



C.W.A. Minderhoud

Safety Evaluation of Kitepower Operations

Safety Evaluation of Kitepower Operations

By

C.W.A. Minderhoud

in partial fulfilment of the requirements for the degree of

Master of Science
in Aerospace Engineering

at the Delft University of Technology,
to be defended publicly on Wednesday December 15, 2021 at 14:00 PM.

Supervisors:	Prof. dr. ir. H.A.P. Blom	TU Delft
	Ir. J. Breuer	Kitepower
Thesis committee:	Dr. -Ing, R. Schmehl	TU Delft, chair
	Prof. dr. ir. H.A.P. Blom	TU Delft
	Ir. J. Breuer	Kitepower
	Dr. L. Li	TU Delft
	MSc V. Salma	TU Delft

This thesis is confidential and cannot be made public until December 15, 2023.

An electronic version of this thesis is available at <http://repository.tudelft.nl/>.

Preface

This thesis concludes my master degree at the Delft University of Technology and therefore also my time in Delft. I could not have done this without support of many persons, to whom I would like to address a few words to express my gratitude.

Firstly, I would like to thank professor Henk Blom, who supervised me during the thesis. His involvement and dedication has helped me a lot. Furthermore, his feedback and often nightly emails has taken my thesis to a higher level.

Secondly, I would like to thank the people from Kitepower. Various people have helped me during the thesis. However, in special I would like to thank Joep Breuer, my official supervisor. His practical view on the topic has ensured that my thesis adds value to Kitepower.

Lastly, a special thanks to my family and friends for supporting me throughout my complete Master. Especially during the thesis they have motivated and entertained me in my spare time. This has helped me a lot to successfully finish my master degree.

*C.W.A. Minderhoud
The Hague, November 2021*

Contents

Abstract	8
Acronyms	9
1 Introduction	10
1.1 Research Motivation.....	10
1.2 Research Question	11
1.3 Report Outline.....	11
2 Operations Description	12
2.1 System Components	12
2.2 Human Intervention.....	15
2.3 System Phases	16
2.4 System Modes.....	17
3 Third-party Risk Modelling	18
3.1 Safety Risk Indicators for Hazardous Installations.....	18
3.2 Safety Risk Indicators for Unmanned Aircraft Systems.....	21
4 Regulations	25
4.1 Unmanned Aircraft Systems	25
4.2 Air Traffic Obstacle	28
4.3 Hazardous Installations	28
5 Agent-based Approach	36
5.1 Environment	37
5.2 Kite.....	37
5.3 Tether	38
5.4 KCU	39
5.5 5 GHz WIFI Link.....	40
5.6 Weather Sensor	40
5.7 Ground Station.....	41
5.8 Field Team	43
5.9 Caravan Team.....	44
6 Scenario Identification	49
6.1 Hazard Merge.....	49
6.2 Potential Hazard Pre-processing.....	50
6.3 Scenario Identification	51
6.4 Crystallization	52
6.5 Consequences	54

6.6 Comparison FMEA and FTA	55
7 Model Description	56
7.1 Evaluation Steps	56
7.2 Flight Path Model	62
7.3 Event Rate Specification	69
7.4 Non-nominal Descend Model	69
7.5 Unprotected Fatality Model.....	75
8 Model Implementation, Verification, and Validation	76
8.1 Model Implementation	76
8.2 Flight Path Model Verification.....	77
8.3 Non-nominal Descend Model Verification	81
8.4 Non-nominal Descend Model Validation	84
8.5 Wind Turbulence Model Verification	86
9 Simulation Results and Sensitivity Analysis.....	89
9.1 Parameter Values and Sensitivity Judgement.....	89
9.2 Simulation Results Individual Risk.....	96
9.3 Simulation Results Collective Ground Risk per Flight Hour	98
9.4 Simulation Results Collective Ground Risk per Year.....	102
9.5 Sensitivity Analysis.....	103
9.6 Uncertainty Evaluation	113
9.7 Discussion of Results.....	114
10 Conclusion and Follow-up Research.....	115
10.1 Conclusion.....	115
10.2 Follow-up Research.....	116
References.....	118

Abstract

Like any other flying system, Kitepower poses risks to third-parties on the ground. Therefore, in this thesis a safety risk assessment is performed for the system of Kitepower. The research question of this thesis is: Which third-party risks are posed by Kitepower operations and how high are these? Kitepower uses a kite attached to a fixed ground station via a tether to harvest energy. This tether is reeled out by performing crosswind manoeuvres with the kite. The tether is retracted in a situation where the kite is in a gliding configuration with different aerodynamic settings. Therefore, there is a net energy gain between these two modes.

Firstly, a pure hazard brainstorm is performed to identify the hazards of the Kitepower operations. With these hazards four safety-relevant scenarios are constructed. The identified safety-relevant scenarios are: the kite, KCU, and tether fly away; the kite and KCU fly away; the kite flies away; and the complete system slides over the ground. Only the first scenario is modelled in this thesis because the first scenario is the most likely scenario.

The first scenario is modelled by using a model framework that is developed to estimate the third-party risk posed by a drone-based parcel delivery service. This model is adapted to the situation in which the kite, KCU, and tether fly away. A flight path model is used from a preceding MSc thesis. The non-nominal descend model is developed by simulating the forces on the kite. These models have been integrated in a Monte Carlo simulation that simulates the tether failure and subsequent landing of the kite multiple times at the proposed test location in Rutten, the Netherlands.

In the results it is found that the individual risk is the most critical in terms of regulation limits. The operational zone should be enlarged to a radius of 500m in the dominant wind direction at location Rutten to comply with the individual risk limits. The system operations comply with the regulations in terms of collective ground risk. However, it is also observed that the population density and wind conditions have a large impact on the individual risk and collective ground risk. Therefore, these parameters should be adapted if the risk is assessed for new locations. Furthermore, the tether failure rate should be based on operational data and not on the Kitepower expert his assumptions. Lastly, the scenarios that are not analysed yet should be analysed in further research.

Acronyms

ADNOC	Abu Dhabi National Oil Company
ALARP	As Low As Reasonably Practicable
AoA	Angle of Attack
AWE	Airborne Wind Energy
BSO	Basic Safety Objective
BSL	Basic Safety Limit
CBS	Statistics Netherlands
EASA	European Union Aviation Safety Agency
FAA	Federal Aviation Administration
FDIR	Fault Detection, Isolation, and Recovery
FMEA	Failure Mode and Effect Analysis
FTA	Fault Tree Analysis
HSA	Health and Safety Authority of Ireland
HSE	Health and Safety Executive of the United Kingdom
ICAO	International Civil Aviation Organization
KCU	Kite Control Unit
KNMI	Royal Netherlands Meteorological Institute
NAA	National Aviation Authority
RPA	Remotely Piloted Aircraft
SORA	Specific Operations Risk Assessment
TPR	Third-party Risk
UA	Unmanned Aircraft
UAS	Unmanned Aircraft Systems

1 Introduction

In this chapter the topic of this thesis is introduced. Firstly, the research motivation and context around the safety evaluation of the system is discussed. Next, the research question is introduced. Lastly, there is elaborated on the report structure.

1.1 Research Motivation

Global warming is a significant challenge that the world is currently facing. Therefore, a shift in energy generation from fossil energy to renewable energy is needed. Wind energy has developed from an experimental source of energy to one of the most important renewable energy sources in the past decades. At the moment, wind energy delivers more than 590 GW of energy, which is 5% of the global energy consumption [Wiser and Bolinger, 2018]. The main disadvantage of wind energy was its cost per kilowatt hour, but even the cost has dropped to a competing level: below 4 cents per kWh at different locations [Wiser and Bolinger, 2018]. Therefore, wind energy is able to compete with fossil energies. However, the world still needs to make a significant shift from fossil to renewable energy, creating a need to harvest more wind energy. Harvesting more wind energy can be achieved in several ways, such as more efficient wind turbines, larger wind turbines, and more wind turbines. This causes some problems. Firstly, ground-level winds are not present everywhere on earth. Therefore, only a small part of the world is able to generate energy at such a low level of cost. Furthermore, 71% of the earth is covered by water [Gleick, 1993]. Thus, deep-water offshore location are needed to generate energy. These floating platforms and systems are expensive and therefore economically less relevant. A lot of research is performed on this topic, economic development of floating offshore wind energy. A solution is airborne wind energy (AWE). In AWE, the tower is replaced by a tether, allowing AWE to harvest wind energy at higher altitudes. These heights cannot be reached with conventional wind turbines since their economically feasible maximum hub size is around 200m [de Castro et al, 2011], because structural costs increase enormously at these lengths. Since AWE does not have these cost, it can reach the high altitudes with steadier and stronger winds. AWE is also cheaper to manufacture than conventional wind turbines because of the lower total mass of materials.

One of the AWE system solutions is developed by the Dutch company Kitepower. Kitepower uses a kite attached to a fixed ground station via a tether to harvest energy. This tether is reeled out by performing crosswind manoeuvres with the kite. The tether is retracted in a situation where the kite is in a gliding configuration with different aerodynamic settings. Therefore, there is a net energy gain between these two modes. AWE and Kitepower operations are more complex than conventional wind turbines. Furthermore, there are currently no regulations for AWE since it is a new industry. At the moment Kitepower is only allowed to operate at two spots in the Netherlands. Therefore, regulations become more and more important because the system comes closer to the commercial utilisation and to be able to operate at new locations. The safety risks to third-parties on the ground posed by Kitepower are a concern for the operator and the third-parties on the ground. Furthermore, it is difficult to regulate Kitepower, but also AWE in general, in an existing legal European framework. Therefore, there is a need to conduct a systematic safety evaluation.

Thus far, only reliability assessments are performed on the system of Kitepower by Salma et al. (2019). Even for other AWE systems than Kitepower there is no quantitative safety risk assessment available publicly. Therefore, a quantitative third-party safety risk assessment of the

Kitepower operations is needed. The outcome of this quantitative safety risk assessment of Kitepower operations will give new insights for the design team of Kitepower and will be a sole basis for the discussion with regulators.

1.2 Research Question

The aim of this research is to quantify the third-party risk posed by the operations of Kitepower. This is done by adapting the existing third-party risk model framework from Blom et al. (2020). In this thesis the operations of Kitepower is modelled as an agent-based system. Next, the hazards are identified by a performed pure hazard brainstorm. Subsequently, an identified safety-relevant scenario is modelled by the adapted third-party risk model. Lastly, the results are compared with the current third-party risk regulations. The critical components or processes are identified and communicated with the design team of Kitepower. Therefore, the research question for this thesis is defined as follows:

Which third-party risks are posed by Kitepower operations and how high are these?

1.3 Report Outline

This master thesis consists of ten chapters. Firstly, in chapter 2 the operations of the system are explained. Secondly, in chapter 3 third-party risk modelling is introduced. Thirdly, in chapter 4 an overview of the regulations on AWE and third-party risk is given. In chapter 5 the operations of the system are modelled as an agent-based system, as a first step in the safety risk assessment. Next, in chapter 6 the safety-relevant scenarios are identified by using the performed pure hazard brainstorm. Subsequently, the developed third-party risk model is described in chapter 7. In chapter 8 the model implementation, validation, and verification are discussed. Furthermore, in chapter 9 the results are depicted and the sensitivity analysis is performed. Finally, in chapter 10 the thesis is concluded and recommendations are given for further research.

2 Operations Description

To understand this thesis two important research fields are needed, the operations of Kitepower, and third-party risk modelling. Firstly, in this chapter the operations of Kitepower are introduced. The operations of Kitepower are currently in the testing phase. This means that the design of the system will still change in the future. The current system design is analysed in this thesis, therefore the current system is described in this chapter. In section 2.1 the major system components are introduced. Secondly, in section 2.2 the influence of humans on the operations is explained. Next, the major operational phases of Kitepower are discussed in section 2.3. Lastly, in section 2.4 the different operational modes are discussed.

2.1 System Components

In this section the major system components are introduced. In Figure 2.1, the overview of the system is depicted. The system consists of four major components: kite, kite control unit (KCU), tether, and ground station.

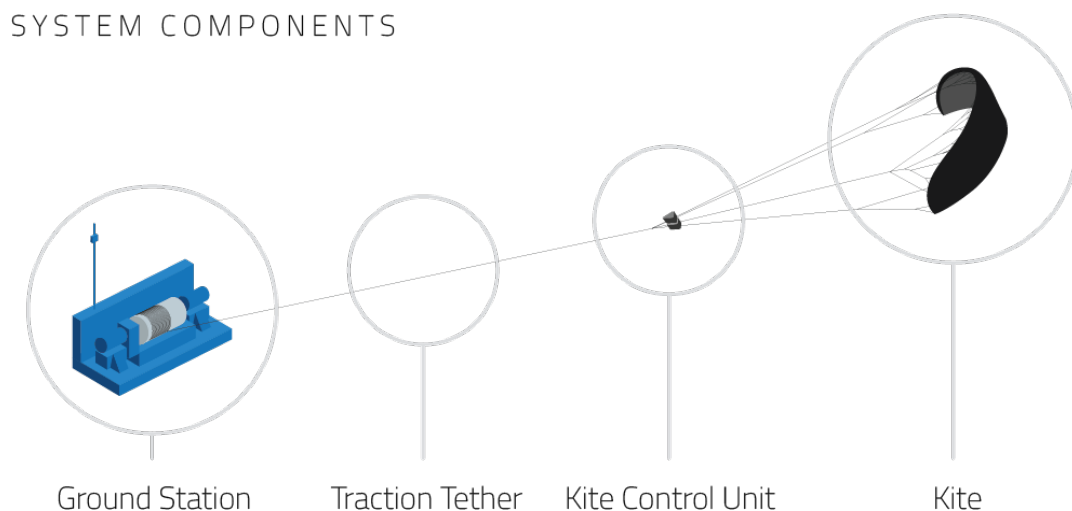


Figure 2.1: Components overview of the system [Kitepower, 2021].

Kite

The wing of the system is a kite which looks similar like a kite from kite surfing. The kite is a sail with inflatable beams in two directions, span and chord direction. The kite, that is analysed, has a surface area of 60 m². The kite is attached to the tether and KCU, both introduced in the next paragraphs, with the bridle system as depicted in Figure 2.2. The bridle system consists of three major components. Firstly, the leading edge of the kite is attached with bridles to the tether, the front tube suspension. The main function of the front tube suspension is the load transfer from the kite to the tether. Secondly, the wing tips of the kite are attached at the rear to the KCU, the steering lines. The KCU influences these two steering lines. The angle of attack is changed by symmetrically changing the length of the steering lines. The heading of the kite is changed by asymmetrically changing the length of the two steering lines. Lastly, the kite is attached to the tether with a safety line. The attachment point is different than the front tube suspension. There is a weak link and a redundant safety release mechanism in between. The weak link breaks if the load on the tether is too close to the tether limit. The redundant safety release mechanism

separates the tether from the KCU if an unsafe situation is detected by the KCU, the ground station, or the operator. The safety line is still attached to the tether in these situations. While the front tube suspension is not attached in these situations. The safety line is only under tension in these emergency situations.

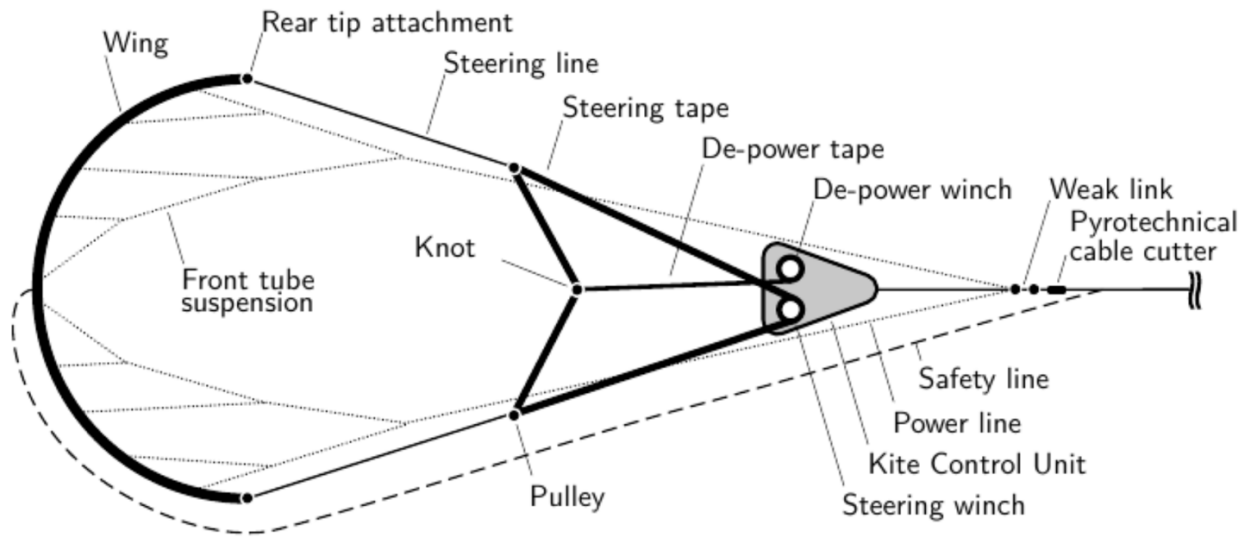


Figure 2.2: Schematic layout of the kite, bridle system, and KCU [van der Vlugt et al., 2013].

In the kite there are also GPS and two Inertial Measurement Units (IMU's) present to measure the state. The GPS has a redundancy of two. The IMU's have both a redundancy of three. The GPS and IMU's together determine the location, velocity, and (rotational) accelerations of the kite. The GPS and IMU's are attached with a four core cable to the KCU.

Kite Control Unit

The KCU is a cable robot that is suspended below the wing and steers the kite. The KCU is located between the kite and the tether, as depicted in Figure 2.1 and Figure 2.2. The KCU is attached by the bridle system and the tether. The KCU has the following components:

- **Depower tape:** The depower tape is attached to both steering lines, of the bridle system, and the depower winch.
- **Depower winch:** The depower winch influences the angle of attack of the kite by changing the length of the depower tape. This influences the depower state of the kite, the power the kite generates.
- **Depower brake:** The depower brake is used to arrest the depower winch.
- **Steering tapes:** The steering tapes are attached to both steering lines, of the bridle system, and the steering winch.
- **Steering winch:** The steering winch influences the heading of the kite by changing the length of the steering tapes asymmetrically.
- **Gearboxes:** Gearboxes are present for the depower winch and steering winch.
- **Ram air turbine:** The ram air turbine is present on the KCU. This module generates energy for the battery, winches, and computer of the KCU.
- **Battery:** The rechargeable battery supplies electrical energy to the computer, depower winch, steering winch, and sensors (GPS and IMU's) in the kite.
- **Computer:** The computer is the brain of the robot. The software of the computer consists of the following components:

- **Message forwarder KCU:** The message forwarder routes all messages between the KCU and ground station. The communication, between the KCU and the ground station, is performed by a 5 GHz WIFI link.
- **Kite control daemon:** The kite control daemon reads the kite sensors and the state of the kite. Furthermore, it receives the desired state of the depower winch and the steering winch from the flight path controller. Based on this information, commands are sent to the depower winch and the steering winch.
- **Kite state estimator:** The kite state estimator reads the kite state, KCU state, and ground state, received by the message forwarder. Next, it estimates the future state of the kite. The estimated future state is sent to the flight path controller.
- **Flight path controller:** The flight path controller sends messages to the kite control daemon to steer the kite. Moreover, the kite receives the estimated future state of the kite, the current state of the kite and the KCU, and the desired trajectory from the message forwarder if the path is adapted during the operation.
- **Health supervisor KCU:** The health supervisor KCU normally only monitors the health of the connection to the ground station. However, if this connection is lost it monitors the health of the KCU and the kite. Furthermore, in the scenario of connection loss, the health supervisor turns on the system state controller.
- **System state controller KCU:** The system state controller is turned on by the health supervisor if needed. The system state controller checks the state of all components of the system and sends this information to the health supervisor.

Tether

The tether connects the ground station and the kite. The tether is depicted in Figure 2.1 and is a 14mm dyneema rope with a total length of 360m. The main function of the tether is the load transfer from the KCU to the ground station, no electricity is transferred via the tether. Due to the length of the tether, only one tether is present. The tether is designed in a “safe-life” philosophy. This means that the tether is designed to not fail within a certain amount of time or number of cycles. The tether is replaced after a certain amount of time or number of cycles.

Ground Station

The ground station is located at the ground. The ground station is attached with the tether to the rest of the system. The ground station has two main functions. Firstly, it converts the tether force into electrical energy. The second main function is the tether retraction. The ground station has the following components:

- **Winch:** The winch is the component that reels-in or out the tether.
- **Generator:** The generator generates electrical energy with the torque of the winch during the reel-out of the tether and generates the torque for the winch during the reel-in of the tether.
- **Gearbox:** The gearbox is the mechanism between the generator and the winch.
- **GPS:** The GPS measures the location of the ground station.
- **Weather sensor:** The weather sensor measures the weather at the ground station. It measures the wind velocity and wind direction. The weather sensor is located close to the ground station. A cable connects the weather sensor with the computer.
- **Computer:** The computer is the brain of the ground station. The software of the computer consists of the following components:
 - **Message forwarder ground station:** The message forwarder routes all messages between the ground station and KCU. The communication, between the KCU and the ground station, is performed by a 5 GHz WIFI link.

- **Winch control daemon:** The winch control daemon is the control centre of the winch. It receives the winch control commands from the KCU and sends back the winch state to the KCU. Furthermore, it sends the winch state to the ground state estimator. The winch control daemon is programmed in a way that the tether is always reeled in if there is no or too little tether force.
- **Sensor daemon:** The sensor daemon reads the GPS sensor and weather sensor. The output is the ground state. The ground state is sent to the ground state estimator and to the KCU, via the message forwarder.
- **Ground state estimator:** The ground state estimator estimates the future ground state with the winch state and ground state.
- **Health supervisor ground station:** The health supervisor monitors the complete system, including kite and KCU. Furthermore, the health supervisor sends orders to the system its components if actions are needed.
- **System state controller ground station:** The system state controller checks the state of all components of the system and sends this information to the health supervisor.
- **Proto logger daemon:** The proto logger daemon receives all messages sent around and logs them.

2.2 Human Intervention

The human intervention in the operation of Kitepower is explained in this section. Two human teams are present in the operations of Kitepower, the caravan team and the field team. The caravan team monitors the operation from a display and intervenes if needed. The caravan team could be located remotely. The field team prepares the system before launch and monitors the system visually in the field. Both teams are discussed in more detail in this section.

Caravan Team

The caravan team has a display in front of them. This display is connected to the system. This display depicts the following:

- **System state:** The state of the ground station, KCU, and kite are depicted.
- **Top view:** The display depicts the position of the kite from above, centred around the ground station.
- **Front view:** The display depicts the position of the kite in the hemisphere around the ground station.
- **Control state:** The display depicts the information about the current control state of the kite (steering and depower position) and which device controls the kite.

Next to the observing task, the caravan team can also intervene. This is done by starting another mode. These modes are discussed in section 2.4. However, in principle the caravan team does not intervene, only when anomalies occur. The caravan team usually consists of only one person.

Field Team

The field team always stands in the field. Before launch the field team prepares the ground station, kite, and KCU. During and after launch the field team monitors the system and the environment, only one person is needed for these tasks. If needed, the field team intervene physically to the ground station. If actions are needed, for example, the mode needs to be changed, the field team communicates the observations to the caravan team. During landing, the field team secures the kite and packs the complete system.

2.3 System Phases

In this section the operations phases of the system are described. The kite has the following operations phases: launch, normal operation or pumping cycle, and landing. The phases are as follows:

- **Launch:** The first phase is the launch of the kite. The kite, KCU, and ground station are prepared by the field team. The caravan team monitors the system and orders the system to launch the kite. The kite is anchored with magnets to the ground and raised. The bridle system and tether are tensioned. The kite releases and takes-off at the point that the bridle system and the tether are under tension. If not enough wind is present the tether is reeled in to make sure the kite takes off.
- **Pumping cycle:** The second phase is the pumping cycle or normal operation. After the launch phase the kite starts the normal operation, if no anomalies are detected. This normal operation is a so called “pumping cycle”. An overview of the pumping cycle is depicted in Figure 2.3. The pumping cycle has four sub-phases. The sub-phases are:
 - **Reel-out:** In the reel-out phase, the most energy is gained by reeling out the tether. In the reel-out phase, the kite flies a figure of eight, crosswind manoeuvring, to optimally gain energy.
 - **First transition:** In the first transition phase, the kite depowers, decreases the angle of attack, and moves to the highest point of the operation, the point to zenith, before it is retracted by the tether.
 - **Reel-in:** In the reel-in phase, the tether of the kite is retracted. The kite has a smaller angle of attack in this phase. This results in less drag than during the reel-out phase. This drag difference causes a net generation of energy.
 - **Second transition:** In the second transition phase, the kite powers, increases the angle of attack, and moves to the starting point of the reel-out phase. After this transition, the reel-out phase starts again.

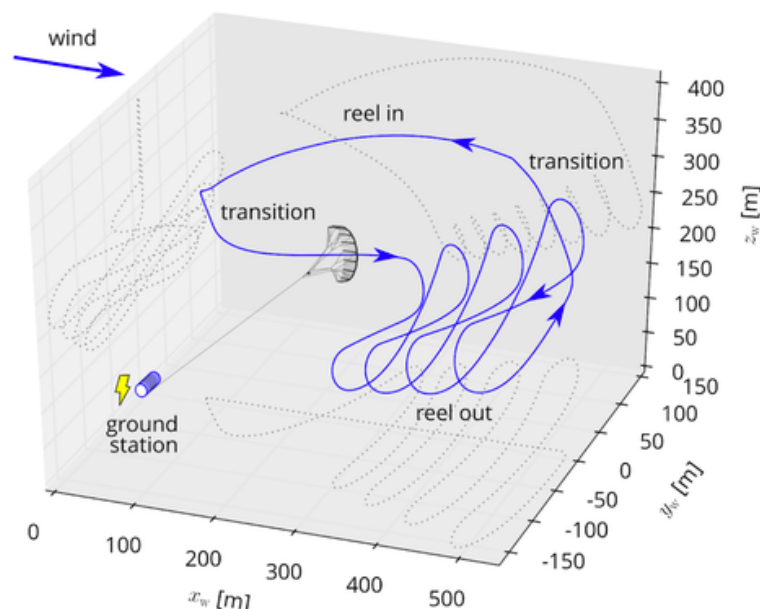


Figure 2.3: Overview of the pumping cycle [Schmehl, 2019, Fechner, 2016].

- **Landing:** The landing phase consists of three parts. Firstly, the kite is reeled in to a low altitude to park the kite. During this manoeuvre the aerodynamic settings are constantly adjusted to the wind speed to prevent overflying of the zenith, and to keep the tether force within the limits. The second part starts when the tether has reached a certain length and all

the landing requirements are met. At this point a landing path is followed. This path is depicted in Figure 2.4. In the second part three waypoints are followed by adapting the aerodynamic settings. The last part of the landing phase starts if the kite is at a certain height. At this point the kite starts landing. In the final manoeuvre, the kite is powered and moved to the edge of the wind window. Therefore, the kite starts flaring and in the end drops to the ground.

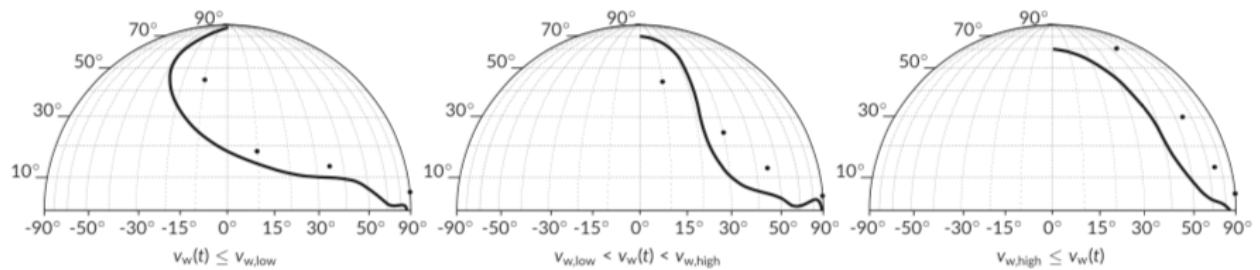


Figure 2.4: Landing paths with different wind speed [Salma et al., 2019].

2.4 System Modes

In this section the operation modes of the system are described. These modes are activated by the caravan team or automatically initiated by one of the health supervisors. The system has the following modes:

- **Normal operation mode:** The normal operation mode is started at the start of every operation. The normal operation mode is normally started with the launch phase described in section 2.4. After the launch, the pumping cycle is followed as described in section 2.4. If the kite starts in the parking mode, it immediately starts the pumping cycle. The normal operation mode is ended by one of the other modes.
- **Parking mode:** In the parking mode, the kite moves to point towards zenith and terminates the normal operation mode. This manoeuvre is fairly similar as the first transition phase. The parking is initiated due to weather conditions, an anomaly, or to prevent a landing and relaunch.
- **Landing mode:** The landing mode is set when the kite needs repair/maintenance or the fault detection, isolation and recovery (FDIR) system detects a problem with the operational safety. In this mode the landing manoeuvre is executed as described in section 2.3. The landing phase described in section 2.3 is started in this mode.
- **Emergency landing mode:** The emergency landing mode is initiated when the redundant safety release mechanism is initiated or the weak link is broken. In this situation the KCU is separated from the tether. The KCU hangs under the kite with the safety line under tension. The kite is retracted to the ground in a gliding configuration with the KCU stabilising the kite. The emergency landing follows a landing path with only one navigation point. The tether reels in constantly until it has reached a certain touchdown point. At this point the kite depowers and falls to the ground.

All these modes are executed in the operational zone of the system. The operational zone is a circle centred around the ground station with a radius of 400m. Only the operator is allowed in the operational zone, no third-parties are allowed.

3 Third-party Risk Modelling

Two important research fields are needed to understand this thesis, the operations of Kitepower, and third-party risk modelling. In chapter 2 the operations of Kitepower are introduced. In this chapter third-party risk modelling is introduced. The safety risk indicators are introduced and the modelling of the safety risk indicators are described. The safety risk indicators are used to identify the acceptability of the risk. Therefore, the safety risk indicators are compared with the regulations. The regulations around the safety risk indicators are discussed in chapter 4. Firstly, in section 3.1 the most important safety risk indicators for hazardous installations and commercial air transport of third-party risks are introduced and formally defined. Furthermore, the mathematical definition of these most important risk indicators are explained. Secondly, in section 3.2 there is focused on the risk indicators of unmanned aircraft systems (UAS) operations. The risk indicators are formally defined for the UAS operations. Moreover, the mathematical definition of the risk indicators for UAS operations are discussed. The focus on UAS operations is chosen because of the similarities with the operations of Kitepower. Lastly, in section 3.2 there is focused on the type of accidents for UAS operations. Several types of UAS crashes are a risk for third-parties.

3.1 Safety Risk Indicators for Hazardous Installations

The safety risk indicators for hazardous installations and commercial air transport of third-party risk are introduced in this section. In literature there are three main safety risk indicators identified. Firstly, the individual risk indicator is discussed in this section. Secondly, the societal risk indicators are discussed in this section. The most important societal risk indicators are collective risk and FN-curve.

Individual Risk

Individual risk is the risk indicator that is mostly used by authorities, such as the Dutch ministry of housing, spatial planning, and environment. Individual risk is a common safety risk indicator in the commercial air transport. The definition of individual risk in commercial air transport is defined as follows [Blom et al., 2020]:

“Individual risk, $R_I(y)$, is the probability that an average unprotected person, who resides permanently at ground location y , would get killed or fatally injured due to the direct consequences of an aircraft accident during a given annum.”

The assumption is made here that the individual is permanently unprotected and permanently present at a certain location. Therefore, the individual risk is location dependent.

Individual risk is often used to determine the risk of hazardous objects. Hazardous objects can be all kinds of objects, such as an airport, transport routes, or Kitepower operations. A common way to depict individual risk is a contour map. In Figure 3.1 two example contour maps are depicted, the left map is a contour map of a point source, such as a factory. The right map is a contour map of a line source, such as an runway or road. It is observed that the individual risk is independent of the population density. Authorities have set a standard for individual risk for populated areas [Bottelberghs, 2000]. The value used in the Netherlands is depicted in Equation 3.1. Equation 3.1 is valid if y is outside the operational area of the hazardous object.

$$R_I(y) < 10^{-6} \text{ (per year)} \quad (3.1)$$

This standard is set for involuntary risk, third-party risk is involuntary risk. The regulations on hazardous installations in the Netherlands and other countries are discussed in more detail in chapter 4.

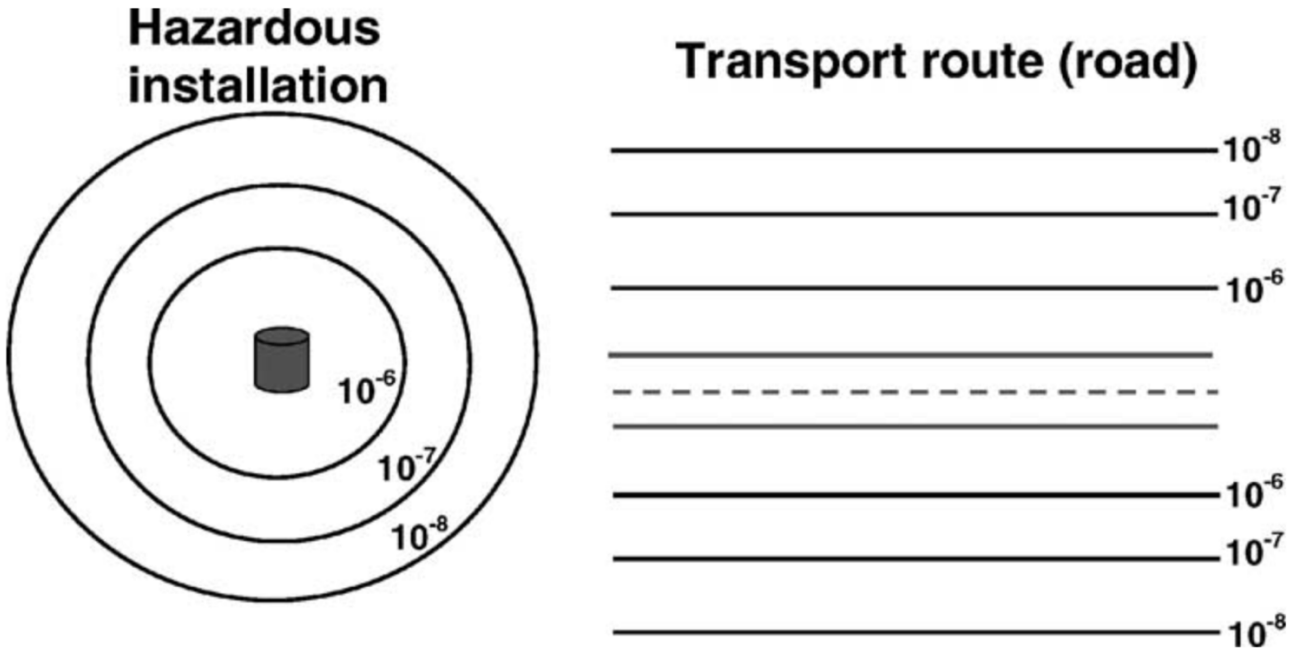


Figure 3.1: Individual risk contour maps for a point source and a line source [Jonkman et al., 2003].

The individual risk is independent of the population density, as mentioned before. Therefore, individual risk is mathematically defined for commercial air transport in Equation 3.2 [Ale and Piers, 2000, Blom et al., 2020].

$$R_I(y) = \sum_d N_d P(C|d) p_s(y|d) |A(d)| P(Fly \in A(d)) \quad (3.2)$$

In Equation 3.2, N_d is the yearly number of flights of flight type d flying in area Y . $|A(d)|$ represents the crash area size of flight type d . $P(C|d)$ represents the accident probability model of flight type d [Blom et al., 2006]. This model represents the probability that a flight of type d crashes [Ale and Piers, 2000]. The determination of specific accident rate models for third-party risk are widely available for commercial air transport.

In Equation 3.2, $p_s(y|d)$ represents the accident location probability model [Ale and Piers, 2000]. This model describes the probability of ending up at a particular location if a crash occurs. There are three types of accident location probability models, according to Ale and Piers (2000): non-dependent accident location probability models, runway referenced accident location probability models, and traffic-route referenced accident location probability models. All these models depend on historical data.

Lastly, in Equation 3.2, $P(Fly \in A(d))$ represents the conditional probability that an unprotected person dies in crash impact area $A(d)$ by a flight of type d [Blom et al., 2020]. This is an accident consequence model. Fatal accidents on the ground are the only consequences considered in third-party risk modelling around airports [Ale and Piers, 2000]. Accident consequence models are divided in three categories:

- **Subjective estimation accident consequence models (Category I):** Models that subjective estimates the fatalities inside an area and estimates the size of this area [Hillestad et al., 1993, Solomon, 1974].
- **Deterministic accident consequence models (Category II):** Analytical models on the lethal consequences which estimate the size of the crash area [Ale and Piers, 2000].
- **Probabilistic accident consequence models (Category III):** This statistical models are mostly based on accident data from accident reports [Evans et al., 1997, Piers, 1998].

Societal Risk Indicators

Societal risk indicators are another important way to identify third-party risk. Societal risk represents the number of fatalities within a certain area per time unit. Individual risk does not take the population density into account. Societal risk does take population density into account, as depicted in Figure 3.2. Figure 3.2 represents the difference between societal and individual risk. Both figures have the same individual risk. However, the right figure has a higher societal risk than the left figure due to the population density. As mentioned before, there are two main societal risk indicators, the FN-curve and collective risk. The FN-curve is first discussed. The formal definition of the FN-curve for hazardous installations is defined as follows [Laheij et al., 2000]:

“The FN-curve, $R_{FN}(n)$, is the probability that a group of n or more third party persons will be killed or fatally injured due to the direct consequences of an aircraft accident during a given annum.”

The FN-curve is obtained by deriving the probability density function from the number of fatalities per year. Mathematically the FN-curve is defined in Equation 3.3 [Jonkman et al., 2003].

$$R_{FN}(n) = P(n_F \geq n), \text{ for } n \geq 1 \quad (3.3)$$

Where n_F is the number of persons on the ground in a given area Y that are killed or fatally injured due to the direct consequences of a hazardous installations during a given year. Other literature, for example, Jonkman et al. (2003) define the FN-curve different, these sources refer to “more than n ”. This definition is depicted in Equation 3.4.

$$R_{FN}^>(n) = P(n_F > n) = R_{FN}(n + 1), \text{ for } n \geq 0 \quad (3.4)$$

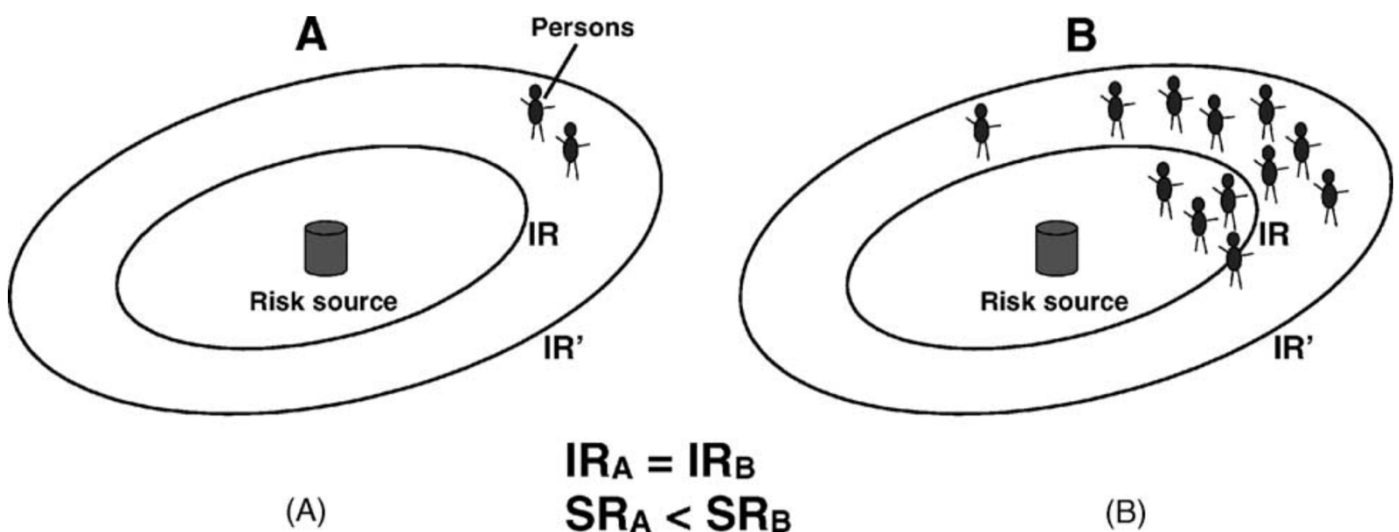


Figure 3.2: This figure represents the difference between societal and individual risk [Jonkman et al., 2003].

Several authorities regulate third-party risk via an FN-curve. This is done by setting a limit to the FN-curve. A limit line is set since an FN-curve is a curve and not one value. The line is defined according to Equation 3.5.

$$R_{FN}(n) < \frac{C}{n^\alpha} \quad (3.5)$$

In Equation 3.5, n represents the number of fatalities, C is the constant that sets the location of the line, and set the steepness of the limit line. If the line is set at risk neutral, α is set at 1. If the line is set at risk averse, α is set at 2. In chapter 4, the different regulations on the FN-curve are discussed.

The second important societal risk indicator is collective risk. The formal definition of collective risk for hazardous installations is explained as follows [Blom et al., 2020]:

“The collective risk, R_C , is the expectation value of the number of fatalities in a given area Y that are killed or fatally injured due to the direct consequences of a hazardous activity during a given annum.”

Therefore, collective risk is mathematically defined in Equation 3.6.

$$R_C = E(n_F) \quad (3.6)$$

Where n_F is the number of yearly fatalities in a given area Y , the same as for the FN-curve. The collective risk is obtained from the FN-curve. The collective risk is calculated by the summation of the FN-curve, as depicted in Equation 3.7 [Laheij et al., 2000].

$$R_C = \sum_{n=1}^{\infty} R_{FN}(n) \quad (3.7)$$

Furthermore, collective risk and individual risk are related to each other if the assumption is made that people are unprotected to a hazard caused by the hazardous installation. In Equation 3.8, the relation between the individual risk and collective risk is depicted. In Equation 3.8, $\rho(x, y)$ is the population density at location x, y .

$$R_C = E(n_F) = \iint_A R_I(x, y) \rho(x, y) dx dy \quad (3.8)$$

3.2 Safety Risk Indicators for Unmanned Aircraft Systems

In this section, the general safety risk indicators discussed in section 3.1 are discussed for the UAS operation. The most important risk indicators are the same as for hazardous installations, namely individual risk, FN-curve, and collective ground risk. The mathematical definitions of individual and collective ground risk for UAS operations are per flight and not per year. Blom et al. (2020) have adapted these indicators. In this section individual risk and both societal risk indicators for the UAS operations are explained in more detail. The adaptations on the risk indicators performed by Blom et al. (2020) are discussed and other types of collective risks than ground risks are introduced.

Individual Risk

The individual risk indicator for UAS operations is adapted from the commercial air transport model described in section 3.1. The formal definition of individual risk for UAS operations is defined as [Blom et al., 2020]:

“Individual risk per UAS operation, $R_I^i(y)$, is the probability that an unprotected average person at a location y is killed or fatally injured due to a ground crash by UAS flight i .”

Now the formal definition of individual risk is known, the mathematical definition of individual risk is depicted in Equation 3.10 [Bertrand et al., 2017, Cour-Harbo, 2019, Primatesta et al., 2019].

$$R_I^i(y) = \sum_{e \in E} P(eli) p_s(y|li, e) |A(d_i, e)| P(Fly \in A(d_i, e)) \quad (3.9)$$

Where $p(eli)$ represents the probability of a crash type e by flight i . $p_s(y|li, e)$ is the accident location probability model for flight i due to crash type e . $A(d_i, e)$ is the impact area of crash type e of vehicle d_i . Lastly, $P(Fly \in A(d_i, e))$ is the probability that an unprotected average person is killed by a crash in area $A(d_i, e)$. $P(Fly \in A(d_i, e))$ depends on the kinetic energy ($\frac{1}{2}mv^2$). Therefore, $P(Fly \in A(d_i, e))$ mainly depends on the impact velocity [Bertrand et al., 2017, Cour-Harbo, 2019, Primatesta et al., 2019]. There are two main differences between Equation 3.9 and Equation 3.2. Firstly, Equation 3.9 gives the individual risk per flight, while Equation 3.2 gives the annual individual risk. Secondly, Equation 3.2 only looks at different types of flights, while Equation 3.9 looks into different types of flights and also into different crash events.

Thus far, individual risk per flight was the most commonly used individual risk indicator for UAS operations. However, most regulations are on individual risk per year, as described in section 3.1. Therefore, Blom et al. (2020) have developed the individual risk indicator $R_I^{UAS}(y)$. The formal definition of $R_I^{UAS}(y)$ is as follows [Blom et al., 2020]:

“The individual risk per year for UAS operations, $R_I^{UAS}(y)$, is the probability that an average unprotected person, who resides permanently at ground location y , would get killed or fatally injured due to the direct consequences of a ground crash by a UA flight during a given annum.”

In Equation 3.10, the relationship between $R_I^i(y)$ and $R_I^{UAS}(y)$ is depicted. In Equation 3.10 N is the number of UA flights per year.

$$R_I^{UAS}(y) = 1 - \prod_{i=1}^N (1 - R_I^i(y)) \quad (3.10)$$

Societal Risk Indicators

The two main societal risk indicators of UAS operations are the FN-curve and collective ground risk, as mentioned before. Firstly, the FN-curve is introduced for the UAS operation. The formal definition of an FN-curve for UAS operation is defined as follows [Blom et al., 2020]:

“The FN-curve for UAS operation, $R_{FN}^{UAS}(n)$, is the probability that in an area Y a group of n or more third-party persons will be killed or fatally injured due to the direct consequences of ground crashes by UA flights during a given annum.”

Therefore, the FN-curve is mathematically defined by Equation 3.11.

$$R_{FN}^{UAS}(n) = P(n_{F,i}^{UAS} \geq n) , \text{ for } n \geq 1 \quad (3.11)$$

Where $n_{F,i}^{UAS}$ is the number of people on the ground that are killed by a ground crash of UA flight i . $n_{F,i}^{UAS}$ is mostly smaller or equal to one because UA are often small vehicles [Blom et al., 2020]. Therefore, the FN-curve is a steep curve for UAS operations, the FN-curve decreases quickly with an increasing number of fatalities.

As mentioned before, the second important societal risk indicator for UAS operation is collective ground risk. Collective ground risk per UA flight, $R_{Cground}^i$, is formally defined as follows [Blom et al., 2020]:

“The collective ground risk per UA flight, $R_{Cground}^i$, is the expected number of persons on the ground in a given area Y that are killed or fatality injured due to the i -th UA flight colliding to the ground.”

Collective ground risk per UA flight, $R_{Cground}^i$, is mathematically defined by Equation 3.12 [Ancel et al., 2017, Bertrand et al., 2017].

$$R_{Cground}^i = E(n_{F,i}^{UAS}) = \iint_A R_f^i(x,y) [1 - P(S|x,y,i)] \rho(x,y) dx dy \quad (3.12)$$

Where $R_f^i(x,y)$ is the individual risk for an average unprotected person at location x,y by flight i . $P(S|x,y,i)$ is the probability that a person is protected against a crash of flight i at location x,y . Lastly, $\rho(x,y)$ represents the population density at location x,y .

Blom et al. (2020) have adapted the collective ground risk per UA flight, $R_{Cground}^i$ to the collective ground risk per year, $R_{Cground}^{UAS}$. The formal definition of the collective ground risk per year, $R_{Cground}^{UAS}$, is as follows [Blom et al., 2020]:

“The collective ground risk per year, $R_{Cground}^{UAS}$, is the expected number of persons on the ground in a given area Y that are killed or fatally injured due to the direct consequences of ground crashes by flights of the UAS operation during a given annum.”

The collective ground risk per year, $R_{Cground}^{UAS}$, is calculated by the summation of the collective ground risk per flight as depicted in Equation 3.13.

$$R_{Cground}^{UAS} = \sum_{i=1}^N R_{Cground}^i \quad (3.13)$$

The collective ground risk per year, $R_{Cground}^{UAS}$, can also be calculated from the FN-curve, as depicted in Equation 3.14 [Blom et al., 2020].

$$R_{Cground}^{UAS} = \sum_{n=1}^{\infty} R_{FN}^{UAS} \quad (3.14)$$

The curve that sets the regulations for the FN-curve, depicted in Equation 3.5, is adapted to set regulations on collective ground risk. This adaptation is based on the assumption that a crash of a UA flight leads to maximum one fatality. This is observed by the slope of the FN-curve of UAS operations. This adaptation is depicted in Equation 3.15 [Blom et al., 2020].

$$R_{Cground}^{UAS} < C \sum_{n=1}^{\infty} \frac{1}{n^{\alpha}} \quad (3.15)$$

In Equation 3.15, α should always be larger than 1 because otherwise Equation 3.15 is unbounded [Blom et al., 2020]. In section 4.3 an overview of these parameters are given of different countries.

Thus far, the only collective risk considered is the ground risk, third-party risk in the air is not considered. Jiang et al. (2020) have identified five types of UAS accidents that have the potential of third-party fatalities, these types are as follows:

- **Type 1:** The UA flight collides to a commercial air transport flight.
- **Type 2:** The UA flight collides to a general aviation flight.
- **Type 3:** The UA flight collides to an urban air mobility UA carrying on-board passengers.
- **Type 4:** The UA flight collides to the ground as a consequence of a mid-air collision of types 1 until 3 or with another UA flight.
- **Type 5:** The UA flight collides to the ground without preceding mid-air collision.

Therefore, the collective risk per flight, R_C^i , is calculated by summing the expectation value of the number of fatalities per flight for every type of accident, this is depicted in Equation 3.16 [Jiang et al., 2020].

$$R_C^i = E(n_F^i) = E(n_{FCAT}^i) + E(n_{FGA}^i) + E(n_{FUAM}^i) + E(n_{FUSair}^i) + E(n_{FUSground}^i) \quad (3.16)$$

In Equation 3.16 $E(n_{FCAT}^i)$ is the expected number of fatalities due to a collision type 1 of flight i , $E(n_{FGA}^i)$ is the expected number of fatalities due to a collision type 2 of flight i , $E(n_{FUAM}^i)$ is the expected number of fatalities due to a collision type 3 of flight i , $E(n_{FUSair}^i)$ is the expected number of fatalities due to a collision type 4 of flight i , and $E(n_{FUSground}^i)$ is the expected number of fatalities due to a collision type 5 of flight i .

The collective risk per year is obtained by substituting Equation 3.16 in Equation 3.13. This is depicted in Equation 3.17, the collective risk per flight is summed over N , the number of flights per year [Jiang et al., 2020].

$$R_C^{UAS} = E(n_F) = \sum_{i=1}^N E(n_{FCAT}^i) + E(n_{FGA}^i) + E(n_{FUAM}^i) + E(n_{FUSair}^i) + E(n_{FUSground}^i) \quad (3.17)$$

In this thesis the focus is on collective ground risk. On some parameters discussed in this chapter there are limits set by authorities. Therefore, in the next chapter there is a research performed on the regulations on these parameters but also on the regulations on AWE in general. These limits are used in this thesis to identify if the system is safe or not.

4 Regulations

In this chapter the focus is on the regulations of AWE and for Kitepower in particular. In this chapter the safety risk criteria are found that are used for the safety risk assessment. Currently, there are no regulations on AWE. Kitepower operates at two locations at the moment. At Valkenburg, the first test site, the kite operates under art. 2 (a) and (b) of the Regulation Cable Kites and Small Balloons since 2019. At the second test site, Melissant, the kite operates under the same conditions as the first test site since 2020 [Overheid, 2014].

The current operational regulations are complex and not usable for commercial usage. Therefore, Salma et al. (2018) have looked into the regulations of other systems comparable to AWE. Salma et al. (2018) describe that AWE can be regulated in three categories. Namely, in the regulations of unmanned air systems (UAS), air traffic obstacles, and for tethered gas balloons. However, Salma et al. (2018) describe that tethered gas balloons is not a feasible option for Kitepower because Kitepower has a complex control system. Therefore, this option is not discussed in this chapter. The regulations of UAS are discussed in section 4.1. The regulations of air traffic obstacles are discussed in section 4.2. In these sections no quantitative limits on the third-party risk indicators of chapter 3 were found. Therefore, there is looked into the regulations of hazardous installations in section 4.3.

4.1 Unmanned Aircraft Systems

In this section the regulations around UAS are discussed. The regulations of UAS are a hot topic these days for international aviation organizations and national aviation agencies due to the increasing popularity of UAS. However, one of the main challenges is the different types of UAS. For example, some UAS only weight 16 grams [de Croon et al., 2012], while other vehicle weight up to 14 tons [Clegg, 2021]. Currently, there is not one classification method for this high range in UAS. Some UAS are certified by the FAA or EASA with a case by case risk evaluation for specific operations. Kitepower and other AWE systems can be classified in the UAS category. For the operations of AWE applications an airworthiness certificate is needed [Salma et al., 2018]. Two types of airworthiness certifications exist in aviation: the standard airworthiness certificate and the restricted airworthiness certificate. The restricted airworthiness certificate restricts operational limitations, such as manoeuvres, speed, and location [Salma et al., 2018]. It is unclear if AWE systems, such as Kitepower, fall into the UAS regulations. Therefore, there is looked into the definition of UAS used by ICAO, EASA, and FAA in this section. ICAO (International Civil Aviation Organization) is an important organization in terms of regulation. ICAO develops international standards and recommended practices. These are used by member states for their regulations. EASA (European Aviation Safety Agency) advises the European Commission and the countries of the European Union regarding new regulations. FAA (Federal Aviation Authority) is the civil aviation agency of the US and sets the regulation in the US. EASA and the FAA are authorized to certify civil aircraft for international use.

ICAO

ICAO does not use the term UAS but RPA (Remotely Piloted Aircraft). ICAO defines RPA as follows [ICAO, 2005]: “An unmanned aircraft which is piloted from a remote pilot station”. An interesting point is made here by ICAO, ICAO states the following [ICAO, 2005]: “autonomous unmanned aircraft and their operations including unmanned free balloons or other types of aircraft

which cannot be managed on a real-time basis during flight is not in the scope of DOC 10019". This means that there are currently no rules by ICAO for tethered aircraft or AWE systems. In annex 7 of ICAO (2005) it is only observed that kites are categorised as a non-power driven heavier than air aircraft.

EASA

The regulations of the European Union define that the following aircraft do not lie within the EASA regulations [EASA, 2008]: "Unmanned aircraft with an operational mass of no more than 150kg". The national aviation authorities (NAA's) are responsible for the aircraft that are not regulated by EASA. The NAA's should certify Kitepower since the weight of the kite is below 150kg. EASA still advises the NAA's of the EU for regulations around UAS lighter than 150kg. Ampyx Power, one of the AWE concepts, and EASA have concluded that Ampyx is more an unmanned glider than a normal UAS [Salma et al., 2018]. Therefore, it is decided that Ampyx falls in the sailplanes category. EASA also states in NPA-2014-09 that tethered aircraft are remotely piloted aircraft [Salma et al., 2018]. Therefore, according to EASA, AWE falls into the UAS regulations. EASA created a Concept of Operations for Drones [EASA, 2015], regulations for UAS. In this concept three UAS categories are stated: open, specific, and certified. For the open category no certification is required as long as the UAS operate within certain boundaries. UAS in this category present lower risk and should not require the official aeronautical procedures. Kitepower operations are too complex to fall in the open category according to Salma et al. (2018). The UAS that fall in the specific category present a higher risk to its environment. Therefore, a specific risk assessment is needed to identify the requirements to ensure operational safety. The specific risk assessment method is called SORA (Specific Operations Risk Assessment). SORA aims to cover qualitatively third-party fatalities on the ground and third-party fatalities on board of manned aircraft, according to Jiang et al. (2020). In Figure 4.1 an overview is depicted of the third-party fatality terms that are addressed by EASA and FAA. This overview is made by Jiang et al. (2020). The third-party fatality terms are introduced in section 3.2. It is observed that SORA does not include consequences of a preceding mid-air collision between a UAS and a manned aircraft or another UAS. Furthermore, in Figure 4.2 the applicable UAS third-party risk indicators per regulator are depicted. There is no third-party risk indicator contribution from SORA due to its qualitative nature. All in all, Kitepower could fall in the specific category since non-fixed wing concepts fall in this category according to Salma et al. (2018). The last category, certified, is for UAS where very high risks are identified during the performed risk assessment. The UAS in the certified category are subject to rules on certification of the operator, licensing of remote pilots, and the aircraft itself. The airworthiness certification process (AMC RPAS.1309), of the certified category, assess the risk per hazard and the risk per flight hour [Jiang et al., 2020]. AMC RPAS.1309 assess the ground fatalities due to system failure and the mid-air fatalities due to a mid-air collision, excluding mid-air collision between two UAS. This is depicted in Figure 4.1. However, ground fatalities due to mid-air collision are not covered according to Jiang et al. (2020). All in all, the second, fourth, sixth, and eighth term in Figure 4.1 are not covered by the certified category.

Salma et al. (2018) state that at this moment the concepts of AWE systems fall in the specific category. This is also confirmed by EASA, soft wing concepts, such as Kitepower, fall in the specific category of the implementing regulation 2019/947 if the operational mass is below 150kg. Fixed wing and more heavy concepts, such as Ampyx, is categorized in the certified category according to Salma et al. (2018).

Third-party fatality terms of i -th UAS flight	Regulations & Operation category					
	EASA/JARUS SORA	EASA/JARUS AMC RPAS.1309		FAA Advisory Circular 107-2	FAA UAS SRM policy /order 8040.4B	FAA ATO SMS Manual
	Open /Specific /Certified	Certified (for ground risk)	Certified (for air risk)	Work /business	Advanced (in uncontrolled airspace)	Advanced (in controlled airspace)
1. $E\{n_{F_{UASground}}^i\}$	Yes*)	Yes	-	Yes*)	Yes	Yes
2. $E\{n_{F_{UASair}}^i\}$	-	-	-	-	-	Yes
3. $E\{n_{F_{CATonboard}}^i\}$	Yes*)	-	Yes	-	-	Yes
4. $E\{n_{F_{CATground}}^i\}$	-	-	-	-	-	Yes
5. $E\{n_{F_{GANboard}}^i\}$	Yes*)	-	Yes	-	-	Yes
6. $E\{n_{F_{GAground}}^i\}$	-	-	-	-	-	Yes
7. $E\{n_{F_{UAMonboard}}^i\}$	Yes*)	-	Yes	-	-	Yes
8. $E\{n_{F_{UAMground}}^i\}$	-	-	-	-	-	Yes

Figure 4.1: An overview of third-party fatality terms that are addressed by EASA and FAA regulations, created by Jiang et al. (2020).

Regulation/Policy	Operation Category	Applicable TPR Indicator
EASA/JARUS SORA	Open/Specific/Certified	-
EASA/JARUS AMC RPAS.1309	Certified (for ground risk)	$R_{Cground}^i$ *) per hazard and per flight hour
	Certified (for mid-air collision risk)	R_C^i on-board per hazard and per flight hour
FAA Advisory Circular 107-2	Work/business	-
FAA Order 8040.4B	Advanced (in uncontrolled airspace)	$R_{Cground}^i$ *) per hazard and per year UAS operation
FAA ATO SMS Manual	Advanced (in controlled airspace)	R_C^i per hazard and per flight hour

*) excluding ground fatalities due to a preceding mid-air collision

Figure 4.2: An overview of applicable UAS third-party risk indicators, created by Jiang et al. (2020).

FAA

Every civil aircraft must operate with a valid airworthiness certificate, according to the regulations of the FAA (2013). Currently, UAS are certified by the FAA to be able to operate in the airspace of the US. The UAS are certified in the experimental category. However, UAS are certified as conventional aircrafts by subsystem. Thus far, subsystems, such as command and control links, and ground control systems do not have any regulations. Therefore, UAS operations for civil use are restricted in the airspace of the US, according to Salma et al. (2018). The FAA classifies the operation of UAS at very high level. There are three main UAS categories, according to Jiang et al. (2020). The first category is the recreational category, the recreational category focuses on small drones flown for recreational purposes. No safety risk assessment is required in this category. The second category is the work/business category. The work/business category has some constraints, for example, the UAS should be lighter than 25kg and flying below 400 feet. The Advisory Circular 107-2 is the risk assessment method of the work/business category. This risk

assessment method states that a qualitative overall safety risk assessment is encouraged but not obliged. In this safety risk assessment method only the ground collision is considered, as depicted in Figure 4.1. There is no applicable third-party risk indicator, as depicted in Figure 4.2, since there is no quantification. All UAS operations that are not in the recreational category or work/business category are in the advanced category. A safety risk assessment is needed for this category. There are two optional safety risk assessment methods for the advanced category, the Order 8040.4B and the ATO SMS Manual. In Figure 4.1 and Figure 4.2 the difference between the two safety risk assessments is depicted.

However, the FAA has a different approach than EASA regarding AWE systems. As mentioned before, EASA defines tethered aircraft as UAS. However, the FAA excludes the tethered aircraft from the UAS category in the following statement [FAA, 2013]: “A device used or intended to be used for flight in the air that has no on-board pilot. This device excludes missiles, weapons, or exploding weapons, but includes all classes of aircrafts, helicopters, airships, and powered-lift aircraft without an on-board pilot UA do not include traditional balloons, rockets, tethered aircraft and un-powered gliders”. The FAA has made a “Notification for Airborne Wind Energy Systems”, this notification states that each AWE system that has an impact on the aviation environment should be studied for every scenario to ensure safety for the aviation [FAA, 2011].

4.2 Air Traffic Obstacle

In this section the regulations around air traffic obstacles are discussed. Air traffic obstacles are objects that hinder the civil air traffic. Some AWE companies register the current AWE concepts as air traffic obstacles [Salma et al., 2018]. This is to prevent collision with the aviation system. Masts and wind turbines are also often registered as air traffic obstacles. ICAO definition of an "obstacle" is as follows [ICAO, 2009]: “All fixed and mobile objects, or parts thereof, that: are located on an area intended for the surface movement of aircraft; or extend above a defined surface intended to protect aircraft in flight; or stand outside those defined surface and that have been assessed as being a hazard to air navigation”. Even mobile objects can be air traffic obstacles, this is important since AWE systems are often mobile. Furthermore, it is defined by ICAO that the zones around the airports should be obstacle free [ICAO, 2013]. Most AWE applications operate outside the airport zones. In terms of certification ICAO describes the required marking and lighting. Lightning is necessary for obstacles if the height of the system exceeds the altitude of 150m. All in all, Salma et al. (2018) state that AWE can be certified as an air traffic obstacle for the aviation. However, this might reduce the flexibility to move the systems easily to all spaces. This flexibility is one of the big advantages of AWE.

4.3 Hazardous Installations

In this section the regulations around third-party risk of hazardous installations are discussed. The regulations around third-party risk heavily depends per country, in the EU there are no EU wide regulations. In some countries, the regulations even differ per region. There are also no federal wide regulations on third-party risk in the US. Furthermore, there is also a difference in type of regulation. In some countries there is a basic safety limit (BSL). This means that the BSL separates the risks that are tolerated from the risks that are not tolerated under certain conditions [Zielinski and Eng, 2014]. In other countries a basic safety objective (BSO) is set. A BSO separates the risks that are tolerated under certain conditions from the risks that are broadly acceptable or that are considered as negligible [Zielinski and Eng, 2014]. In some countries both BSO and BSL are set. In this section the regulations for a few countries are discussed. In Figure 4.3 an overview of some authorities is given. This overview is made by Zielinski and Eng (2014) during a research on individual and societal risk criteria for safety of dams. A note needs to be made that most of these criteria are from one authority, often for one specific type of risk. The

regulations from Figure 4.3 are considered as examples since for some countries the regulations heavily depend on the region or some countries do not even have any regulations. These examples can be used during the thesis to state whether the risk is acceptable or not.

Country	Annual probability of fatality		Area of application/Regulatory Agency	Individual Risk Measure	Source
	Basic Safety Limit	Basic Safety Objective			
United Kingdom	10^{-4}	10^{-6}	All areas of application within the scope of the Health and Safety at Work Act	Maximum individual risk with accounting for exposure duration allowed	(HSE 2001)
Netherlands*	10^{-6}		Ministry for Housing, Spatial Planning and the Environment Ministry for Transport, Public Works and Water Management	Location-specific individual risk	(VROM 2004) (CCPS 2009)
Hong Kong	10^{-5}		Coordinating Committee on Land use Planning and Control Relating to Potentially Hazardous Installations	Maximum individual risk with accounting for exposure duration allowed	(HK 2012)
Australia	10^{-4}	10^{-6}	New South Wales Dam Safety Committee	Maximum individual risk - accounting for exposure duration not addressed	(NSW DSC 2010)
	0.5×10^{-6}	10^{-6}	New South Wales Department of Planning <ul style="list-style-type: none"> • Hospitals, schools, child-care facilities, old age housing • Residential, hotels, motels, tourist resorts • Commercial developments including retail centres, offices and entertainment centres • Sporting complexes and active open space • Industrial 	Maximum individual risk with accounting for exposure duration allowed	(NSW 2011b)
	5×10^{-6}				
	10^{-5}				
5×10^{-5}					
	10^{-5}	10^{-7}	State of Victoria, Occupational Health and Safety-Major Hazard Facilities	Maximum individual risk - accounting for exposure duration not addressed	(WSV 2011)
Brazil	10^{-4}	10^{-5}	State of Sao Paulo and State of Rio Grande do Soul -pipelines	Not available	(CCPS 2009)
	10^{-5}	10^{-6}	State of Sao Paulo and State of Rio Grande do Soul –fixed facilities	Not available	(CCPS 2009)
USA	1.4×10^{-6}	1.4×10^{-8}	New Jersey Air Quality Permitting Program - cancer risk to public	Not available	(CCPS 2009)
International	10^{-4}	10^{-5}	International Maritime Organization – criteria for passengers and public ashore	Not defined	(IMO 2002) (DNV 2007)

* The legal system in the Netherlands which is based on the Napoleonic law does not allow accommodating of the concept of tolerable risk and ALARP. The law defines precisely what is unjust, unlawful or forbidden

Figure 4.3: Individual risk criteria for several regulatory agencies [Zielinski and Eng, 2014].

Regulations around hazardous installations are mostly on individual risk and FN-curves. Furthermore, due to the chemical accident in Seveso in 1976, European countries are the leaders in third-party risk regulations. Therefore, an overview is made of the individual risk of European countries in Table 4.1. Furthermore, an overview of the regulations on FN-curves of European countries is depicted in Table 4.2. The regulations of Germany, one of the important AWE markets, is not found in literature. Therefore, this section discusses some example countries since countries

deal different with the regulations. It is observed that 63% of the researched countries regulate on individual risk. Furthermore, 83% of the researched countries regulate on the FN-curve. The countries that do not regulate on either the FN-curve or individual risk have developed country specific methods. The FN-curve limitations can also be used as collective ground risk limitations if a hazard leads to maximum one fatality, as stated in section 3.2.

Table 4.1: Overview of individual risk limits within the EU [Gooijer et al., 2011, Pitblado et al., 2012, Trbojevic, 2005].

R_I	UK	The Netherlands	Hungary	Czech Republic	Flanders	Wallonia
10^{-4}	Intolerable					
10^{-5}	ALARP	Existing installations	Upper limit	Existing installations	Hazardous installation	
3×10^{-6}	Limit of acceptability					
10^{-6}	Acceptable level of risk	New installations	Lower limit	New installations	Residential areas	Consultation zone
10^{-7}	Negligible				Vulnerable areas	
10^{-8}		Negligible				

Table 4.2: Overview of FN-curve regulations within the EU [Pitblado et al., 2012, Trbojevic, 2005].

Country	n	C
UK	1	10^{-2}
The Netherlands	2	10^{-3}
Denmark	2	10^{-2}
Czech Republic	2	10^{-4}
Flanders	2	10^{-2}

Netherlands

In the Netherlands regulations are set by the RIVM and are put together in the reference manual Bevi Risk Assessments [RIVM, 2009]. The two common safety risk indicators are used in the Netherlands, individual risk and FN-curve. Next to the regulations on the third-party risk indicators, there are also regulations on the way the quantitative risk assessment is performed. In the reference manual Bevi Risk Assessments it is stated that [RIVM, 2009]: “In order to be able to use the results of a quantitative risk assessment for decisions, they must be verifiable, reproducible, and comparable”.

For new “vulnerable objects” the limit for individual risk is set in the Netherlands at 10^{-6} per year, according to Pitblado et al. (2012). “Vulnerable objects” are firstly residences/areas for children, elderly, or sick/disabled. For example, schools, hospitals, and nursing homes. Secondly, large stores and hotels that have more than 1500m² of floor space are also “vulnerable objects”. Lastly, campground for over 50 people are also “vulnerable objects”. For “less vulnerable objects” the individual risk of 10^{-6} per year is a target value. This target value may be exceeded under certain conditions. Therefore, the ALARP principle is applied in the Netherlands, as discussed in section 3.8. “Less vulnerable objects” are scattered residences (less than two per hectare), small shops, business areas, hotels, recreational objects, and infrastructure objects [Pitblado et al., 2012]. For existing installations the individual risk of 10^{-5} per year is set by the RIVM.

There are also regulations on the FN-curve in the Netherlands. As described in section 3.1, a linear function is established to set a limit for the FN-curve with a defined C and α . For this criteria curve certain guide values are used [Gooijer et al., 2011]. The authority involved should account for the height of the societal risk in relation to social-economic benefits. Therefore, the FN-curve is not a strict regulation. The parameters of the FN-curve limitation equation in the Netherlands are depicted in Table 4.2.

United Kingdom

The regulations around risk assessment of major hazard facilities are complex and nuanced in the United Kingdom, according to Pitblado et al. (2012). The regulatory body for major hazard facilities in the United Kingdom is the Health & Safety Executive (HSE). The HSE has a statutory role for enforcement with major hazard installations. The individual risk criteria for the United Kingdom are depicted in Table 4.1. An important safety risk indicator for the United Kingdom is the FN-curve. The FN-curve parameters of the United Kingdom are depicted in Table 4.2. The United Kingdom use a so called “three band approach” which is depicted in Figure 4.4. The United Kingdom has two criteria curves to limit the FN-curve instead of one. The area above the two lines is the intolerable region, which is the same for the Dutch approach. However, in the area between the criteria curves the ALARP principle applies [Pitblado et al., 2012].

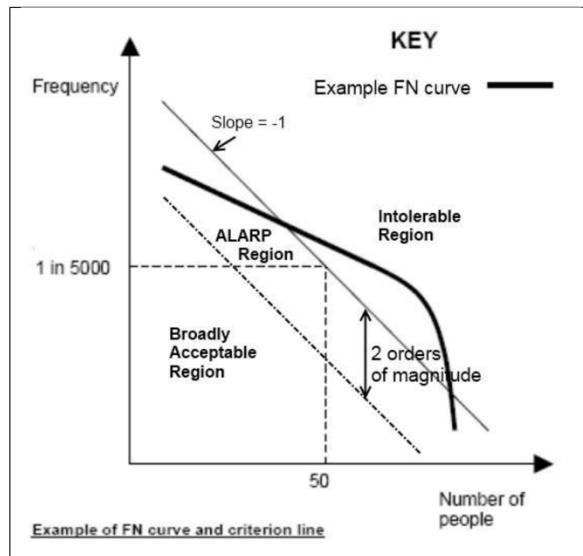


Figure 4.4: Example of an FN-curve and the three band approach made by Pitblado et al. [2012].

A quantitative risk assessment is needed to generate an FN-curve, this is time consuming. Therefore, the HSE has developed several alternative methods [Carter et al., 2002, Hirst and Carter, 2002]. One of the methods developed by HSE is the risk integral. The risk integral is depicted in Equation 4.1.

$$RI = \sum f_i N_i^\alpha \quad (4.1)$$

Where f_i is the frequency of outcome i , N_i is the number of fatalities resulting from outcome i , and α is the scale aversion factor. The scale aversion factor means that it depends on the measure being computed. For example, for the potential loss of life α is set to 1. In Figure 4.5 the limits for the risk integral are depicted.

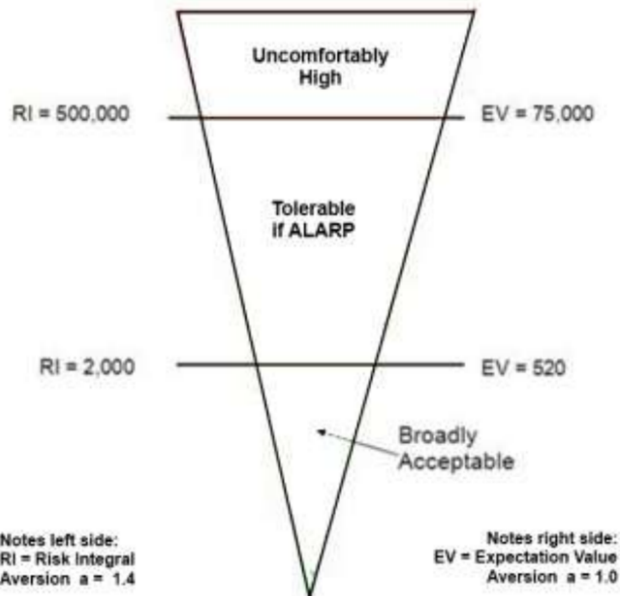


Figure 4.5: UK societal risk regulations [Pitblado et al., 2012].

Belgium

In Belgium the land use planning policy is regional performed. Therefore, the country is divided in three regions Flanders, Walloon, and Brussels. Only Walloon and Flanders have third-party risk regulations in place. Furthermore, it is unfeasible that Kitepower will operate in the city of Brussels.

Flanders

The main criteria for third-party risk regulations in Flanders is individual risk, according to Pitblado et al. (2012). However, also the FN-curve is used as a safety risk criterion. The criteria are the same for existing and new installations. For individual risk there are three limits. Firstly, the maximum individual risk on the hazardous installation boundary line is 10^{-5} . Secondly, at residential areas the limit of the individual risk is set at 10^{-6} . Lastly, at vulnerable areas the limit of individual risk is set at 10^{-7} . The criterion around the FN-curve are depicted in Figure 4.6 with the parameters in Table 4.2. A clear description must be given of the technical and organizational measures taken to prevent the most important accident scenarios if the criteria of societal or individual risk are not met. Furthermore, additional safety measure might be required. A safety information plan needs to be made if the criterion of the boundary line of the individual risk is not met. This is a formal agreement between the major hazard installation and the surrounded area [Pitblado et al., 2012].

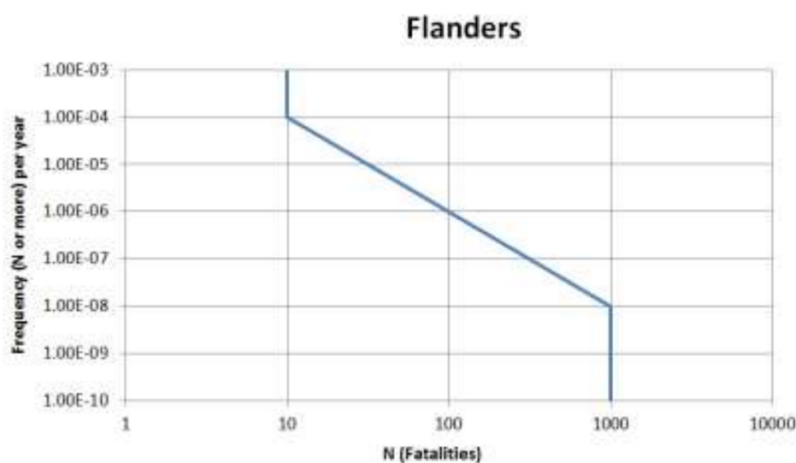


Figure 4.6: FN-curve criterion for Flanders made by Pitblado et al. [2012].

Wallonia

In Wallonia the safety risk indicator that is used to quantify the third-party risk is individual risk, societal risk is not taken into account according to the Gooijer et al. (2011). The area with individual risk higher than 10^{-6} is called the consultation zone [Gooijer et al., 2011]. Inside this zone the advice from the competent authority must be taken into account for every hazardous installation. The authority bases its advice on the matrix depicted in Figure 4.7.

	Individual risk (risk of irreversible damage)		
	10^{-3} to 10^{-4} per year	10^{-4} to 10^{-5} per year	10^{-5} to 10^{-6} per year
Type A: Buildings and technical units directly linked with the geography (catchment, water tower, wastewater treatment, windmill, et cetera)	OK	OK	OK
Type B: Buildings for a few people, for the most part adult and autonomous (workshop, logistic units, small shops, et cetera)	With caution	OK	OK
Type C: Buildings for people, for the most part adult and autonomous, but without number restriction (accommodation, workshops or offices for more than 100 people, schools and dormitories for students aged 12 and over, et cetera)	Not allowed	With caution	OK
Type D: Buildings for susceptible people, with restricted autonomy (hospitals, rest homes, schools and dormitories for children under 12, prisons, et cetera)	Not allowed	Not allowed	With caution

Figure 4.7: Matrix for decision-making in the consultation area in Wallonia [Gooijer et al., 2011].

Ireland

In Ireland the Health and Safety Authority (HSA) is the authority that regulates hazardous installations. In 2003 an approach to land use planning was developed [Pitblado et al., 2012]. This plan was developed to provide a high level of protection. In Ireland the main criteria are on societal risk. The HSA uses the British integrated risk. The HSA uses a scale aversion factor of 1.4 and an integrated risk of 2000 is considered to be acceptable. An integrated risk of 500.000 is regarded as significant. An FN-curve can also be included and used by the considerations of the HSA. No strict FN-curve limits are specified by the HSA, according to Pitblado et al. (2012).

France

In France there are two tools used to decide on the risk acceptability. Firstly, the “Matrice de Mesure de Maitrise des Risques” (MMR) is used. This matrix depicts the risk level of an accident based on a combination of the probability of occurrence and its severity. The severity is based on the persons exposed and not on fatalities [Gooijer et al., 2011]. In Figure 4.8 the MMR matrix is depicted. There are three regions in the MMR matrix. Firstly, the acceptable areas which is marked green. Secondly, the ALARP region where operators should continuously improve the safety of their installation. Lastly, the unacceptable area, in this area operators should implement new safety measures [Gooijer et al., 2011].

Probability Severity	E ($0-10^{-5}$ y)	D ($10^{-5}-10^{-4}$ y)	C ($10^{-4}-10^{-3}$ y)	B ($10^{-3}-10^{-2}$ y)	A ($10^{-2}-1$ y)
Disastrous	ALARP/ Unacceptable	Unacceptable	Unacceptable	Unacceptable	Unacceptable
Catastrophic	ALARP 2	ALARP 2	Unacceptable	Unacceptable	Unacceptable
Significant	ALARP	ALARP	ALARP 2	Unacceptable	Unacceptable
Serious	Acceptable	Acceptable	ALARP	ALARP 2	Unacceptable
Moderate	Acceptable	Acceptable	Acceptable	Acceptable	ALARP

Figure 4.8: The risk matrix of France (MMR) [Gooijer et al., 2011].

The second tool is the “Plan de Prévention des Risques Technologiques” (PPRT). This method creates dangerous maps according to a specific governance process. In these maps there are different dangerous levels, these are depicted in Figure 4.9. Kooi et al. (2011) describe the process of establishing the risk zones. The red, orange, and yellow zones are prevented because the risk is not acceptable in these regions [Pitblado et al., 2012].

Maximum intensity	Significant lethal	Lethal	Irreversible	In-direct						
Cumulative probability	D	5E to D	<5E	>D	5E to D	<5E	>D	5E to D	<5E	All
'aléa levels'	VH+	VH	H+	H	M+	M	Low			

Figure 4.9: Danger levels of the PPRT [Gooijer et al., 2011].

Abu Dhabi

The authority that regulates risk in Abu Dhabi is the Abu Dhabi National Oil Company (ADNOC), this company is both the national oil company as the regulating authority. ADNOC has both individual risk and societal risk criteria. ADNOC uses the British approach to set criteria for societal risk with the three band approach, unacceptable, ALARP, and acceptable. In Figure 4.10 the FN-curve criterion is depicted. Currently, no societal risk criteria are in place for offshore facilities. Kitepower has a big opportunity in off shore wind energy, this regulation gap gives opportunities [Pitblado et al., 2012].

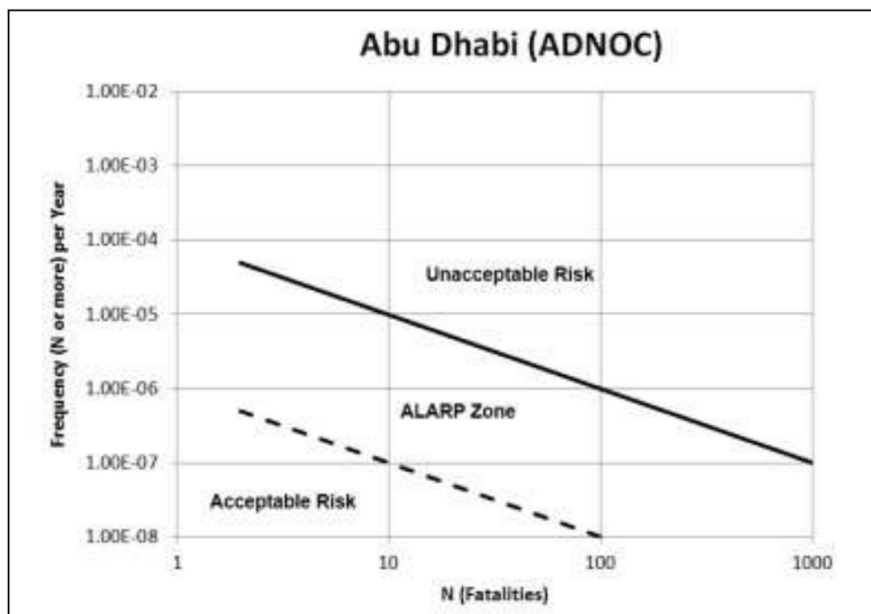


Figure 4.10: FN-curve criterion of ADNOC [Pitblado et al., 2012].

Brazil

Risk is regulated in Brazil on both federal and state level. On state level regulations are only in place for certain types of installations. The general risk assessment methods and criteria differ per state. Pitblado et al. (2012) describe the different quantitative risk assessment methods per state. Rio de Janeiro, São Paulo, Rio Grande do Sul, and Bahia State have developed guidelines for the risk assessment. The other states mostly use the method and criteria of São Paulo. All the states only regulate on societal risk. In all states FN-curve criteria were set in the British way, the three band approach. However, the values for the FN-curve differ per state as depicted in Figure 4.11.

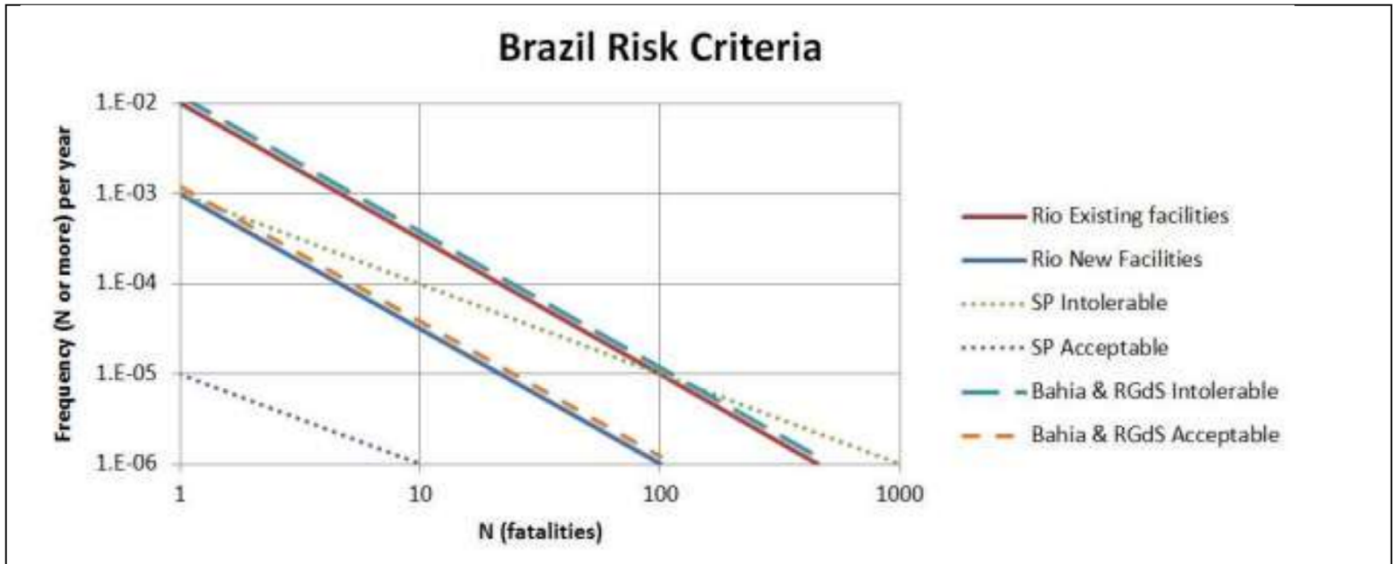


Figure 4.11: State FN-curve criteria in Brazil [Pitblado et al., 2012].

5 Agent-based Approach

In this chapter the safety risk assessment is started, now all the needed background knowledge is explained in the previous chapters. The system is explained as an agent-based model as a first step of the safety risk assessment. In this model there are eight agents identified for the Kitepower operations. The agents are defined as follows:

- **Environment:** The environment is a non-agent that represents the external influence on the complete system. The most important factor is the wind. A non-agent is an agent that may be influenced by its environment, but does not perceive it [Blom, 2018-2019].
- **Kite:** The kite is a reactive agent that consists of the kite. The kite includes the bridle system but excludes the safety line, IMU, GPS, and pump.
- **Tether:** The tether is a reactive agent that consists of the tether, weak link, and safety line.
- **KCU:** The KCU is a proactive agent that consists of the KCU, redundant safety release mechanism, and the sensors of the kite. These sensors are the IMU, GPS, and the pump.
- **5 GHz WIFI link:** The WIFI link is a reactive agent that represents the communication link between the KCU and the ground station.
- **Weather sensor:** The weather sensor is a reactive agent that measures the wind from the environment.
- **Ground station:** The ground station is a proactive agent that consists of all components of the ground station, as described in chapter 2, and the display in the caravan.
- **Field team:** The field team is a proactive agent that consists of the two humans in the field.
- **Caravan team:** The caravan team is a proactive agent that consists of the human in the caravan.

The interaction of the agents are depicted in Figure 5.1. All the agents are discussed in a separate section in this chapter.

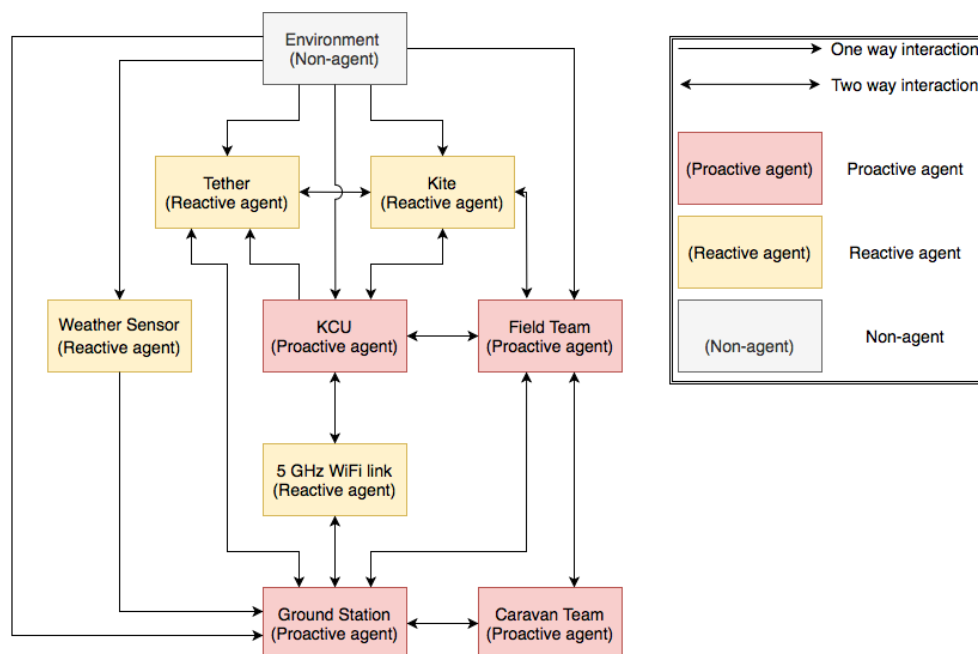


Figure 5.1: Schematic display of Kitepower as a multi agent system.

5.1 Environment

In this section the non-agent that represents the environment is introduced. The environment has several state variables in real life, such as the temperature, the wind vector, the humidity, and the visibility. This influences the complete system with for example, dust/sand wearing out the system, corrosion in mechanical components, or the temperature influencing the batteries.

Assumption 5.1: The environment only influences the system in the model with the wind vector.

Due to assumption 5.1 the only state variable of the environment is the wind vector $v_{wind,t}^{i,k}$.

5.2 Kite

In this section the state variables and local modes of the kite are introduced. Furthermore, the interaction between the kite and the environment are discussed. The kite has the following state variables:

- **Orientation:** The orientation of the kite is present in three dimensions: roll angle (ϕ), pitch angle (θ), and yaw angle (ψ).
- **Turn rate:** The turn rate of the kite is present in three dimensions: roll rate (p), pitch rate (q), and yaw rate (r).
- **Angle of attack (α)**
- **Side slip angle (β)**
- **Position:** The position is measured in three directions: x , y , and z direction.
- **Velocity:** The velocity is also measured in three directions: x , y , and z direction.
- **Acceleration:** The acceleration is also measured in three directions: x , y , and z direction.
- **Bridle forces**
- **Relative depower:** The relative depower represents the length of the bridle lines that influence the depower state, the depower tapes.
- **Relative steering:** The relative steering represents the length of the bridle lines that influence the steering, the steering tapes.

The orientation, turn rate, angle of attack, side slip angle, position, velocity, and acceleration are measured by the sensors in the kite. These sensors are not part of the kite but part of the KCU agent. The bridle forces, relative depower, and relative steering are measured at the KCU. The kite also has local modes. There are eight local modes identified for the kite. These are defined as follows:

- **Launching mode:** In the launching mode, the kite is launched from the ground. The kite is stabilised by the KCU and the loads are transferred via the bridle system to the tether.
- **Reel-out mode:** In the reel-out mode, the kite flies a figure of eight. The radial distance to the ground station increases during this mode.
- **First transition mode:** In the first transition mode, the kite reduces the angle of attack. Furthermore, the kite flies to the highest point of the operation, pointtozenith. The radial distance to the ground station is constant during this mode.
- **Reel-in mode:** In the reel-in mode, the kite is retracted with a small angle of attack. The radial distance to the ground station decreases during this mode.
- **Second transition mode:** In the second transition mode, the kite increases the angle of attack. Furthermore, during the second transition mode the radial distance to the ground station is constant again.

- **Landing mode:** In the landing mode, the kite is landed according to the procedure described in chapter 2. The kite is at the ground at the end of this mode.
- **Parking mode:** In the parking mode, the kite reduces the angle of attack and parks the kite in the air. The kite is located at a constant location. The radial distance to the ground station is constant during this mode.
- **Emergency landing mode:** In the emergency landing mode, the kite is in a gliding configuration because the safety line is under tension and the front tube suspension is not attached to the tether anymore. The kite is stabilised by the KCU. The loads are transferred via the safety line to the tether. The tether is retracted and the kite is landed.

Interaction Environment and Kite

The environment has several effects on the kite. However, only the wind vector is assumed to be relevant as explained in assumption 5.1. The wind vector has a large influence on the velocity vector of the kite and the location of the kite. Furthermore, gusts influence the orientation, turn rate, side slip, angle of attack, position, velocity, and acceleration of the kite. Next, there are also other environmental factors that influence the kite. However, these are negligible compared to the impact of the wind. An example of this other factor is the temperature. The temperature influences the strength of the kite since there is pressurised air in the kite. However, assumption 5.1 neglects these effects.

5.3 Tether

In this section the state variables and local modes of the tether are introduced. Furthermore, the interactions between the tether and the other agents are discussed. The tether agent consists of the tether, weak link, and the safety line. The kite has the following state variables:

- **Tether force**
- **Tether length**
- **Tether mass**
- **Tension safety line:** If the safety line is under tension either the redundant safety release mechanism, part of the KCU agent, or the weak link, part of the tether agent, is activated.

The tether length and tether force are measured at the ground station. The tension in the safety line is not measured. However, the safety line is tensioned if the weak link or the redundant safety release mechanism is activated. The tether has three different local modes:

- **Reel-in mode:** In the reel-in mode, the tether length is reduced.
- **Reel-out mode:** In the reel-out mode, the tether length is increased.
- **Constant mode:** In the constant mode, the tether length is held constant.

Interaction Environment and Tether

The interaction between the tether and environment is neglected during the modelling of the kite. However, in real life the environment does have influence on the tether, such as UV radiation, dust/sand wear, and temperature effects.

Interaction Kite and Tether

The interactions between the tether and the kite are mainly forces. The tether transfers forces between the kite and the ground station. This is the tether its main function. The forces between the kite and tether are transferred via the bridle system in the normal operation situation. In the emergency situation the forces between the kite and tether are transferred via the safety line.

5.4 KCU

In this section the main functions, state variables, and local modes of the KCU are introduced. Furthermore, the interactions between the KCU and the other agents are discussed. The KCU has the following main functions:

- **Steering the kite:** The KCU steers the kite via its two winches.
- **Control the kite:** The KCU controls the kite its flight path. The KCU adapts the flight path if needed. It is the control centre of the system.
- **Health analyser of the system:** The KCU constantly analyses the health of the 5 GHz WIFI link. If the link is not working, the KCU takes over the health analysis of the KCU and the kite.
- **State estimator of the kite:** The ground station estimates its own future state.

The KCU has the following state variables:

- **Main battery charge**
- **Voltage of main battery**
- **Electric current of main battery**
- **Safety release mechanisms battery charge:** Both safety release mechanisms have their own battery. These batteries are also charged by the wind turbine of the KCU.
- **Voltage of safety release mechanisms batteries**
- **Electric current of safety release mechanisms batteries**
- **Voltage of wind turbine**
- **Electric current of wind turbine**
- **Magnetic flux of wind turbine**
- **Torque depower winch**
- **Electric current depower winch**
- **Torque steering winch**
- **Electric current steering winch**

All these state variables are measured by the KCU itself. The local modes of the KCU are the same as the kite. The KCU has the following local modes:

- **Launching mode:** In this mode, the KCU follows the launch path programmed in the flight path controller.
- **Reel-out mode:** In this mode, the KCU follows the figure of eight programmed in the flight path controller.
- **First transition mode:** In this mode, the KCU rotates the depower winch to decrease the angle of attack.
- **Reel-in mode:** In this mode, the KCU keeps both winches still. Only for stabilisation purposes the steering winch is used.
- **Second transition mode:** In this mode, the KCU rotates the depower winch to increase the angle of attack.
- **Landing mode:** In this mode, the KCU follows the landing path programmed in the flight path controller.
- **Parking mode:** In this mode, the KCU parks the kite in the air. The KCU first uses the depower winch to decrease the angle of attack. Next, the KCU only uses the steering winch to stabilise the kite.
- **Emergency landing mode:** In this mode, the KCU agent separates the tether and the KCU by initiating the redundant safety release mechanism or the weak link, part of the tether

agent. In this situation, the KCU is only attached via the bridle system to the rest of the system. The KCU stabilizes and steers the kite in this emergency landing mode.

Interaction Environment and KCU

The interaction between the KCU and environment is neglected during the modelling of the kite. However, in real life the environment does have influence on the KCU. Such as UV radiation, dust/sand wear, and temperature effects.

Interaction Tether and KCU

The only interaction between the KCU and the tether is the redundant safety release mechanism. The redundant safety release mechanism is activated if the system decides that the tether needs to be separated from the bridle system. In this situation the safety line becomes tensioned and the KCU hangs directly under the kite without an attachment to the tether.

Interaction Kite and KCU

The kite and KCU only interact via forces. The kite and KCU interact via the forces on the bridle system. Therefore, there is interaction via two ways. Firstly, the interaction via the steering tapes, the length of the steering tapes are changed by changing the torque of the steering winch of the KCU. This influences the heading of the kite. Secondly, the interaction via the depower tape, the length of the depower tape is changed by changing the torque of the depower winch of the KCU. This influences the angle of attack of the kite.

5.5 5 GHz WIFI Link

In this section there is elaborated on the 5 GHz WIFI link. The different modes are discussed and the interaction with the KCU is discussed. The 5 GHz WIFI link transfers all the information between the KCU and ground station. The 5 GHz WIFI link has therefore two modes:

- **Connected:** In the connected mode there is a healthy connection between the KCU and the ground station via the 5 GHz WIFI link. In this mode all the information is transferred between the KCU and the ground station via the 5 GHz WIFI link.
- **Disconnected:** In the disconnected mode there is no connection between the KCU and the ground station via the 5 GHz WIFI link. The KCU tries to find and connect to the 5 GHz WIFI link.

Interaction KCU and 5 GHz WIFI Link

The 5 GHz WIFI link interacts with the KCU in two ways. Firstly, the 5 GHz WIFI link transfers the information received from the ground station to the KCU. Secondly, the 5 GHz WIFI link receives the information from the KCU that needs to be transferred to the ground station.

5.6 Weather Sensor

The weather sensor is only influenced by the environment. The weather sensor measures wind vector $v_{wind,t}^{i,k}$. This information is communicated to the ground station by a cable. Therefore, it is a reactive agent since it only reacts to the environment. The weather sensor is located close to the ground station.

5.7 Ground Station

In this section the main functions, state variables, and local modes of the ground station are introduced. Furthermore, the interactions between the ground station and the other agents are discussed. The ground station is an agent with several functions. The ground station has the following main functions:

- **Tether control:** The ground station continuously analyses if the tether force and reeling velocity is not too low or too high.
- **Electrical energy generation:** The ground station generates energy by the generator when the tether is reeled out.
- **Physical energy provision:** The ground station retracts the tether by the generator when the tether is reeled in.
- **Health analyser of the system:** The ground station constantly analyses the health of all components of the system.
- **State estimator of the ground station:** The ground station estimates its own future state.
- **Receiving commands:** The display in the caravan is part of the ground station agent. Commands are entered on this display. The following commands can be entered:
 - **Launch:** The launch mode is activated by entering launch on the display if the kite is on the ground. The kite launches as described in section 2.3.
 - **Landing:** The landing mode is activated by entering landing on the display. In this situation the kite lands as described in section 2.3.
 - **Emergency landing:** The emergency landing mode is activated by entering emergency landing on the display. In this situation the safety release is activated and the emergency line becomes tensioned. The kite lands by an emergency landing as described in section 2.3.
 - **Parking:** The parking mode is activated by entering parking on the display. In this situation the kite is parked as described in section 2.3.
- **Displaying information:** On the display all the measurements are found. In Figure 5.2 an example menu is depicted. In Figure 5.2 the following is depicted:
 - **Top left menu:** The top left menu is a system monitor that displays the state of the different subsystems of the ground station and KCU.
 - **Top middle menu:** The top middle menu depicts the following:
 - The situation at the ground station, including the wind speed, wind direction, and the position of the ground station.
 - The state variables of the KCU, including the position and battery level.
 - The current path of the kite.
 - The loaded paths of the kite.
 - **Top right menu:** The power setting of the kite. In this menu it is displayed how much the kite is powered and steered by the KCU.
 - **Centre menu:** The centre menu consists of three different windows:
 - Top view: This menu depicts the position of the kite from above, centred around the ground station.
 - Front view: This menu depicts the position of the kite in the hemisphere around the ground station.

- **Headings:** This menu depicts the heading of the kite that is received from the three heading sensors.
- **Bottom middle menu:** The bottom middle menu is the data display. The data display consists of the wind speed at the ground, the azimuth of the kite, the elevation of the kite, the heading of the kite, the battery level of the KCU, the tether force at the winch, the reel-out speed, and the tether length.
- **Bottom right menu:** The bottom right menu is also a system monitor that displays the state of the different systems and sensors.

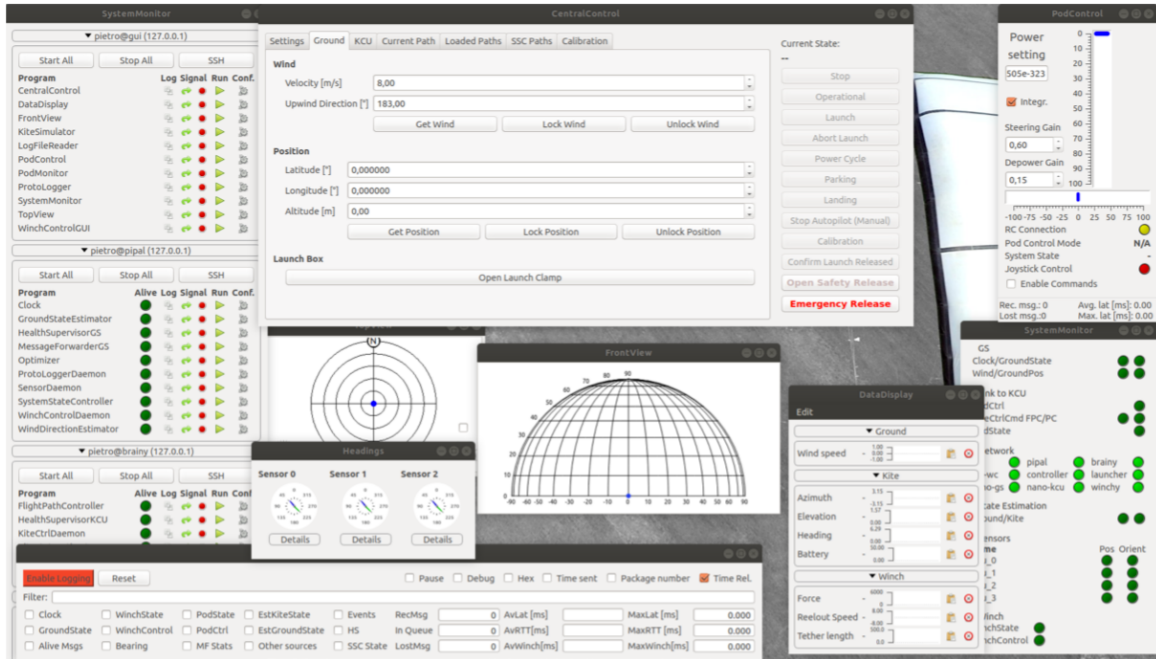


Figure 5.2: Overview of the ground station's display.

The ground station has the following state variables:

- **Winch speed:** The rotating speed of the winch.
- **Mechanical power:** The mechanical power of the winch.
- **Mechanical energy:** The mechanical energy of the winch.
- **Electrical power:** The electrical power generated or used by the generator.
- **Electrical energy:** The electrical energy generated or used by the generator.

All these states are measured by internal sensors. The local modes of the ground station are the same as the kite. The ground station has the following local modes:

- **Launching mode:** In this mode, the ground station is always ready to reel-in the tether if there is no or too little tension on the tether.
- **Reel-out mode:** In this mode, the ground station reels-out the tether. The generator is activated and generates electrical energy.
- **First transition mode:** In this mode, the winch is stopped. The tether length is held constant. The tether is reeled in by the generator if the tether force is too low.
- **Reel-in mode:** In this mode, the ground station reels-in the tether. The generator is activated and supplies mechanical energy.
- **Second transition mode:** In this mode, the winch is stopped. The tether length is held constant. The tether is reeled in by the generator if the tether force is too low.

- **Landing mode:** In this mode, the tether is reeled in by the winch according to the orders of the KCU.
- **Parking mode:** In this mode, the winch is stopped. The tether length is held constant. The tether is reeled in only if the tether force is too low.
- **Emergency landing mode:** In this mode, the tether is reeled in by the winch. If there is still a connection between the KCU and ground station, the ground station receives orders from the KCU.

Interaction Environment and Ground Station

The interaction between the ground station and environment is neglected in the agent-based model. However, in real life the environment does have influences on the ground station, such as UV radiation, dust/sand wear, and temperature effects.

Interaction Tether and Ground Station

There are two interactions between the tether and ground station. The first interaction between the ground station and the tether is the tether force. The kite pulls the tether due to its aerodynamic forces. The winch of the ground station also generates a pulling force, either to retract the kite or to generate energy. The second interaction between the ground station and the tether is the length of the tether. The tether length is controlled by the ground station. The tether length also influences the mass of the tether.

Interaction Weather Sensor and Ground Station

The interaction between the weather sensor and the ground station is performed via a cable. Via this cable the wind vector is communicated from the weather sensor to the ground station. The heading and velocity of the wind is used by the ground station.

Interaction 5 GHz WIFI Link and Ground Station

The 5 GHz WIFI link interacts with the ground station in two ways. Firstly, the ground station transfers the information received from the KCU to the ground station. Secondly, the 5 GHz WIFI link receives the information from the ground station that needs to be transferred to the KCU.

Interaction KCU and Ground Station via 5 GHz WIFI Link

The interaction between the KCU agent and ground station agent only consists of communication, this is performed via the 5GHz WIFI link agent. Three different types of information are communicated. Firstly, the measured state variables of all components are communicated to both agents. Secondly, orders from the flight path controller are communicated to the winch control daemon. Lastly, if one of the health supervisors detects an anomaly, the operational mode of the entire system is switched. This mode change is also communicated between the KCU and ground station.

5.8 Field Team

The field team is an agent that represents the humans in the field. In this section the exact tasks are explained of the field team. Furthermore, there is elaborated on the interaction with the other agents. The field team always stands in the field. Before launch the field team prepares the ground station, kite, and KCU. Furthermore, the field team checks the complete system in the field by the cross checking principle. During and after launch the field team monitors the system and the environment. The field team intervene physically to the ground station if needed. The field team communicates the observations to the caravan team if actions are needed, for example, the mode needs to be changed. The field team secures the kite and packs the complete system during landing. Therefore, the field team interacts with the environment, kite, KCU, ground station, and caravan team. All these interactions are explained in more detail in this section.

Interaction Environment and Field Team

The interaction between the environment and field team mainly consists of visual observation. For example, the field team observes the local weather conditions. This is performed by the human eyes from the field team and observing weather data.

Interaction Kite and Field Team

The interaction between the kite and field team consists of three parts. Firstly, the kite is prepared and checked for the launch by the field team. The field team rolls out the tether and attaches everything correctly. At the end, the field team performs safety checks. Secondly, the field team observes the kite during launch, normal operation, and landing. Lastly, the field team secures the kite and clears up the kite after landing.

Interaction KCU and Field Team

The interaction between the KCU and field team consists of three parts. Firstly, the KCU is prepared and checked for the launch by the field team. The field team attaches the KCU to the rest of the system and inserts the battery. At the end, the field team performs safety checks. Secondly, the interaction between the field team and the KCU consists of the observation of the KCU by the field team during launch, normal operation, and landing. Lastly, the field team clears up the KCU after landing.

Interaction Ground Station and Field Team

The interaction between the ground station and field team consists of three parts. Firstly, the ground station is prepared and checked for the launch by the field team. At the end, the field team performs safety checks. Secondly, the field team observes the ground station during launch, normal operation, and landing. Furthermore, the field team can physically take action if needed in an abnormal situation. The field team also receives updates via Telegram from the ground station. Lastly, the field team clears up the ground station after landing.

5.9 Caravan Team

The caravan team is an agent that represents the human in the caravan. In this section the exact tasks are explained of the caravan team. Furthermore, there is elaborated on the interaction with other agents. The caravan team is the control room of the operation. The main decisions made in the operation by humans are performed by the caravan team. The caravan team interacts with the ground station and field team. The field team interacts with the caravan team by voice. Secondly, the caravan team communicates with the ground station via the display. These interactions are explained in more detail in this section.

Interaction Field Team and Caravan Team

The interaction between the field team and caravan team consists of voice communication via a radio connection. The interaction between the field team and caravan team consists of the following communication:

- **Setup checks before lifting:** The field team communicates the setup checks before lifting to the caravan team. The list of setup checks before lifting are depicted in Figure 5.4. Lifting means that the kite stands upright but is still at the ground and attached to the launch system.
- **Lifting:** The caravan team communicates to the field team when the kite is lifted.
- **Setup checks after lifting:** The field team communicates the setup checks after lifting to the caravan team. The list of setups checks after lifting are depicted in Figure 5.5 and Figure 5.6.
- **Launch:** The caravan team communicates the moment of launch to the field team.

- **System monitoring:** The caravan team and field team constantly communicate their observation of the system to each other.
- **Landing:** The caravan team communicates to the field team if the landing button is pressed. During landing the observations of the caravan team and field team are constantly communicated to each other.
- **Kite secured:** The field team communicates to the caravan team when the kite is secured to the ground by the field team.

Interaction Ground Station and Caravan Team

The main interaction between the caravan team and the ground station is the display of the ground station. All the measured state variables are depicted on this display. However, in Figure 5.2 an example overview of the ground station's display is depicted with its most important information. Figure 5.2 is clarified in section 5.5. The interaction between the caravan team and the ground station consists of the following:

- **Hardware checks:** The hardware checks are performed by the caravan team by pushing buttons on the display depicted in Figure 5.3. The following checks are performed:
 - **Sensors**
 - **Pressure in the kite**
 - **KCU motors**
 - **Emergency release:** With this button the emergency landing mode is started.

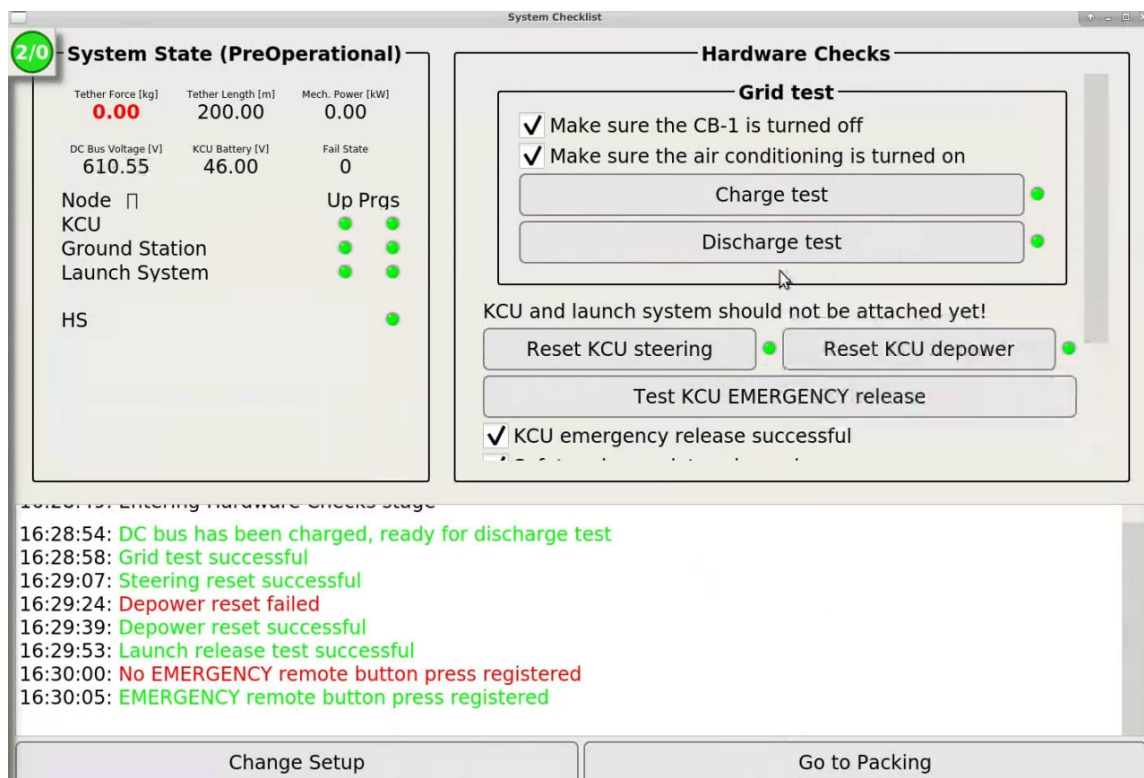


Figure 5.3: Display overview of hardware checks.

- **Setup checks before lifting:** The setup checks before lifting are performed and communicated by the field team and are entered in the display. In Figure 5.4 an overview of this display is depicted. The caravan team enters "Continue and enter Operational" after these checks are entered in the system.

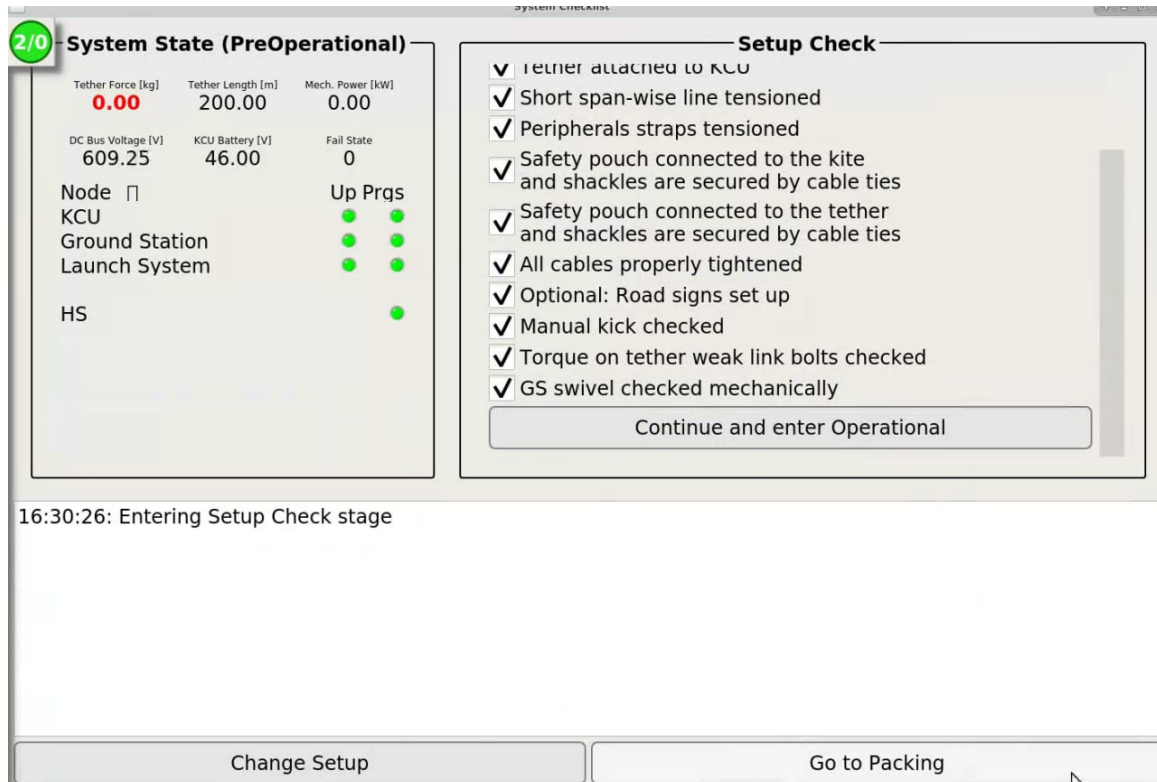


Figure 5.4: The display overview of the setup checks performed by the field team before the kite is lifted.

- **Press lift kite:** The kite is lifted by pressing “Lift kite” on the display after performing the last checks before lifting. This display is depicted in Figure 5.5.

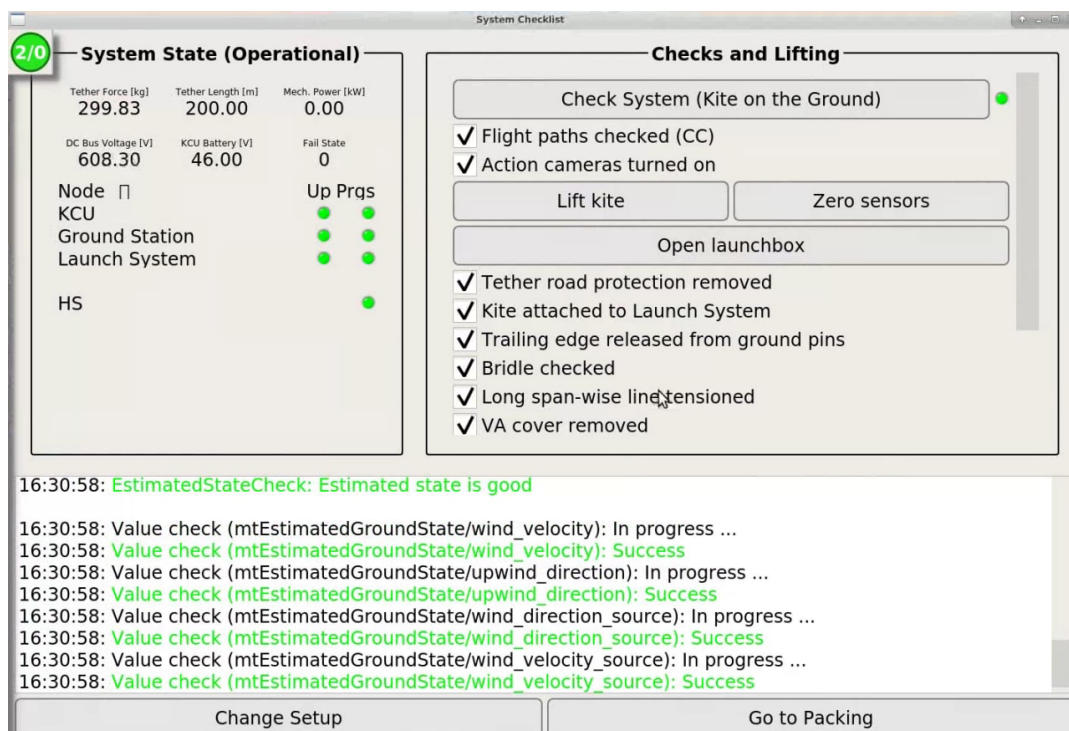


Figure 5.5: The first display overview of the setup checks performed by the field team after the kite is lifted.

- **Setup checks after lifting:** The setup checks after lifting are performed and communicated by the field team and are entered in the display. In Figure 5.5 and Figure 5.6 an overview of this display is depicted. The caravan team enters “Continue to Launch” after these checks are entered in the system.

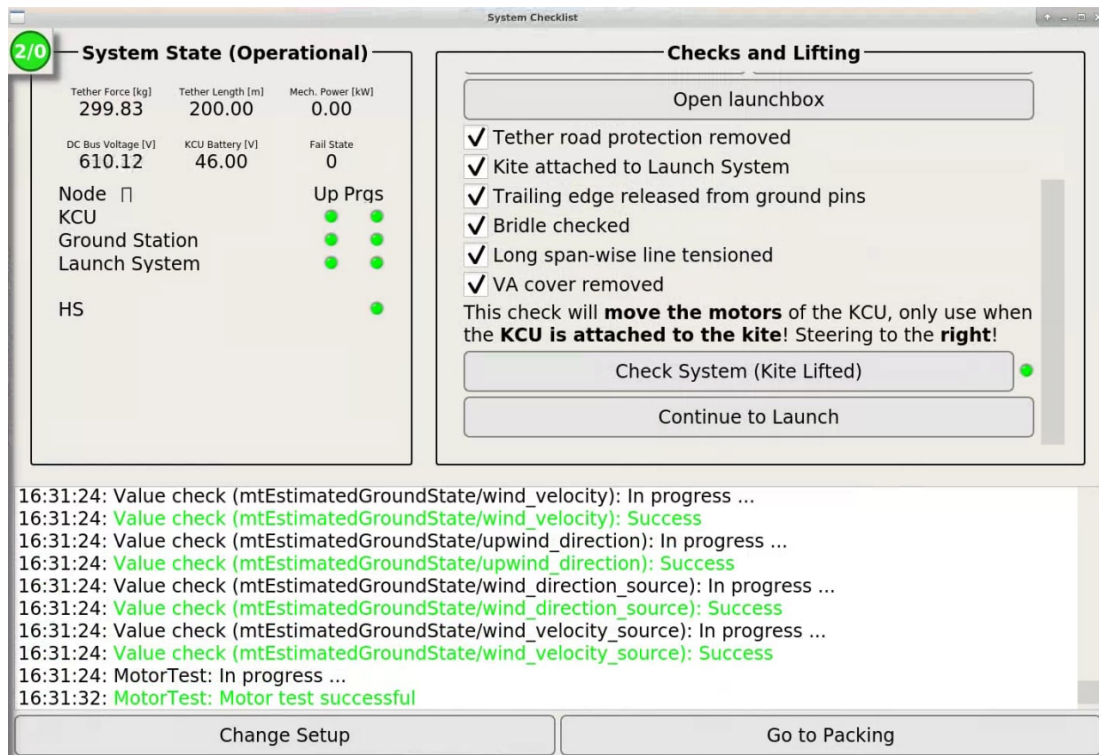


Figure 5.6: The second display overview of the setup checks performed by the field team after the kite is lifted.

- **Press launch:** The caravan team orders to launch the kite on the display as depicted in Figure 5.7.

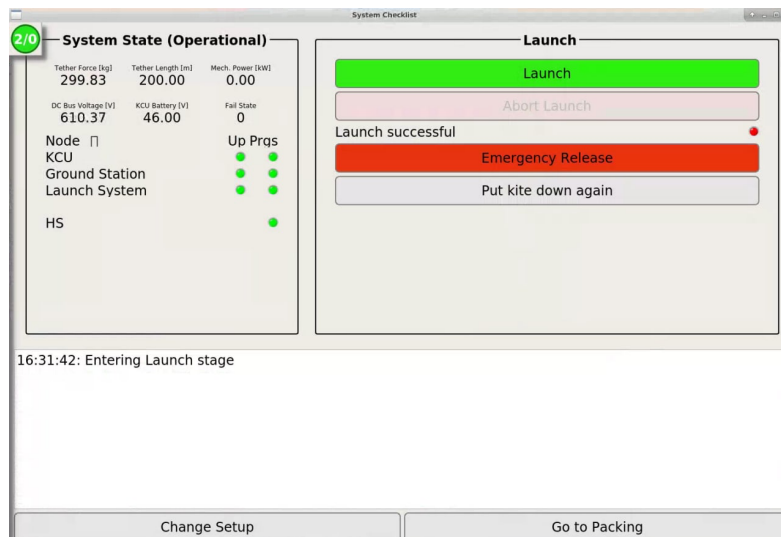


Figure 5.7: Overview of launch display.

- **Monitor the system:** All the flight parameters are monitored during the operation by the caravan team. This display is depicted in Figure 5.8. However, the most important flight parameters are:
 - Tether force
 - Tether length
 - Wind direction
 - Wind speed

If the caravan team recognizes that these flight parameters are exceeding the limits the caravan team changes the setting of the kite via the display depicted in Figure 5.8. The setting changes could be a higher elevation angle, a change in figure eight from down loops to up loops, parking, or even an emergency landing mode can be initiated.

- **Press “Land Left” or “Land Right”:** If there is decided that the kite should be landed by the caravan team. The caravan team needs to press “Land Left” or “Land Right” on the display, as depicted in Figure 5.8.

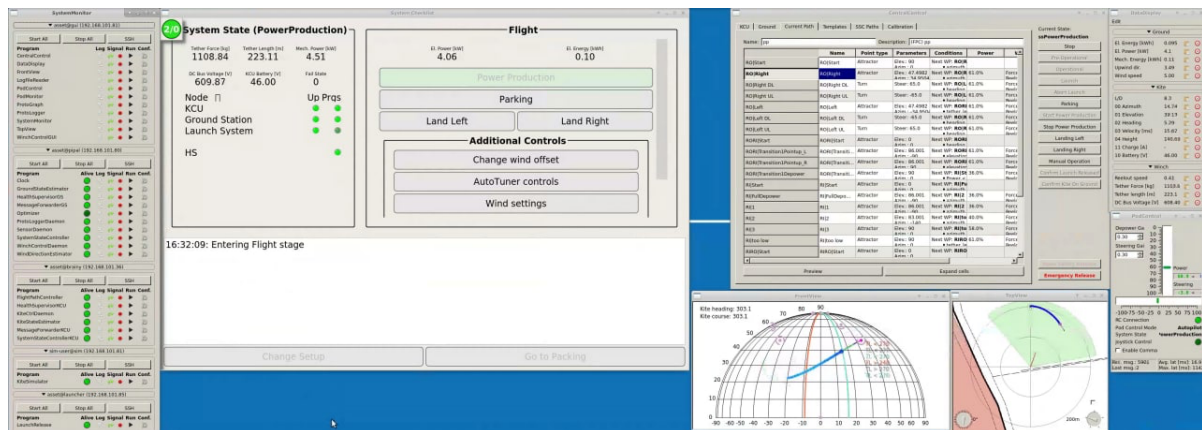


Figure 5.8: Overview of the display during operation.

6 Scenario Identification

In chapter 5 the first step of the safety risk assessment is performed, namely describing the system as an agent-based system. The second step is the hazard identification and safety-relevant scenario generation. These steps are performed in this chapter. Safety-relevant scenarios are scenarios where the kite could harm third-parties. This is the situation in which the kite is outside the operational zone, the circle of 400m around the ground station. To obtain these scenarios a hazard brainstorm is performed. The hazards from the hazard brainstorm and the top-events of the FTA and FMEA performed by Salma et al. (2019) are used. All these hazards are merged in section 6.1 and pre-processed in section 6.2. Next, in section 6.3 the potential safety-relevant scenarios are identified. Subsequently, in section 6.4 the crystallization of the hazards is performed according to the method of Blom (2018-2019). In section 6.5 the consequences of the identified scenarios are discussed. Lastly, the findings are compared with the FTA and FMEA performed by Salma et al. (2019) in section 6.6.

6.1 Hazard Merge

In this section all the hazards are merged in Table 6.1. The hazards are obtained from the performed hazard brainstorm and from an already performed FTA by Salma et al. (2019). Firstly, the hazard brainstorm with operational experts is performed. The hazards generated during the hazard brainstorm that could result in the kite leaving the operational zone are added to Table 6.1. Secondly, the basic events of the top fault tree from Salma et al. (2019), depicted in Figure 6.1, are included in Table 6.1 as well. This results in the complete list of hazards before pre-processing.

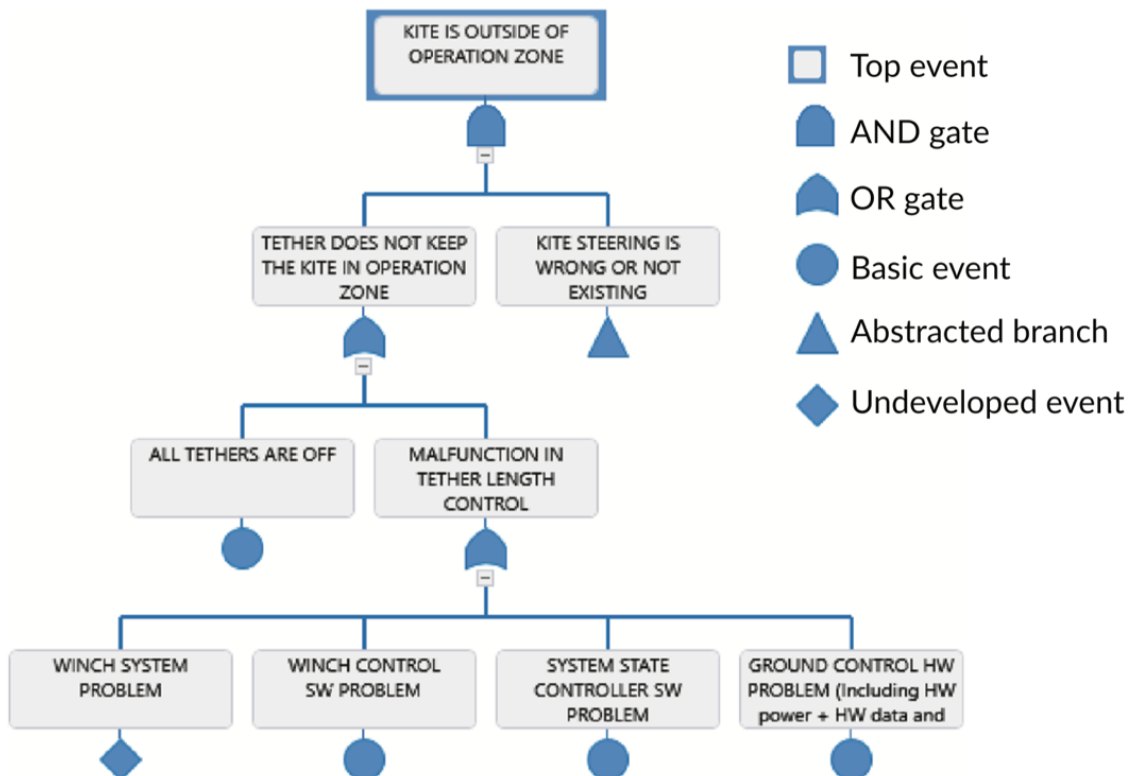


Figure 6.1: Basic events of top fault tree made by Salma et al. (2019).

Table 6.1: Overview of hazards that might result in a kite outside the operational zone.

	Originator	Description
A	Christian	Tether failure
B	Christian	Safety line failure
C	Christian	Helicopter crash into the kite
D	Bert	Airplane crash into the kite
E	Alexandre	Birds crash into the kite
F	Joep	Sabotage
G	Alexandre	Goats on the tether
H	Christian	Kite crashing into house
I	Joep	Tether not attached to the ground station
J	Joep	Ground Station slides away
K	Alexandre	Safety release does not work when needed
L	Alexandre	Lightning hitting the system
M	FTA	Kite steering is wrong or non-existing
N	FTA	All tethers are off
O	FTA	Winch system problem
P	FTA	Winch control SW problem
Q	FTA	System state controller SW problem
R	FTA	Ground control HW problem

6.2 Potential Hazard Pre-processing

In this section the hazard list made in section 6.1, depicted in Table 6.1, is pre-processed. Duplicate and irrelevant hazards are removed and some hazards are generalised. Firstly, duplicate hazards are removed. Hazard N, “All tethers are off”, is similar as hazard A, “Tether failure”. Therefore, hazard M is removed. Also hazard G, “Goats on the tether”, and hazard L, “Lightning hitting the system”, are merged to one hazard because of its similarity. This merge is named “Damaged tether by external factor”. Next, the irrelevant hazards are removed. Only one irrelevant hazard is found, hazard F. Hazard F, “sabotage”, is removed because it is not a safety issue. Sabotage is a security issue because with sabotage people have a malicious intent. Lastly, some hazards are generalised. In Table 6.1 only hazard H needs to be generalised a bit more. It is a very specific description. Therefore, hazard H is generalised to “Third-party harm due to kite crash”. This results in the following list of hazards:

- 1. Tether failure:** This hazard represents a broken tether. The tether can break at the top or at the bottom of the tether.
- 2. Safety line failure:** This hazard represents a safety line failure, if the safety line fails there is no back-up if a safety release mechanism or weak link is initiated.
- 3. Helicopter crash into the kite:** This hazard represents a helicopter crash into the kite. The helicopter can separate the kite from the ground station at various locations.
- 4. Airplane crash into the kite:** This hazard represents an airplane crash into the kite. The airplane can separate the kite from the ground station at various location. However, it can also move the complete system.
- 5. Birds crash into the kite:** This hazard represents a bird crash into the kite. The bird can damage the kite with the result that it is separated from the KCU, tether, and ground station.
- 6. Damaged tether by external factor:** This hazard represents the possibility that external factors damage or even break the tether. This separates the tether, KCU, and kite from the ground station.

7. **Third-party harm due to kite crash:** This hazard is the renamed hazard “Kite crashing into house”. This hazard is generalised to a collision with a third-party.
8. **Tether not attached to ground station:** This hazard represents that it can be forgotten to attach the tether to the ground station. If the drum of the ground station rolls too far off the kite, KCU, and tether are separated from the ground station.
9. **Ground station slides away:** This hazard represents a sliding ground station due to too high forces.
10. **Safety release does not work when needed:** This hazard represents a defect safety release and weak link. This could lead to too high loads on the tether and even a tether failure if other systems are not able to reduce this load.
11. **Kite steering is wrong or non-existing:** This hazard represents an uncontrollable kite. This could lead to too high loads on the tether and even a tether failure if other systems are not able to reduce this load.
12. **Winch system problem:** This hazard represents a not working ground station winch. This could lead to too high loads on the tether and even a tether failure if other systems are not able to reduce this load.
13. **Winch control software problem:** This hazard represents a not working ground station winch due to a software issue. This could lead to too high loads on the tether and even a tether failure if other systems are not able to reduce this load.
14. **System state controller software problem:** This hazard represents a not working system state controller. This leads to unidentified dangerous situations. Therefore, the system is not in control of the system. This could lead to too high loads on the tether and even a tether failure if subsystems do not notice the situation.
15. **Ground control hardware problem:** This hazard represents a hardware problem for the ground control. This could lead to several dangerous situations, also a tether failure.

6.3 Scenario Identification

In this section potential safety-relevant scenarios are identified based on the potential hazard list of section 6.2. There are four safety-relevant scenarios identified based on the hazard list of section 6.3. These scenarios are as follows:

- I. **Tether, KCU, and kite fly away:** In this scenario the tether, KCU, and kite are not attached to the ground station anymore. The ground station is still at its original position. The tether, KCU, and kite fly away with the wind. The tether is broken close to the ground station in this situation.
- II. **KCU and kite fly away:** In this scenario the KCU and kite are not attached to the ground station anymore. The ground station is still at its original position. The KCU and kite fly away with the wind. The tether is broken close to the KCU or/and the safety line has failed in this situation.
- III. **Kite flies away:** In this scenario only the kite flies away and is not attached to the KCU, tether, or ground station. The ground station is still at its original position.
- IV. **The system slides away:** In this scenario the complete system is not at its original position anymore and the ground station slides over the ground.

6.4 Crystallization

In this section the crystallization is performed of the previously mentioned potential hazards and safety-relevant scenarios. With crystallization each potential safety-relevant scenario is used as crystallization point upon which all applicable hazards are fitted. In section 6.2 the hazards are identified. In section 6.3 the safety-relevant scenarios are identified. These numbering of these sections are used in the crystallization. The crystallizations are depicted in Figure 6.3 and Figure 6.4, in Figure 6.2 the legend is found.

Firstly, hazard one, two, four, six, or eight can immediately lead to scenario I, without the accumulation of another hazard, as depicted in Figure 6.3. A combination of hazard fifteen, fourteen, thirteen, or twelve with hazard ten and eleven can also lead to scenario I, the scenario where the tether, KCU, and kite fly away. For example, hazard eleven, “kite steering is wrong or non-existing”, can only lead to a close to the ground tether failure if the redundant safety release and weak link do not work (hazard ten) and the ground station is not able to adapt to the high forces. This happens with hazard fifteen, fourteen, thirteen, or twelve. Scenario I can lead to hazard seven, “third-party harm due to kite crash”, if the kite, KCU, and tether crash on a third-party.

The crystallization of scenario II is very similar as scenario I, as depicted in Figure 6.3. Hazard one, three, or four can immediately lead to scenario II, without the accumulation of another hazard. Situation II can also occur if hazard eleven happens in combination with hazard ten or two and in combination with hazard fifteen, fourteen, thirteen, or twelve. Scenario II can also lead to hazard seven, “third-party harm due to kite crash”, if the kite, KCU, and tether crash on a third-party.

The crystallization of scenario III is rather simple. Hazard three, four, and five can immediately lead to situation where the kite flies away, as depicted in Figure 6.4. The kite crash on third-parties in this situation and therefore scenario III can also lead to hazard seven “third-party harm due to kite crash”.

Lastly, hazard nine and four can immediately lead to scenario IV, without the accumulation of another hazard, as depicted in Figure 6.4. Furthermore, hazard eleven in combination with hazard fifteen, fourteen, thirteen, or twelve can lead to scenario IV. Scenario IV can eventually also lead to hazard seven.

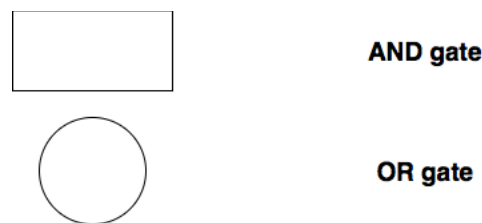


Figure 6.2: Legend of the crystallizations in Figure 6.3 and Figure 6.4.

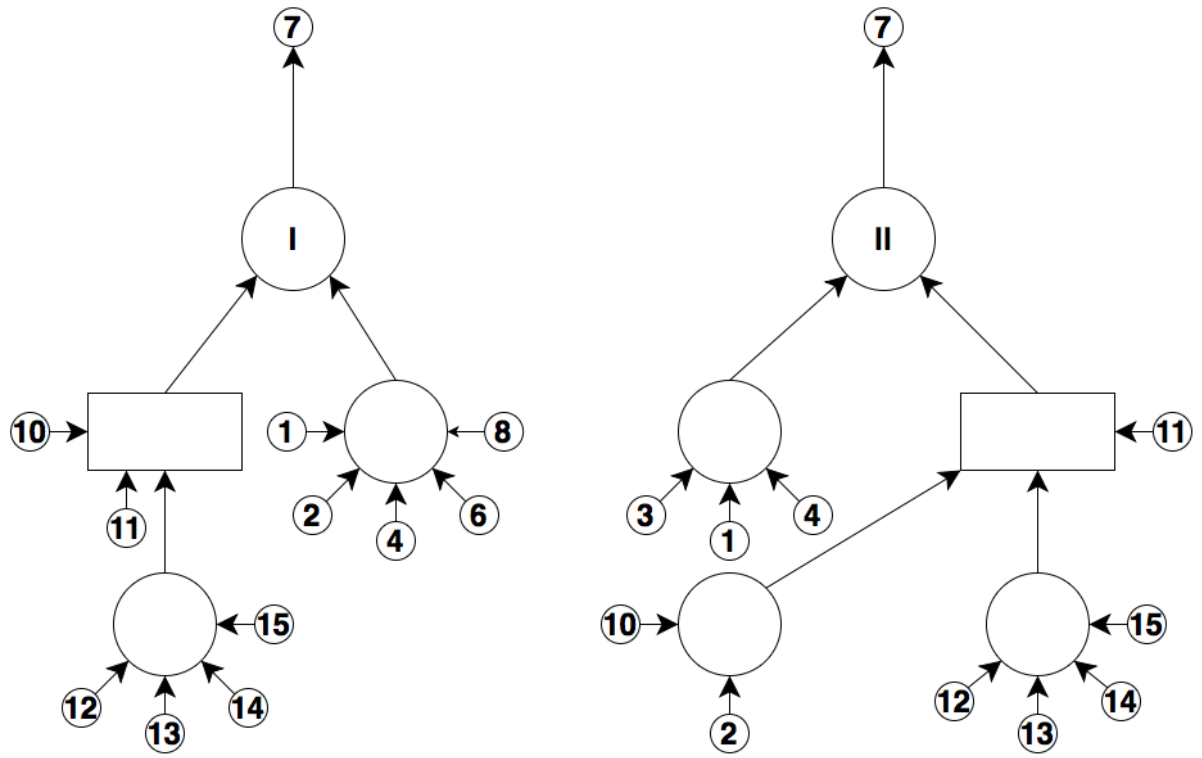


Figure 6.3: Overview of the crystallizations of situation I and II.

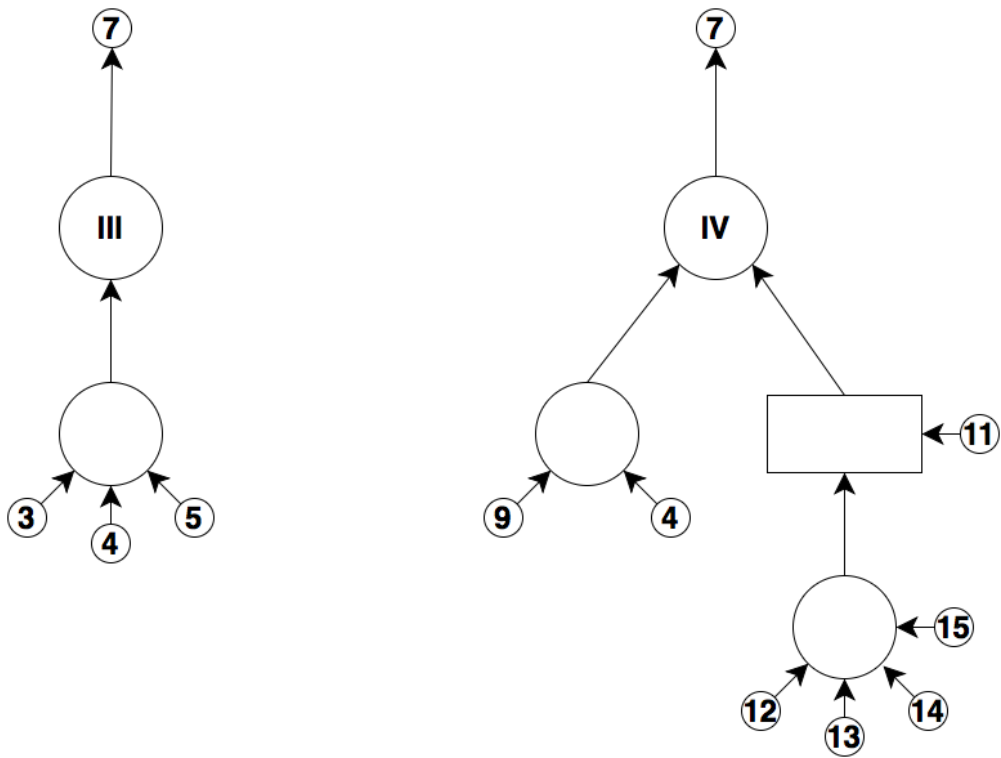


Figure 6.4: Overview of the crystallizations of situation III and IV.

6.5 Consequences

In this section the consequences of the four identified safety-relevant scenarios are described. It is discussed if the system leaves the operational zone. Furthermore, the consequences of leaving the operational zone are discussed.

Scenario I

Scenario I is the safety-relevant scenario in which the tether, KCU, and kite fly away. In this scenario various consequences are possible. Firstly, the tether, KCU, and kite can crash within the operational zone. This happens if the kite flies at a low altitude or if the kite flutters/whirls. In this situation the system does not harm any third-parties since no parties are present in the operational area.

Secondly, the tether, KCU, and kite can fly away outside the operational zone if the kite flies at a high altitude and with higher wind velocities at the moment of the hazard. In this situation the kite flies with the wind and is controlled by the KCU. The KCU balances the kite. The consequence can be a crash of the tether, KCU, and/or kite on third-parties. The KCU and kite can crash on third-parties which might result in a fatality.

Lastly, the end of the tether can snag behind something after a (short) flight. In this situation the kite and KCU can come down with a high velocity outside the operational zone. This nosedive can lead to dangerous situations due to the high impact velocity of the KCU and kite.

Scenario II

Scenario II is the safety-relevant scenario in which the KCU and kite fly away. The consequences of this scenario are fairly similar as scenario I. Only the last consequence of scenario II, the nosedive, is not possible in this scenario. Therefore, the first consequences of scenario II is that the KCU and kite crash on the ground within the operational zone. This happens if the kite flies at a low altitude or if the kite flutters/whirls. In this situation the system does not harm any third-parties since no parties are present in the operational area.

The second possible consequence is the situation in which the kite and KCU fly away outside the operational zone. This happens if the kite flies at a high altitude and with higher wind velocities at the moment of the hazard. In this situation the kite flies with the wind and is controlled by the KCU. The KCU balances the kite. The possible consequence is the harm of third-parties by a crash of the KCU and/or kite. This can lead to a fatality.

Scenario III

Scenario III is the safety-relevant scenario in which the kite flies away. In this scenario the kite flies away with the wind. However, the KCU is not attached to the tether. Therefore, the kite will flutter and whirl like a piece of paper. The crash location depends on the location of the kite at the moment of the hazard and the wind. The kite can flutter outside the operational zone but also can stay inside the operational zone. Of course, outside the operational zone the kite can crash on third-parties. However, the impact velocity will not be very high. Therefore, the chance on a fatality is very low.

Scenario IV

Scenario IV is the safety-relevant scenario in which the complete system slides over the ground. There are two types of consequences of this scenario. Firstly, the situation in which the tether is not completely reeled out and the ground station slides over the ground. In this situation there are no consequences for third-parties because the system stays within the operational zone.

The second situation is the situation in which the tether is reeled out and the ground station slides over the ground. In this worst case scenario, the kite can leave the operational zone and crash on the ground. In this situation there are high forces on the kite since it moves the ground station. Therefore, the chance of a high impact velocity increases and therefore the chance of a fatality increases as well. However, only the kite and KCU will leave the operational zone. The situation in which the ground station slides outside the operational zone is unfeasible because the movement will never be more than a few meters in the worst case scenario.

6.6 Comparison FMEA and FTA

In this section the comparison is made between the performed hazard brainstorm and the performed analyses by Salma et al. (2019), an FMEA and FTA. Firstly, the comparison is made between the FMEA and the performed hazard brainstorm. Secondly, the comparison is made between the FTA and the performed hazard brainstorm.

FMEA Comparison

For the FMEA 80 failure modes of electronic hardware and software components were investigated. During the hazard brainstorm these failure modes were not considered. Furthermore, the identified hazards in the hazard brainstorm were not considered in the FMEA. Therefore, the hazard identified during the performed hazard brainstorm are complementary to the FMEA performed by Salma et al. (2019). The four identified safety-relevant scenarios in section 6.3 and its consequences of section 6.5 were not considered in the FMEA.

FTA Comparison

The FTA has three main differences with the performed hazard brainstorm. Firstly, the FTA only has one safety-relevant scenario. While, the hazard brainstorm resulted in four different safety-relevant scenarios. Furthermore, the scenarios that resulted from the hazard brainstorm are also more specific.

Secondly, in the performed hazard brainstorm new hazards were identified that were not identified in the FTA. The hazards identified in the FTA were also used in the analysis of the hazard brainstorm.

Lastly, there is a difference in definition of the operational zone between the FTA and the hazard brainstorm. In the FTA the operational zone is a small airspace. The definition of the operational zone during the hazard brainstorm is the complete circle around the ground station.

7 Model Description

In chapter 6 four safety-relevant scenarios are generated. The next step in the safety risk assessment is the development of a safety risk model. This chapter develops the third-party risk model of scenario I of chapter 6. The tether snag that results in a nosedive situation is not included in the model.

The third-party risk model framework of the UAS operations from Blom et al. (2020) is used as a basis for the third-party risk model. Furthermore, the differential equations from the non-nominal descend model are established by the information from the airborne wind energy book from Ahrens (2013) and the thesis on third-party risk from Vettorato (2021).

Firstly, in section 7.1 every step of the third-party risk model framework of the UAS parcel delivery operation from Blom et al. (2020) is evaluated. The third-party risk model for the Kitepower operations is explained for every step. Secondly, the flight path model is explained. In section 7.2 there is elaborated on the flight path model from Johnson (2019). This flight path model is used in this thesis. In section 7.3 there is elaborated on the event rate of the tether failure. The tether failure leads to scenario I. Next, in section 7.4 the non-nominal descend model is explained. In this section there is elaborated on the differential equations. Furthermore, the accelerations are modelled by the force calculations. Lastly, in section 7.5 the fatality model is explained. This model is the Range Commanders Council (2001) adopted Feinstein model and also used by Blom et al. (2020) in the third-party risk assessment of the UAS parcel delivery operation.

7.1 Evaluation Steps

In this section the third-party risk model framework for UAS delivery developed by from Blom et al. (2020) is evaluated. This model framework considers N flights per annum over an area Y . The objective of this model is to estimate the Individual risk $R_I^{UAS}(y)$ for each position $y \in Y$. A Monte Carlo simulation is conducted for the generation of N nominal flight paths, and subsequently to conduct a Monte Carlo simulation of K flights in which the failure event occurs that leads to a ground crash for each of these N nominal flight paths.

For Kitepower the area Y is considered to be the area around the ground station. The ground station is located near the town Rutten, the Netherlands, for this third-party risk model. The ground station is located at $52^\circ 48' 45.30'' \text{N}$ $005^\circ 42' 39.30'' \text{E}$ in the simulation. In Figure 7.1 the location of the ground station is depicted with respect to its surroundings. Furthermore, the depicted circle has a radius of 400m. This circle represents the operational zone of 400m. In the third-party risk model of the Kitepower operations N is the number of cycles per annum. One flight cycle consists of the four phases: reel-out phase, first transition phase, reel-in phase, and second transition phase. K is also considered to be flight cycles. Therefore, a Monte Carlo simulation is developed of K flight cycles in which a failure event occurs that leads to a ground crash for each of these N nominal flight paths of the flight cycles.

In this section every step of the risk model is explained. In *italics* the description of the step is given. Below the step a more detailed explanation is given. Step 0 is not discussed because this step is not relevant for the Kitepower operations.



Figure 7.1: Overview of the surroundings of the proposed test location in Rutten, the Netherlands.

Step 1: Determine nominal flight paths for each of the N flight cycles.

In step 1 the nominal flight paths are determined. For the 4-dimensional nominal flight path the model of Johnson (2019) is adopted. This is described in detail in section 7.2. An example flight path from the flight path model of Johnson (2019) is depicted in Figure 7.2 for a wind velocity of 7 m/s. Firstly, N nominal wind conditions $v_{wind}^{i,nom}$ are obtained from historical data from KNMI by introducing a wind condition grid to keep N finite. For each of these N nominal wind conditions, the Johnson model yields the duration T_i^{nom} of i -th nominal flight path, the 3D position $s_t^{i,nom}$ and velocity $v_t^{i,nom}$ of the kite at every $t \in [0, T_i^{nom}]$, as well as the attitude $\theta_t^{i,nom}$.

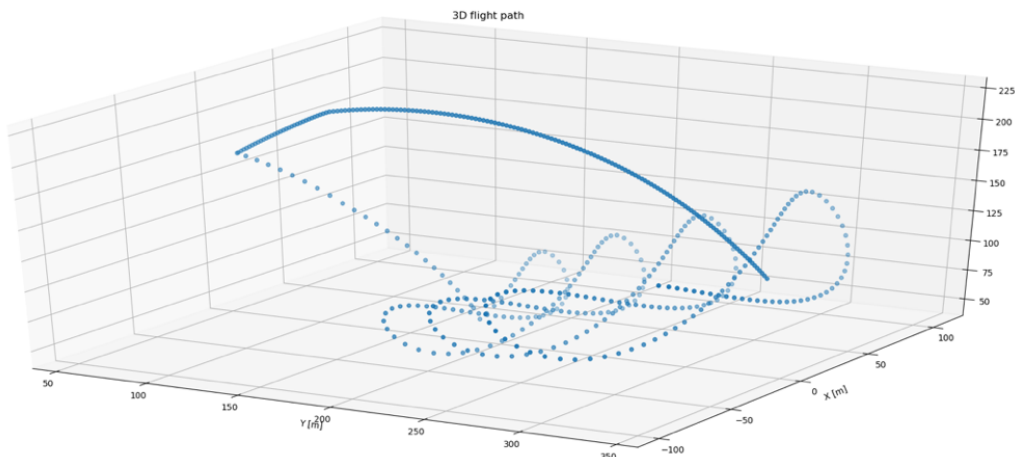


Figure 7.2: Nominal flight path of the kite at a wind velocity of 7 m/s.

Step 2: Evaluate ground crash probability. Calculate for each of the N flight cycles and each event $e \in E$ the probability of a crash.

In this step the ground crash probability is modelled. The ground crash probability $P(e|i)$ is modelled for each of the N flight cycles and each event $e \in E$ in Equation 7.1.

$$P(e|i) = 1 - \exp\left\{-\left(\int_0^{T_i^{nom}} \lambda_{i,e}(t) dt\right)\right\} \quad (7.1)$$

Where $\lambda_{i,e}(t)$ is the rate of event e to happen at moment t during the i -th flight cycle. In this model there is only one event, the tether failure. $\lambda_{i,e}(t)$ is not always constant. The tether failure event occurs more often in the reel-out phase. Therefore, $\lambda_{i,e}(t)$ is higher during this phase. The rate of event $\lambda_{i,e}(t)$ is described in detail in section 7.3.

Step 3: Simulate kite cycles that crash.

In this step ground crashes are simulated. A Monte Carlo simulation consisting of K_i runs that crash to the ground is conducted for each of the N flight cycles and each event $e \in E$, i.e. for $k = 1, \dots, K_i$. K_i is defined as the absolute value of the nominal duration of one cycle:

$$K_i = \lfloor T_i^{nom} \rfloor \quad (7.2)$$

The nominal duration depends on the flight cycle N . The Monte Carlo simulation consists of three substeps.

Substep 3.1: Generate a random moment of event time.

In this substep a random event time $t_e^{i,k}$ is generated for every crash simulation. This is the starting moment of the non-nominal kite descend that ends into a ground crash

Substep 3.2: Simulate for the i, k -th flight, for each event $e \in E$ the kite state at moment of failure event $t_e^{i,k}$.

In this step the state components are generated at moment of failure event $t_e^{i,k}$. These state components are obtained from the flight path model. These states are updated in substep 3.3 by obtaining the acceleration. The state components at failure time t_e , that are generated, are 3D position $s_{t_e}^{i,k}$, 3D velocity $v_{t_e}^{i,k}$, 3D wind velocity $v_{wind,t_e}^{i,k}$, and attitude $\theta_{t_e}^{i,k}$, as depicted in Equation 7.3.

$$\begin{aligned} s_{t_e}^{i,k} &= s_{t_e}^{i,nom} + \varepsilon_{t_e}^S \\ v_{t_e}^{i,k} &= v_{t_e}^{i,nom} \\ v_{wind,t_e}^{i,k} &= v_{wind}^{i,nom} + \varepsilon_{t_e}^{v_{wind}} + \varepsilon_{grid}^{v_{wind}} \\ \theta_{t_e}^{i,k} &= \theta_{t_e}^{i,nom} \end{aligned} \quad (7.3)$$

Where $s_{t_e}^{i,nom}$ is the position of the kite at failure time t_e with nominal flight path i . $\varepsilon_{t_e}^S$ is the deviation from the nominal flight path at failure time t_e . The deviation from the nominal flight path is defined

by Equation 7.4. Where σ_x , σ_y , and σ_z is the standard deviation of the normal distribution in the x , y , and z direction, respectively. $v_{t_e}^{i, nom}$ is the velocity of the kite at failure time t_e with the nominal flight path i . $v_{wind}^{i, nom}$ is the wind velocity vector of the nominal flight path i . $\varepsilon_{t_e}^{v_{wind}}$ is the randomly generated wind gust at failure time t_e . In section 7.4 there is elaborated on these randomly generated wind gusts. $\varepsilon_{grid}^{v_{wind}}$ is the wind sampling error. This error has an almost uniform distribution¹. Lastly, $\theta_{t_e}^{i, nom}$ is the attitude of the kite at failure time t_e according to the nominal flight path i .

$$\varepsilon_{t_e}^S \sim \begin{bmatrix} N(0, \sigma_x) \\ N(0, \sigma_y) \\ N(0, \sigma_z) \end{bmatrix} \quad (7.4)$$

Substep 3.3: Simulate non-nominal descend.

In this step the non-nominal descend to the ground is simulated. The non-nominal descend occurs between the time interval $[t_e^{i,k}, t_{c,e}^{i,k}]$, i.e. from the start of the event $t_e^{i,k}$ until the moment of the ground crash $t_{c,e}^{i,k}$. This yields the state $x_{c,e}^{i,k}$ of the kite. During the non-nominal descend the kite evolves according to the following differential equations:

$$\begin{aligned} \dot{s}_t &= \dot{v}_t \\ \dot{v}_t &= a_t \\ a_t &= \frac{L(\alpha) + D(\alpha) + W + F_T}{m_{kite} + m_{KCU} + m_{Tether}(l)} \end{aligned} \quad (7.5)$$

Where $L(\alpha)$ is the lift force of the kite. The lift force depends on the angle of attack α . $D(\alpha)$ is the drag force of the kite and also depends on the angle of attack α . W is the gravitational force of the airborne parts of the system. F_T is the tether force. m_{kite} is the mass of the kite, m_{KCU} is the mass of the KCU, and $m_{Tether}(l)$ is the mass of the airborne part of the tether. Therefore, the mass of the tether depends on the length of the tether l . A detailed explanation of these differential equations is given in section 7.4.

Step 4: Evaluate the crash location model.

In this step the results from the Monte Carlo simulation are used to model the estimate of the local hit density and the estimate of the probability that the simulated crash locations are in a certain grid cell. The area around the ground station is divided in square grid cells G_j of size $|G_j|$. The estimated probability $\hat{P}(j|i, e)$ that the simulated crash locations $s_{c,e}^{i,k}$ is in grid cell G_j is obtained by Equation 7.6.

$$\hat{P}(j|i, e) = \frac{\sum_{k=1}^{K_i} [1[s_{c,e}^{i,k} \in G_j]]}{K_i} \quad (7.6)$$

¹ In this thesis the wind sampling error is assumed 0.0m/s. This assumption is explained in section 9.1.

Where 1 is a binary function, i.e. $1[true]=1$ and $1[false]=0$. The estimate of the local hit density $\hat{p}_s(y_i|li, e)$ for an arbitrary location y_j in grid cell G_j in area Y is obtained by Equation 7.7.

$$\hat{p}_s(y_i|li, e) = \frac{\hat{P}(j|li, e)}{|G_j|} \quad (7.7)$$

Where $|G_j|$ is the area size of the j -th grid cell.

Step 5: Estimate the probability of fatality for hitting an unprotected person in each grid cell.

In this step the unprotected fatality probability $\hat{P}(F|j, i, e)$ is modelled, for each j, i, e for which $\hat{P}(j|li, e) > 0$. The equations used are:

$$\hat{P}(F|j, i, e) = \frac{\hat{P}(F, j|li, e)}{\hat{P}(j|li, e)} \quad (7.8)$$

With nominator:

$$\hat{P}(F, j|li, e) = \frac{\sum_{k=1}^{K_i} [1[s_{c,e}^{i,k} \in G_j] P(F|v_{c,e}^{i,k}, s_{c,e}^{i,k} \in A(i, e))]}{K_i} \quad (7.9)$$

The crash fatality model $P(F|v_{c,e}^{i,k}, s_{c,e}^{i,k} \in A(i, e))$ is explained in section 7.5.

Assumption 7.1: The crash of the kite consists of two objects: the kite and the KCU.

Step 6: Evaluate the individual risk per flight cycle.

In this step the individual risk per cycle $R_I^i(y)$ is estimated. Equation 7.10 is used to obtain the estimate of the individual risk per cycle $\hat{R}_I^i(y)$ for an arbitrary location y_i in grid cell G_j , for each i -th flight cycle.

$$\hat{R}_I^i(y) = \sum_{e \in E} \left[P(e|li) \hat{p}_s(y_j|li, e) |A(i, e)| \hat{P}(F|j, i, e) \right] \quad (7.10)$$

Where $|A(i, e)|$ is the size of the crash impact area of flight cycle i with event type e . Due to assumption 7.1 there are two crash impact areas, one from the KCU $|A(i, e)_{KCU}|$ and one from the kite $|A(i, e)_{kite}|$.

Step 7: Evaluate the individual risk per year.

In this step the estimated individual risk per year $\hat{R}_I^i(y_j)$ for an arbitrary location y_i in grid cell G_j is obtained by Equation 7.11.

$$\hat{R}_I^i(y_j) = 1 - \prod_{i=1}^N \left[1 - \hat{R}_I^i(y) \right] \quad (7.11)$$

Step 8: Compare the individual risk with regulations.

In this step the individual risk is compared with the applicable threshold values of acceptable level of individual risk for hazardous installations. The threshold in the UK and the Netherlands is 10^{-6} per annum for individual risk that is posed to new objects, as discussed in section 4.3.

Step 9: Assess the population map for each grid cell.

In the introduction of this section the operation location is explained in detail. In this step the estimated population density $\hat{\rho}_j$ for every grid cell is obtained by:

$$\hat{\rho}_j = \rho(y_j) |G_j| \quad (7.12)$$

Where $\rho(y_j)$ is the population density at location y_j . The population density map was obtained from the CBS (2020).

Step 10: Assess the probability of shelter protection against a ground crash.

In this step the probability of shelter protection $\hat{p}(Sl, H)$ against a ground crash for each grid cell G_j of the i -th flight cycle of the kite is established.

Assumption 7.2: In every grid cell the probability of shelter protection is the same.

Step 11: Estimate collective ground risk per flight cycle.

In this step the estimated collective ground risk per flight cycle $\hat{R}_{Cground}^i$ in area Y is modelled. The estimated collective ground risk per flight cycle $\hat{R}_{Cground}^i$ is obtained by Equation 7.13.

$$\hat{R}_{Cground}^i = \sum_j [\hat{R}_j^i(y) [1 - \hat{P}(Sl, j, i)]] \hat{\rho}_j \quad (7.13)$$

Step 12: Estimate collective ground risk per flight hour.

In this step the estimated collective ground risk per flight hour is modelled for each flight cycle. This is obtained by Equation 7.14.

$$\frac{\hat{R}_{Cground}^i}{T_i^{nom}} \quad (7.14)$$

The nominal flight time T_i^{nom} is different for every wind velocity. The result of this step is a histogram of simulation results for the N flight cycles.

Step 13: Compare the collective ground risk per flight hour with the regulations.

In this step it is verified if the empirical density obtained in step 12 passes an applicable threshold level. There is looked at the regulations of UAS. For example, Jarus (2017) sets a threshold of 10^{-6} fatal injuries on the ground per flight hour. It should be observed if the operations of Kitepower meet this requirement.

Step 14: Estimate collective ground risk.

In this step the estimated collective ground risk per year $\widehat{R}_{Cground}^{Kite}$ is modelled by Equation 7.15.

$$\widehat{R}_{Cground}^{Kite} = \sum_{i=1}^N \widehat{R}_{Cground}^i \quad (7.15)$$

In Equation 7.15 the collective ground risk of all N flight cycles are accumulated.

Step 15: Compare the collective ground risk with the regulations.

In this step the estimated collective ground risk is compared with the applicable threshold level of collective ground risk. These thresholds are based on requirements posed on FN-curves which are found in chapter 4. Most regulations are on FN-curves and can be converted to regulations on collective ground risk as described in Equation 3.15. In this thesis $\alpha=2$. The collective ground risk is limited by Equation 7.16 with $C=10^{-3}$ [Blom et al., 2020].

$$R_{Cground}^{Kite} < C \frac{\pi^2}{6} \quad (7.16)$$

The collective ground risk is not modelled for the current number of flight hours due to the low number. It is assessed for the commercial operations.

7.2 Flight Path Model

In this section the flight path model used in step 1 is explained. Several flight paths models are already developed for the simulation of the flight path of the kite. Faggianni (2014) developed a 2D flight path model. This 2D model assumes that the azimuth of the kite is constant during the complete cycle. The figure eight manoeuvres are neglected in this 2D model. In Figure 7.3 the 2D flight path model from Faggianni (2015) is depicted. Johnson (2019) extended the flight path model developed by Faggianni (2015). The extension is mainly the addition of the figure eight manoeuvres. This extension turns the simulation from a 2D model into a 3D model. In Figure 7.4 the flight path of the model developed by Johnson (2019), the 3D model, is depicted. This figure eight movement is significant for the risk assessment, as the exact kite location and (tangential) velocities have a large impact on the final crash location. Not accounting for the (tangential) velocities can result in an inaccurate risk assessment. In this section the 3D flight path model is briefly explained. The details of the 3D flight path model are explained in the thesis report of Johnson (2019).

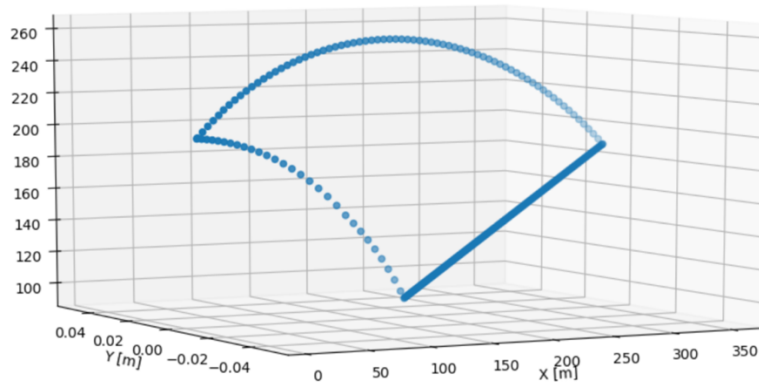


Figure 7.3: 2D flight path model [Faggianni, 2015].

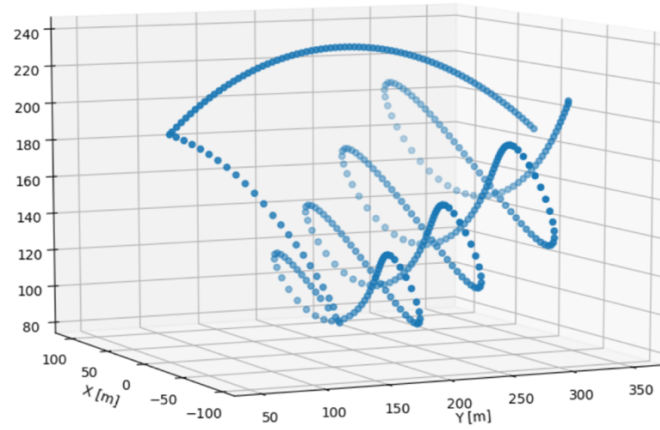


Figure 7.4: 3D flight path model [Johnson, 2019]

Introduction of the quasi-steady model

The 3D model is a quasi-steady model, this means that it is assumed that at each time step there is a force equilibrium at the kite. A single point mass is used to represent all airborne mass. The mass of all airborne components are taken into consideration. The force equilibrium depends on the phase. In the transition phases and the reel-in phase the force equilibrium is 2D. In the reel-out phase the force equilibrium is 3D. The velocity is obtained from the force equilibria at every time step. Therefore, it is important to specify the flight phase of the kite at every moment in time. The 3D model starts the cycle just after the reel-out phase, at this point the time t is zero. The 3D model starts with the first transition phase, after the first transition phase the reel-in phase starts. This phase starts if a certain elevation is reached. The next phase is the second transition phase. This phase starts if the minimum radial distance is reached. The last phase in the 3D model is the reel-out phase. The reel-out phase starts if a certain azimuth is reached. The simulation ends if the maximum radial distance is reached. Therefore, the input parameters for the 3D model are:

- The reel-in force F_{in} : The force on the tether during the reel-in phase. This value is calibrated for different wind velocities.
- The reel-out force F_{out} : The force on the tether during the reel-out phase. This value is calibrated for different wind velocities.
- The minimum radial distance of the kite r_{min} : The second transition phase is started when the minimum radial distance r_{min} is reached during the reel-in phase.
- The maximum radial distance of the kite r_{max} : The flight cycle ends if the maximum radial distance of the kite r_{max} is reached during the reel-out phase.
- The magnitude of the wind velocity at the ground $\left| v_{wind,ref}^{i,nom} \right|$: The wind velocity has a high impact on the location and velocity of the kite. In the 3D model the wind velocity at the kite is not assumed to be constant. The wind velocity increases with an increasing height above the ground z . This due to the roughness of the terrain z_0 . The classification of the surface roughness is depicted in Table 7.1. In the 3D model the wind velocity is assumed to follow a logarithmic profile. The input wind velocity $\left| v_{wind,ref}^{i,nom} \right|$ is wind data from the KNMI station Marknesse. The height above the ground of this wind sensor is h_{ref} . The wind velocity at the kite $\left| v_{wind}^{i,nom}(z) \right|$ is obtained by Equation 7.17 [Johnson, 2019].

$$\left| v_{wind}^{i,nom}(z) \right| = \left| v_{wind_{ref}}^{i,nom} \right| \frac{\ln \frac{z}{z_0}}{\ln \frac{h_{ref}}{z_0}} \quad (7.17)$$

In the model of Johnson (2019) the magnitude of the wind is obtained by Equation 7.18.

$$v_w = \left| v_{wind}^{i,nom}(z) \right| \quad (7.18)$$

Table 7.1: Classification of roughness [Stull, 2000]

Roughness	Terrain	Characteristics
0.0002	Sea	Sea, paved area, snow-covered flat plain, tide flat, smooth desert.
0.005	Smooth	Beaches, pack ice, morass, snow-covered fields grass prairie or farm.
0.03	Open	Grass prairie or farm fields, tundra, airports, heather.
0.1	Roughly open	Cultivated area with low crops and occasional obstacles (single bushes).
0.25	Rough	High crops, crops of varied height, scattered obstacles such as trees.
0.5	Very rough	Mixed farm fields and forests clumps, orchards, scattered buildings.
1	Closed	Regular coverage with large size obstacles with open spaces roughly equal to obstacle heights, suburban houses, villages, mature forests.
≥2	Chaotic	Centres of large towns and cities, irregular forests with scattered clearings.

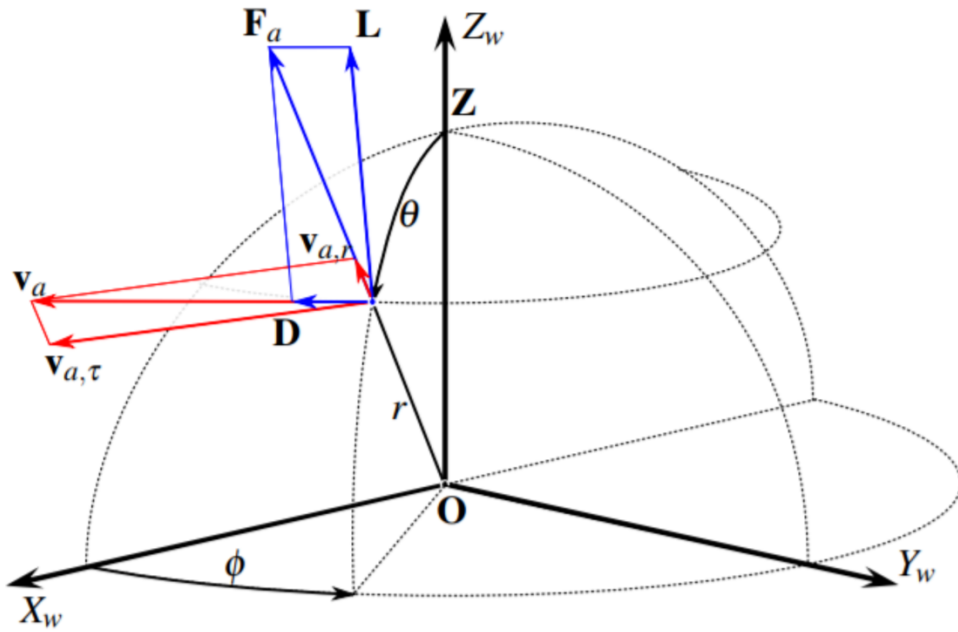


Figure 7.5: Reference coordinate system of Johnson (2019).

Nominal Wind Fixed Reference Frame

First the reference frame needs to be explained before explaining the force equilibrium for all the time steps. The reference coordinate system, used by Johnson (2019), is depicted in Figure 7.5. The reference frame represents the kite path in both spherical and cartesian coordinates. The kite position is defined by the radial vector R , which is defined by the polar coordinates (r, θ, ϕ) . Where r is the radial distance between the kite and the ground station, θ is the polar angle, and ϕ is the azimuth angle. Furthermore, it is important to note that the wind velocity is in the direction of the positive x -axis with the origin at the ground station. Therefore, this is not an earth fixed reference frame but a wind fixed reference frame. The reference frame moves in the direction of the wind. Therefore, all the position vectors are converted from the wind fixed reference frame to the earth fixed reference frame at the end of the flight path model. This is performed by turning the reference frame by the wind direction around the z -axis. Next, in Figure 7.5 it is depicted that the aerodynamic force F_a is the result of the addition of the lift and drag force vectors. The drag vector is in the same direction as the apparent wind speed vector v_a , both vectors consist of a radial and tangential component. Lastly, the kite velocity v_k is defined by the radial velocity $v_{k,r}$ and tangential velocity $v_{k,t}$ in the 3D model.

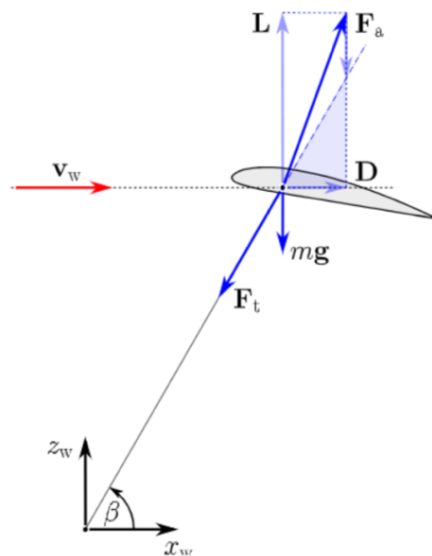


Figure 7.6: 2D reference coordinate system of Faggiani (2014).

Velocity Calculations

The kite velocity is updated after every time interval Δt . The calculations are performed by using the equilibrium force calculations. In Figure 7.6 the forces on the kite are depicted in 2D. In Figure 7.6 the elevation angle β is depicted, the elevation angle is the complementary angle of the polar angle. In the transition phases and the reel-in phase only the 2D forces are relevant, as depicted in Figure 7.6. The 3D forces are important for the reel-out phase, as depicted in Figure 7.5.

The velocity of the kite is modelled via the force equilibrium. Some ratios are introduced by Johnson (2019) that are important for the velocity calculation. Firstly, the tangential velocity factor λ is the relation between the tangential kite velocity $v_{k,\tau}$ and the wind velocity v_w and is defined in Equation 7.19.

$$\lambda = \frac{v_{k,\tau}}{v_w} \quad (7.19)$$

The kinematic ratio k is defined as the ratio between the tangential apparent velocity $v_{a,\tau}$ and the radial apparent velocity $v_{a,r}$. The kinematic ratio is mathematically defined in Equation 7.20.

$$\kappa = \frac{v_{a,\tau}}{v_{a,r}} \quad (7.20)$$

The last important ratio is the reeling factor f . The reeling factor is defined as the ratio between the radial kite velocity $v_{k,r}$ and the wind velocity v_w . The reeling factor is mathematically defined in Equation 7.21.

$$f = \frac{v_{k,r}}{v_w} \quad (7.21)$$

Firstly, the radial kite velocity is found by obtaining the reeling factor. The reeling factor is mostly zero in the transition phases. It is assumed that the aerodynamic force is equal to the tether force in the reel-out and reel-in phase, neglecting the gravity effects in the radial direction. The aerodynamic force is modelled by:

$$F_a = C_R P_w S (1 + \kappa^2) (\sin(\theta) \cos(\phi) - f^2) \quad (7.22)$$

Where C_R is the resultant coefficient. The resultant coefficient is obtained from the kite lift and drag coefficients. P_w is the dynamic air pressure and S is the projected surface area of the kite. The reeling factor is obtained by equalizing the aerodynamic force F_a with the tether force F_T . In the reel-out phase the tether force is equal to F_{out} . During the reel-in phase the tether force is equal to F_{in} . Therefore, the reeling factor is obtained by:

$$f = \cos(\beta) \cos(\phi) - \sqrt{\frac{F_T}{P_w S C_R \left(1 + \left(\frac{L}{D}\right)^2\right)}} \quad (7.23)$$

The reeling velocity is obtained from the reeling factor by Equation 7.20. The tangential velocity factor is obtained by Equation 7.24.

$$\lambda = a + \sqrt{a^2 + b^2 - 1 + k^2 (b - f)} \quad (7.24)$$

Where a is defined as:

$$a = \cos(\theta) \cos(\phi) \cos(\chi) - \sin(\phi) \sin(\chi)$$

And b is defined as:

$$b = \sin(\theta) \cos(\phi)$$

This equation is based on the tangential force equilibrium. The complete derivation is explained in the thesis of Johnson (2019). The tangential velocity is obtained from the tangential velocity factor by Equation 7.18. This results in the nominal velocity vector, depicted in Equation 7.25.

$$v_t^{i,nom} = f_v(v_{k,r}, v_{k,\tau}) \quad (7.25)$$

Attitude Calculations

The only important angle in terms of attitude is the course angle because the other angles that represent the attitude can be deduced from the polar position coordinates. The course angle represents the direction of the tangent velocity of the kite. The zero degrees course angle points in the positive x -axis if the polar angle is zero. The course angle of the kite is in the first transition phase upwards and therefore 180° . In the next phase, the retraction phase, the course angle is also 180° . In the second transition phase the course angle points downwards and is therefore zero degrees. The course angle of the kite during the retraction phase depends on the shape of the figure eight, or so called Lissajous curve, and on the location in the figure eight. The course angle is defined in the reel-out phase by Equation 7.26.

$$\chi = \tan^{-1} \left(\frac{A_\theta \cos(2s)}{A_\phi \cos(s+C)} \right) \quad (7.26)$$

Where A_θ defines half of the figure eight curve height and A_ϕ represents half the width of the figure eight curve. These variables are predefined. C represents a phase shift and s is a dimensionless "positional time step" that represent the position along one figure eight curve. For this variable, a value of 0 , π , or 2π would be at the center point of the figure eight. The dimensionless positional time step is updated every time step, as depicted in Equation 7.27.

$$s = s + \Delta s \quad (7.27)$$

Where:

$$\Delta s = \frac{\Delta L}{\sqrt{(d\beta)^2 + (d\phi)^2}} \quad (7.28)$$

Where ΔL is the distance traveled during reel-out in one time step. This is modelled by Equation 7.29.

$$\Delta L = \frac{v_{k,\tau} \Delta t}{r} \quad (7.29)$$

The derivatives of the elevation $d\beta$ and azimuth angle $d\phi$ are obtained by Equation 7.30 and Equation 7.31, respectively.

$$d\beta = 2A_\theta \cos(2s) \quad (7.30)$$

$$d\phi = A_{\phi} \cos(s + C) \quad (7.31)$$

The course angle is the only angle that represents the attitude, as explained earlier. Therefore, the course angle represents the nominal attitude, as depicted in Equation 7.32.

$$\theta_t^{i,nom} = f_{\theta}(\chi) \quad (7.32)$$

Position Calculations

The position vector consists of the radius r , the elevation angle β , and the azimuth angle ϕ . The radius is modelled by Equation 7.33.

$$r = r_0 + v_{k,r} \Delta t \quad (7.33)$$

Where r_0 is the radius at the previous time step. The elevation angle is obtained by Equation 7.34.

$$\beta = \beta_0 + v_{\beta} \Delta t \quad (7.34)$$

Where β_0 is the elevation angle at the previous time step. The elevation velocity v_{β} is obtained by Equation 7.35.

$$v_{\beta} = \frac{v_w \lambda \cos(\chi)}{r} \quad (7.35)$$

The azimuth angle is obtained by Equation 7.36.

$$\phi = \phi_0 + v_{\phi} \Delta t \quad (7.36)$$

Where ϕ_0 is the azimuth angle at the previous time step. The azimuth velocity v_{ϕ} is obtained by Equation 7.37.

$$v_{\phi} = \frac{v_w \lambda \sin(\chi)}{r} \quad (7.37)$$

Therefore, the radius r , the elevation angle β , and the azimuth angle ϕ represent the nominal position vector, as depicted in Equation 7.38.

$$s_t^{i,nom} = f_s(r, \beta, \phi) \quad (7.38)$$

Model Output

The output of the flight path model consists of the obtained vectors, the duration of the different phases, and the total duration of the cycle. Therefore, the output of the flight path model consists of five components:

- The nominal position vector $s_t^{i,nom}$ for the entire flight cycle, depicted in Equation 7.38.
- The nominal velocity vector $v_t^{i,nom}$ for the entire flight cycle, depicted in Equation 7.25.
- The nominal attitude vector $\theta_t^{i,nom}$ for the entire flight cycle, depicted in Equation 7.32.
- The duration of the four flight phases: The duration of every flight phase is obtained from the 3D model by the summation of the flight phases its time steps.
- The duration of the nominal flight path T_{nom} : The nominal flight path duration is obtained from the 3D model by the summation of all the time steps.

7.3 Event Rate Specification

In this section the event rate $\lambda_{i,e}(t)$ is specified for the tether failure situation of step 2 from the model framework. As explained, the flight cycle of the kite consists of four phases: reel-out, first transition, reel-in, and the second transition phase. The rate of event $\lambda_{i,e}(t)$ depends on the phase. A tether failure happens more frequently with high tether loads. During the reel-out phase the loads on the tether are relatively high. The loads on the tether are relatively low during the first transition, reel-in, and second transition phase.

Assumption 7.3: The rate of event $\lambda_{i,e}(t)$ is zero between the start of the first transition and the end of the second transition $t_{Start Out}^{i,k}$.

Assumption 7.3 is mathematically formulated as:

$$\lambda_{i,e}(t) = 0 \text{ if } t \in [0, t_{Start Out}^{i,k}]$$

Assumption 7.4: The rate of event $\lambda_{i,e}(t)$ has a uniform distribution between the start of the reel-out phase $t_{Start Out}^{i,k}$ and the end of the reel-out phase.

Assumption 7.4 is mathematically formulated as:

$$\lambda_{i,e}(t) = \lambda_{Tether Failure}^{Reel-out} \text{ if } t \in [t_{Start Out}^{i,k}, T_i^{nom}]$$

Where T_i^{nom} is the duration of the nominal flight cycle i and thus the end of the nominal flight cycle. The end of the nominal flight cycle is the same moment in time as the end of the reel-out phase.

7.4 Non-nominal Descend Model

In this section the non-nominal descend model is explained in detail. This model concerns the glide to the ground in case of a tether failure. The non-nominal descend model uses differential equations, introduced in substep 3.3, to obtain the velocity v_t and position s_t of the kite. The acceleration is obtained by force calculations. The differential equations are depicted in Equation 7.39.

$$\begin{aligned}
\dot{s}_t &= \dot{v}_t \\
\dot{v}_t &= a_t \\
a_t &= \frac{L(\alpha) + D(\alpha) + W + T}{m_{kite} + m_{KCU} + m_{Tether}(l)}
\end{aligned} \tag{7.39}$$

Assumption 7.5: The kite is modelled as a point mass in a three-dimensional space during the non-nominal descend.

From Wind fixed reference frame to Earth fixed reference frame

In the non-nominal descend model the earth fixed reference frame is used. The earth fixed reference frame is depicted in Figure 7.7. The reference system is nearly the same as the cartesian reference system of the flight path model. The only difference is that this reference system is an earth fixed reference system instead of wind fixed reference system. The origin is located at the location of the ground station. The positive x -axis points to the geographical north in the earth fixed coordinate system. Secondly, the positive y -axis points to the geographical west. Lastly, the positive z -axis points upwards. The polar angle of the kite is represented by θ . The polar angle represents the angle between the tether and the positive z -axis. Next, the azimuth is represented by ϕ . The azimuth is the horizontal angle of the tether with respect to the positive x -axis.

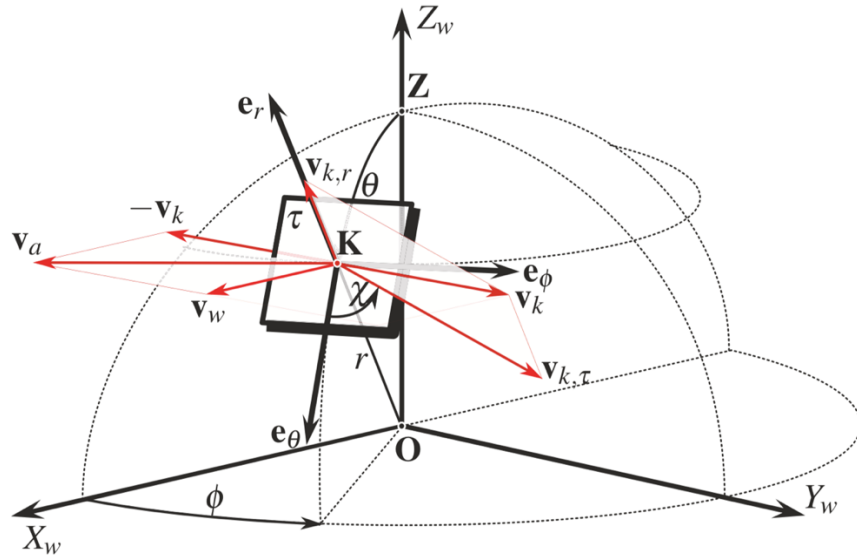


Figure 7.7: The reference system of the non-nominal descend model [Ahrens, 2013].

State Conversion

The position and velocity at the start of the simulation, just before the tether failure, are obtained from the flight path model. The flight path model simulates the position in polar coordinates (r, θ, ϕ) in the wind fixed reference frame. The position in the earth fixed cartesian coordinate frame (x, y, z) is obtained by calculating the cartesian coordinates in the wind fixed reference frame and transferring the coordinates to the earth fixed reference frame by turning around the z -axis with the wind heading $\phi_{t_e}^{wind}$. This results in the transfer equation depicted in Equation 7.40.

$$s_t = \begin{bmatrix} x_t \\ y_t \\ z_t \end{bmatrix} = \begin{bmatrix} r_t \sin(\theta_t) \cos(\phi_t + \phi_t^{wind}) \\ r_t \sin(\theta_t) \sin(\phi_t + \phi_t^{wind}) \\ r_t \cos(\theta_t) \end{bmatrix} \tag{7.40}$$

Where r_t is the radial distance between the kite and the ground station at time t , θ_t is the polar angle at time t , ϕ_t is the azimuth at time t , and s_t is the position vector in the earth fixed reference frame at time t . The flight path model simulates the velocity at time t with the radial velocity $v_t^{k,r}$, tangential velocity $v_t^{k,\tau}$, and course angle χ_t . Therefore, the velocity vector v_t in the earth fixed reference frame is obtained by Equation 7.41.

$$v_t = \begin{bmatrix} v_t^x \\ v_t^y \\ v_t^z \end{bmatrix} = \begin{bmatrix} v_t^{k,\tau}(\cos(\chi_t)\cos(\theta_t)\cos(\phi_t + \phi_t^{wind}) - \sin(\chi_t)\sin(\phi_t)) + v_t^{k,r}(\sin(\theta_t)\cos(\phi_t + \phi_t^{wind})) \\ v_t^{k,\tau}(\cos(\chi_t)\cos(\theta_t)\sin(\phi_t + \phi_t^{wind}) + \sin(\chi_t)\cos(\phi_t)) + v_t^{k,r}(\sin(\theta_t)\cos(\phi_t + \phi_t^{wind})) \\ -v_t^{k,\tau}\cos(\chi_t)\sin(\theta_t) + v_t^{k,r}\cos(\theta_t) \end{bmatrix} \quad (7.41)$$

Acceleration Model

The acceleration vector of the kite is needed in the differential equations. The acceleration vector is obtained in the earlier described earth fixed reference frame. The acceleration is obtained by the force summation in the x , y , and z direction. Firstly, the forces in the x direction at time t consist of the lift force component L_t^x , the drag force component D_t^x , and the tether force component $F_{T_t}^x$.

Secondly, the forces in the y direction at time t also consist of the lift force component L_t^y , the drag force component D_t^y , and the tether force component $F_{T_t}^y$. Lastly, the forces in the z direction at time t consist of the lift force component in the z direction L_t^z , the drag force component in the z direction D_t^z , the tether force component in the z direction $F_{T_t}^z$, and the weight W_t . Therefore, the acceleration vector a_t is mathematically defined in Equation 7.42.

$$a_t = \begin{bmatrix} a_t^x \\ a_t^y \\ a_t^z \end{bmatrix} = \begin{bmatrix} \frac{L_t^x + D_t^x + F_{T_t}^x}{m_{KCU} + m_{kite} + m_{tether}(l_t)} \\ \frac{L_t^y + D_t^y + F_{T_t}^y}{m_{KCU} + m_{kite} + m_{tether}(l_t)} \\ \frac{L_t^z + D_t^z + F_{T_t}^z - W_t}{m_{KCU} + m_{kite} + m_{tether}(l_t)} \end{bmatrix} \quad (7.42)$$

Where m_{KCU} is the mass of the KCU in kg, m_{kite} is the mass of the kite in kg, and $m_{tether}(l_t)$ is the mass of the tether in kg. The mass of the tether depends on the length of the tether l_t , the tether is a 14mm Dyneema rope. The mass of the tether is obtained by Equation 7.43.

$$m_{tether}(l_t) = \rho_{tether} \pi r^2 l_t \quad (7.43)$$

Where r is the radius of the tether in meters and ρ_{tether} is the density of the tether in kg/m^3 . The lift force, drag force, and tether force depend on the type of event e . In this thesis only a tether failure is considered. The forces in case of a tether failure are specified in the next part of this section. In all scenarios the weight is pointing in the same direction and has the same magnitude. Therefore, the weight is obtained by Equation 7.44.

$$W_t = g(m_{KCU} + m_{kite} + m_{Tether}(l_t)) \quad (7.44)$$

Where g is the gravitational acceleration.

Tether Failure Forces

In this part the force modelling during a tether failure is explained. During a tether failure the tether breaks. Several assumptions are made to model these forces.

Assumption 7.6: The tether force is zero in case of a tether failure.

During a tether failure, the tether is not attached to the ground station anymore. Assumption 7.6 sets the tether force at zero, this also means that the ground drag caused by the tether is neglected. Therefore, the tether force is mathematically defined in Equation 7.45.

$$F_{T_t} = \begin{bmatrix} F_{T_t}^x \\ F_{T_t}^y \\ F_{T_t}^z \end{bmatrix} = 0 \quad (7.45)$$

Assumption 7.7: The integration of the differential equations is performed by a first order Euler integration with time step Δt .

Assumption 7.8: The wind is zero in the z direction.

Due to assumption 7.7 and 7.8 the wind vector is obtained by Equation 7.46.

$$v_{wind,t_{\ell+1}}^{i,k} = \begin{bmatrix} v_{wind,t_{\ell}}^{x,i,k} + \varepsilon_{t_{\ell+1}}^x \\ v_{wind,t_{\ell}}^{y,i,k} + \varepsilon_{t_{\ell+1}}^y \\ 0 \end{bmatrix} \quad (7.46)$$

Where $v_{wind,t_{\ell+1}}^{i,k}$ is the wind vector at the next time step $t_{\ell+1}$ and $\varepsilon_{t_{\ell+1}}$ is the wind gust vector at the next time step $t_{\ell+1}$. The wind vector $v_{wind,t_{\ell}}^{i,k}$ is the wind vector of the current time step t_{ℓ} . The wind vector of the first time step is obtained from the KNMI (2021) wind data and recalculated for the altitude of the kite as explained in section 7.2 with Equation 7.17. The wind gust vector is the vector that accounts for the variance in wind. The approach of Brezoescu (2013) is adopted to obtain turbulence time series in the air around the kite. In the approach of Brezoescu (2013) the so called Dryden turbulence model is used. The Dryden wind turbulence model produces a turbulence value at altitude based on the wind vector at six meters above the ground, the velocity vector of the apparent wind, a gust scale length, and a turbulence intensity vector, of which the latter two are dependent of altitude.

Assumption 7.9: The wind vector measurement from the KNMI (2021) have the same value as the wind measured at six meters above the ground.

Assumption 7.10: The turbulence only occur in the x and y direction and not in the z direction.

Therefore, the turbulence is only calculated in the x and y direction. Turbulence samples are obtained by generating a random discrete white noise signal, and filtering it with the discrete Dryden filter. The random discrete white noise signal is a Gaussian signal with a zero mean and a variance of one. Samples are generated with a sample period T_s and fed to the Dryden filter. The gusts are calculated in the x and y direction by Equation 7.47.

$$\varepsilon_{t_{\ell+1}} = \begin{bmatrix} \varepsilon_{t_{\ell+1}}^x \\ \varepsilon_{t_{\ell+1}}^y \\ \varepsilon_{t_{\ell+1}}^z \\ 0 \end{bmatrix} = \begin{bmatrix} \left(1 - \frac{V_{aw,t_{\ell}}^x}{L_u} T_s\right) \varepsilon_{t_{\ell}}^x + \sqrt{2 \frac{V_{aw,t_{\ell}}^x}{L_u} T_s} \sigma_{t_{\ell}}^x \eta_1 \\ \left(1 - \frac{V_{aw,t_{\ell}}^y}{L_u} T_s\right) \varepsilon_{t_{\ell}}^y + \sqrt{2 \frac{V_{aw,t_{\ell}}^y}{L_u} T_s} \sigma_{t_{\ell}}^y \eta_1 \\ 0 \end{bmatrix} \quad (7.47)$$

Where $v_{aw,t_{\ell}}$ represents the apparent wind vector at time step t_{ℓ} in ft/s, L_u is the turbulence scale length in ft, $\sigma_{t_{\ell}}$ is the turbulence intensity at time step t_{ℓ} in ft/s, and η_1 is the generated white noise sample. The turbulence scale and turbulence intensity are calculated by Equation 7.48 and 7.49, respectively.

$$L_u = \frac{z}{(0.177 + 0.0000823z)^{1.2}} \quad (7.48)$$

$$\sigma_{t_j} = \begin{bmatrix} \sigma_{t_{\ell}}^x \\ \sigma_{t_{\ell}}^y \\ \sigma_{t_{\ell}}^z \\ 0 \end{bmatrix} = \begin{bmatrix} \frac{0.1 v_{wind_{ref},t_{\ell}}^{x,i,k}}{(0.177 + 0.000823z)^{0.4}} \\ \frac{0.1 v_{wind_{ref},t_{\ell}}^{y,i,k}}{(0.177 + 0.000823z)^{0.4}} \\ 0 \end{bmatrix} \quad (7.49)$$

Where $v_{wind_{ref},t_{\ell}}^{i,k}$ is the wind vector at the wind sensor in ft/s and z is the height above the ground in ft. The apparent wind vector is obtained by using the obtained wind vector $v_{wind,t_{\ell}}^{i,k}$ and velocity vector $v_{t_{\ell}}^{i,k}$ at time t_{ℓ} . The apparent wind vector $v_{aw,t_{\ell}}$ is modelled by Equation 7.50.

$$v_{aw,t_{\ell}} = \begin{bmatrix} v_{aw,t_{\ell}}^x \\ v_{aw,t_{\ell}}^y \\ v_{aw,t_{\ell}}^z \end{bmatrix} = \begin{bmatrix} v_{wind,t_{\ell}}^{x,i,k} - v_{t_{\ell}}^{x,i,k} \\ v_{wind,t_{\ell}}^{y,i,k} - v_{t_{\ell}}^{y,i,k} \\ -v_{t_{\ell}}^{z,i,k} \end{bmatrix} \quad (7.50)$$

In order to model the lift and drag force some assumptions need to be made.

Assumption 7.11: The lift force is perpendicular to the apparent wind [Ruijgrok, 2009].

Assumption 7.12: After the tether failure the KCU hangs directly under the kite.

In real life the kite does rotate after tether failure. However, in the available tether failure data it is observed that this phase can be neglected because of its short duration and its negligible influence on the velocity and on the position. Therefore, assumption 7.12 is a valid assumption.

Assumption 7.13: The pitch and roll rates are zero during the simulation of the tether failure.

Due to assumption 7.12 and assumption 7.13 it is assumed that during the tether failure the angle of attack is defined as Equation 7.51.

$$\alpha_{t_{\ell}} = \theta_{Kite,t_{\ell}} + \theta_{aw,t_{\ell}} \quad (7.51)$$

Where θ_{kite,t_ℓ} is the reference pitch of the kite, the pitch of the kite if the KCU is directly located under the kite. θ_{aw,t_ℓ} is the vertical apparent wind direction, the angle between the horizon and the apparent wind vector. The vertical apparent wind direction is obtained by Equation 7.52.

$$\theta_{aw,t_\ell} = \tan^{-1} \left(\frac{v_{aw,t_\ell}^z}{\sqrt{v_{aw,t_\ell}^x{}^2 + v_{aw,t_\ell}^y{}^2}} \right) \quad (7.52)$$

The vertical and horizontal apparent wind direction are needed to obtain the lift force. The horizontal apparent wind direction is obtained by Equation 7.53.

$$\phi_{aw,t_\ell} = \tan^{-1} \left(\frac{v_{aw,t_\ell}^y}{v_{aw,t_\ell}^x} \right) \quad (7.53)$$

The magnitude of the lift force is obtained by Equation 7.54.

$$|L_{t_\ell}(\alpha_{t_\ell})| = -\frac{1}{2} C_L(\alpha_{t_\ell}) S \rho_w |v_{aw,t_\ell}|^2 \quad (7.54)$$

Where $|v_{aw,t_\ell}|$ is the magnitude of the apparent wind at time t_ℓ , $C_L(\alpha_{t_\ell})$ is the lift coefficient with the angle of attack α_{t_ℓ} at time t_ℓ as input, and S is the projected surface area. The air density ρ_w depends on the altitude and is obtained by Equation 7.55.

$$\rho_w = \rho_0 \frac{-z}{H_p} \quad (7.55)$$

Where ρ_0 is the air density at zero altitude and H_p is the scale height for air density. The direction of the lift force is modelled by taking into account assumption 7.11 and 7.12. This means that the lift force is perpendicular to the apparent wind and upwards. Therefore, the vector of the lift force is obtained by Equation 7.56.

$$L_{t_\ell} = \begin{bmatrix} L_{t_\ell}^x \\ L_{t_\ell}^y \\ L_{t_\ell}^z \end{bmatrix} = \begin{bmatrix} -|L_{t_\ell}| \sin(\theta_{aw,t_\ell}) \cos(\phi_{aw,t_\ell}) \\ -|L_{t_\ell}| \sin(\theta_{aw,t_\ell}) \sin(\phi_{aw,t_\ell}) \\ |L_{t_\ell}| \cos(\theta_{aw,t_\ell}) \end{bmatrix} \quad (7.56)$$

Assumption 7.14: The direction of the drag force is in the same direction as the apparent wind [Ruijgrok, 2009].

The magnitude of the drag force is calculated by Equation 7.57.

$$|D_{t_\ell}(\alpha_{t_\ell})| = -\frac{1}{2} C_D(\alpha_{t_\ell}) S \rho_w |v_{aw,t_\ell}|^2 \quad (7.57)$$

Where $C_D(\alpha_{t_\ell})$ is the drag coefficient at time t_ℓ with the angle of attack α_{t_ℓ} as input. The drag force vector is obtained by Equation 7.58.

$$D_{t_\ell} = \begin{bmatrix} D_{t_\ell}^x \\ D_{t_\ell}^y \\ D_{t_\ell}^z \end{bmatrix} = \begin{bmatrix} -|D_{t_\ell}| \cos(\theta_{aw,t_\ell}) \cos(\phi_{aw,t_\ell}) \\ -|D_{t_\ell}| \cos(\theta_{aw,t_\ell}) \sin(\phi_{aw,t_\ell}) \\ |D_{t_\ell}| \sin(\theta_{aw,t_\ell}) \end{bmatrix} \quad (7.58)$$

These formulas take into account assumption 7.14, the direction of the drag force is in the same direction as the apparent wind.

7.5 Unprotected Fatality Model

The probability of fatality is needed in step 5 of the third-party risk model framework from Blom et al. (2020). Blom et al. (2020) make use of the Range Commanders Council (2001) adopted Feinsein model, depicted in Equation 7.59.

$$P(Fly \in A(i, H), v) = Z\left(\frac{\ln(E_{imp}) - \ln(a)}{b}\right) \quad (7.59)$$

Where Z is the cumulative standard normal distribution, a is the mid-point value, b is the standard deviation, and E_{imp} is the kinetic energy of the kite at the moment of the ground crash.

Assumption 7.15: The kinetic energy of the KCU and the kite are both considered.

Due to assumption 7.1 and 7.15 the kinetic energy of the kite and KCU are separately modelled. The kinetic energy of the kite E_{imp}^{kite} is obtained by Equation 7.60.

$$E_{imp}^{kite} = \frac{1}{2} m_{Kite} |v_t^{i,k}|^2 \quad (7.60)$$

Where $|v_t^{i,k}|$ is the magnitude of the velocity vector of the kite of the i -th flight cycle of the k -th crash simulation at time t . The kinetic energy of the KCU E_{imp}^{KCU} is obtained by Equation 7.61.

$$E_{imp}^{KCU} = \frac{1}{2} m_{KCU} |v_t^{i,k}|^2 \quad (7.61)$$

The kinetic energy of the kite and KCU is used to obtain the probability of fatality of the kite $P(Fly \in A(i, H), v)_{kite}$ and KCU $P(Fly \in A(i, H), v)_{KCU}$. In Equation 7.10 the multiplication of the probability of unprotected fatality and total impact area is needed. This is obtained by Equation 7.62.

$$\frac{\sum_{k=1}^{K_i} [1[s_{c,e}^{i,k} \in G_j]] \left(|A(i,e)_{KCU}| Z\left(\frac{\ln\left(\frac{1}{2} m_{KCU} |v_t^{i,k}|^2\right) - \ln(a)}{b}\right) + |A(i,e)_{kite}| Z\left(\frac{\ln\left(\frac{1}{2} m_{kite} |v_t^{i,k}|^2\right) - \ln(a)}{b}\right) \right)}{K_i \widehat{P}(j|i,e)} \quad (7.62)$$

8 Model Implementation,

Verification, and Validation

In chapter 7 the model of the safety risk assessment is discussed. In this chapter the exact implementation, of the model described in chapter 7, in python is explained. Furthermore, the model is verified and validated in this chapter. Firstly, the model implementation is explained in section 8.1. Secondly, the flight path model is verified in section 8.2. Next, the non-nominal descend model is verified in section 8.3. The non-nominal descend model is validated with a real tether failure scenario in section 8.4. Lastly, the wind turbulence (Dryden) model is verified in section 8.5.

8.1 Model Implementation

The implementation of the model is explained in this section. The model is developed in the open source Python programming language. The python code consists of several parts, these are all explained in this section.

Wind Data

The first part of the code is the processing of the wind data from KNMI (2021). The wind data of the station Marknesse from the KNMI is from January 1989 until August 2021. This wind data is divided in wind velocity grid steps with step size $|\Delta v_w|$ and divided in wind direction grid steps with step size Δv_w^{hdg} . The outcome of this part of the code is the probability that every wind condition occur with a certain wind velocity grid step and wind direction grid step. In Figure 9.1 the wind rose of Marknesse is depicted, the KNMI station that is used as an estimation for the windconditions at Rutten.

Flight Path Model

The second part of the code is the flight path model of Johnson (2019). The wind velocity is used as an input parameter to the flight path model, as explained in section 7.2. The flight path model is runned for all the different wind conditions. Next, the velocities and position of the complete cycle is transferred to the earth fixed reference frame for all the possible flight paths. These values and the cycle durations are the inputs for the non-nominal descend model and the individual risk modelling.

Non-nominal Descend Model

The third part of the code is the non-nominal descend model. The input values for this model are the previously mentioned flight paths and the probabilities that certain wind conditions occur. Therefore, the number of cycles per wind condition per year are obtained first. Now, all the flight paths during the year are known the exact inputs of the non-nominal descend model are known. Next, a loop in a loop is started where for every flight path the non-nominal descend model is executed K times. The non-nominal descend starts in every simulation by choosing a random tether failure moment with a uniform randomizer between the start of the reel-out phase and the

end of the reel-out phase. Next, the random flight path deviation is added to the position at this tether failure moment according to Equation 7.3 and Equation 7.4. Subsequently, for every time step Δt the forces, velocity, and position of the kite is obtained as explained in section 7.4. The wind is varied by the described Dryden filter and is updated for every time step as well. The simulation stops if the height above the ground is zero. The position and velocities are saved for every simulation.

Individual Risk

The fourth part of the code is the individual risk part. Firstly, the estimated probability, $\widehat{P}(j|i, e)$, that the simulated crash locations is in grid cell G_j is obtained. This is obtained by counting the number of crashes in every grid cell for every cycle. This number is divided by K , the number of simulations. Next, the estimate of the local hit density, $\widehat{p}_s(y_i|i, e)$, is obtained. This is performed by dividing $\widehat{P}(j|i, e)$ with the grid size $|G_j|$.

Subsequently, for every crash the probability of fatality is obtained. The saved velocities are used to determine the kinetic energy for the KCU and kite. Next, the probability of fatality is calculated for both the KCU and kite by the Range Commanders Council (2001) adopted Feinstein model as explained in section 7.5.

Now the probability of fatality is known, the individual risk per cycle is obtained by Equation 7.10. The multiplication of the crash impact area $|A(i, e)|$ and the probability of fatality $P(\text{Fly} \in A(i, H), v)$ is modelled as explained in section 7.5. Lastly, the individual risk per year is obtained by Equation 7.11 and plotted on a map, the results are displayed in chapter 9.

Collective Ground Risk

The last part of the code is the collective ground risk code. Firstly, for every grid cell a population density is assigned. This is performed by using data of the CBS (2020). In this data polygons are presented in so called “Rijksdriehoeks coördinaten”. Every polygon has a population density value. The population density is assigned to each grid cell by converting the CBS (2020) polygons to the earth fixed reference frame with the ground station as the origin. A population density of zero is assigned to all the grid cells that are within the radius of 400m, the operational zone, because no third-parties are present here.

Secondly, the collective ground risk per cycle is obtained by Equation 7.13. To obtain the collective ground risk per flight hour the collective ground risk per cycle is divided by the duration of the complete cycle, the duration of every cycle is different for every wind condition. Therefore, this is performed for every wind heading grid step v_w^{hdg} and wind velocity grid step $\left| v_{wind_{ref}}^{i, nom} \right|$. The results are displayed in a histogram in chapter 9. Subsequently, the estimated collective ground risk per year is calculated by Equation 7.15. This result is also reported in chapter 9.

8.2 Flight Path Model Verification

The flight path model is verified by plotting the 3D position of the kite, the tangential velocity, radial velocity, and tether force. Johnson (2019) already verified the used flight path model for a 25m² kite. However, in this simulation a kite size of 60m² is used. Johnson (2019) has compared the flight path model with a real flight path, under the same weather conditions. The maximum deviation of the flight path was identified to be between the 28 and 29 meters by Johnson (2019). This was defined to be a good fit also because the number of Lissajous figures was the same as the real operation.

The verification of Johnson (2019) is only performed for one wind velocity. The verification of Johnson (2019) did not look into different wind velocities. The variation of the wind velocity is an important factor in this thesis because all the wind conditions are taken into account in this safety evaluation of Kitepower operations. Therefore, this verification focuses on the verification of the flight path model for different wind velocities. It is expected that the number of Lissajous figures decreases with an increasing wind velocity. Furthermore, it is important to note that only the flight path during the reel-out phase is relevant because this is the only moment that a tether failure could occur.

In Figure 8.1 until 8.10 it is observed that the flight path follows the expected path with its Lissajous figures, as already observed by Johnson (2019). During the real operations an important observation is that the number of Lissajous figures decreases with an increasing wind velocity. Firstly, in Figure 8.1 it is observed that with a wind velocity of 3 m/s there are four complete Lissajous figures in the reel-out phase. Next, in Figure 8.3 it is observed that with a wind velocity of 5 m/s there are three and a half Lissajous figures in the reel-out phase. Thirdly, in Figure 8.5 it is observed that with a wind velocity of 7 m/s there are three complete Lissajous figures in the reel-out phase. Subsequently, in Figure 8.7 it is observed that with a wind velocity of 9 m/s there are two and a half Lissajous figures in the reel-out phase. Lastly, in Figure 8.9 it is observed that with a wind velocity of 11 m/s there is one and a half Lissajous figure in the reel-out phase. It is concluded that the number of Lissajous figures indeed decreases with an increasing wind velocity. Therefore, this part of the flight path model is assumed to be correct.

During the real operations a decreasing cycle time with an increasing wind velocity is observed. This due to the higher reel-out velocity during higher wind velocities. This observation is also verified in the flight path model. In Figure 8.2, Figure 8.4, Figure 8.6, Figure 8.8, and Figure 8.10 it is observed that the cycle time indeed decreases with an increasing wind velocity. The cycle time is around 89 seconds with a wind velocity of 3 m/s, as depicted in Figure 8.2. The cycle time is around 66 seconds with a wind velocity of 11 m/s, as depicted in Figure 8.10. Therefore, the observation that the cycle time decreases with an increasing wind velocity is verified.

Thus far, only the position of the kite is verified. The tangential and reeling velocity should be verified as well because these velocities are also important output parameters of the flight path model. In terms of velocity and tether force the observations during a test flight are as follows:

- The tangential velocity oscillates for all the wind velocities in the reel-out phase. A low tangential velocity is observed during the turn. A high tangential velocity is observed in the centre of the Lissajous figure.
- The tether force oscillates for lower wind velocities if the maximum tether force is not reached in the reel-out phase. Therefore, the reeling velocity is constant in this situation.
- The reeling velocity oscillates for higher wind velocities if the maximum tether force is reached in the reel-out phase.

The first observation is confirmed in the flight path model. In Figure 8.1 until 8.10 it is observed that the tangential velocity oscillates, a low tangential velocity during the turn and a high tangential velocity in the centre of the Lissajous figure. The second observation is also confirmed by Figure 8.2, Figure 8.4, Figure 8.6, Figure 8.8, and Figure 8.10. At a wind velocity of 3 m/s the maximum tether force oscillates in the reel-out phase since the maximum tether force is not reached, as depicted in Figure 8.2. In Figure 8.4 it is observed that at a wind velocity of 5 m/s sometimes the tether force limit is reached in the reel-out phase. Therefore, during the reel-out phase sometimes the tether force oscillates and sometimes the reeling velocity oscillates. This is also observed in figure 8.6 with a wind velocity of 7 m/s. In Figure 8.8 and Figure 8.10 it is observed that the tether

force is constant at its limit in the reel-out phase and the reeling velocity oscillates during the reel-out phase. Therefore, the third observation is also verified.

All in all, all the observations during test flights are also observed in the flight path model. Therefore, it is assumed that the flight path model is accurate enough to predict the flight path of the kite for this safety evaluation.

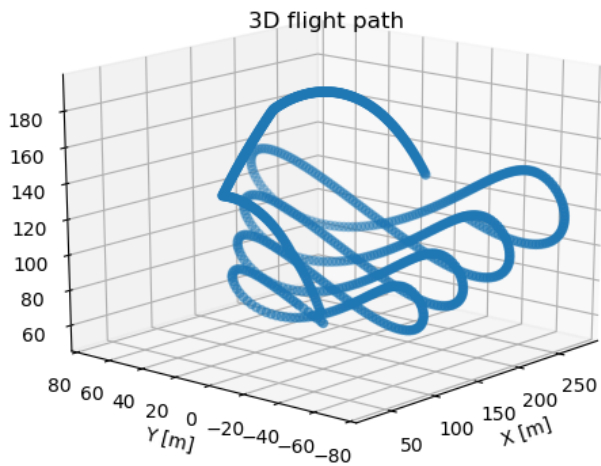


Figure 8.1: Generated nominal flight path with a wind velocity of 3 m/s.

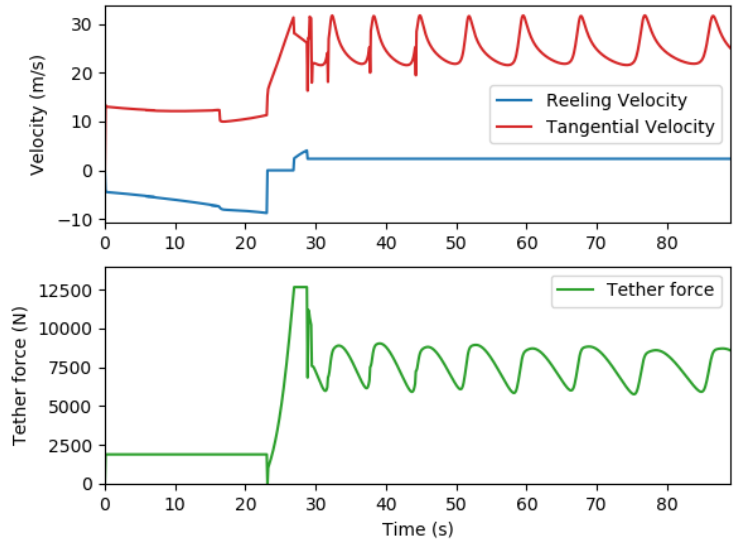


Figure 8.2: Reeling velocity, tangential velocity, and tether force during the nominal flight path with a wind velocity of 3 m/s.

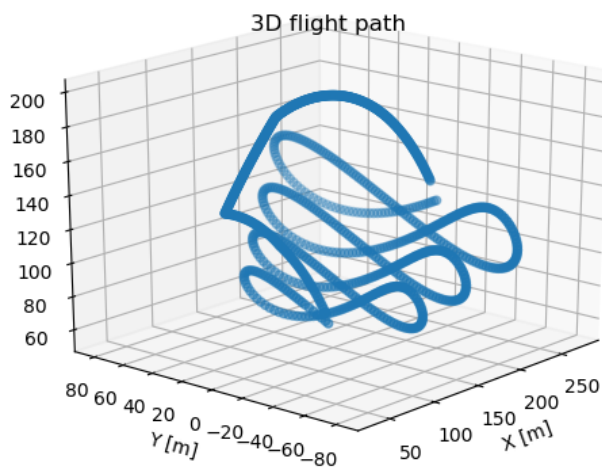


Figure 8.3: Generated nominal flight path with a wind velocity of 5 m/s.

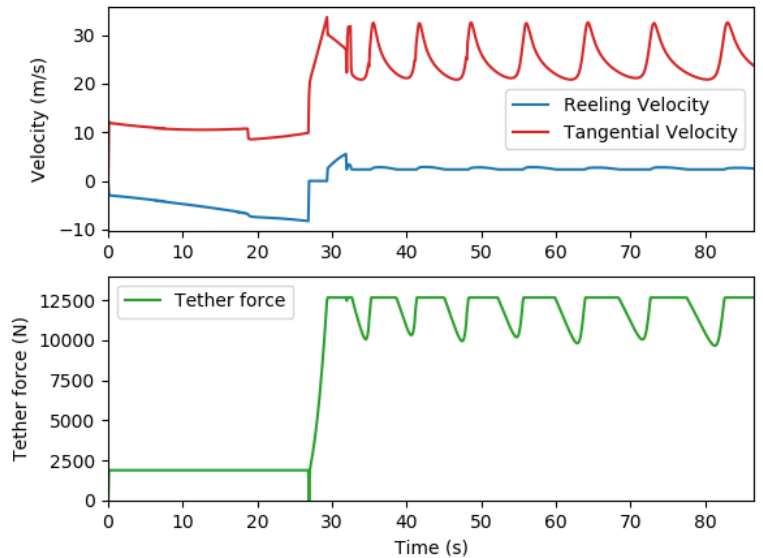


Figure 8.4: Reeling velocity, tangential velocity, and tether force during the nominal flight path with a wind velocity of 5 m/s.

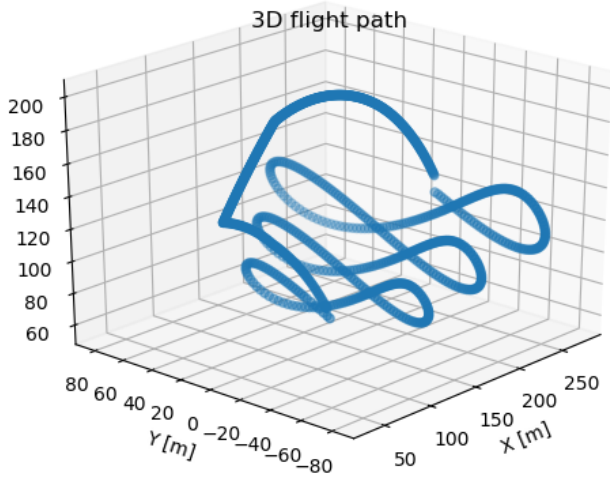


Figure 8.5: Generated nominal flight path with a wind velocity of 7 m/s.

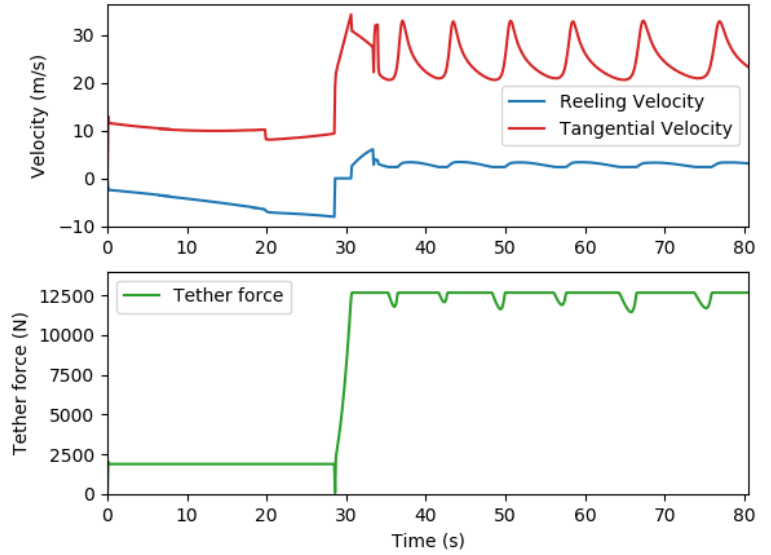


Figure 8.6: Reeling velocity, tangential velocity, and tether force during the nominal flight path with a wind velocity of 7 m/s.

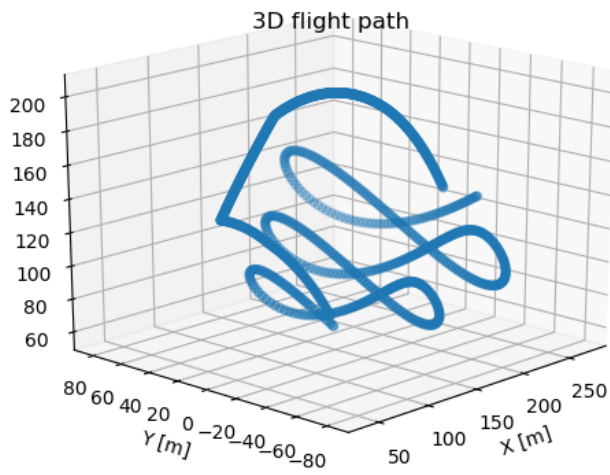


Figure 8.7: Generated nominal flight path with a wind velocity of 9 m/s.

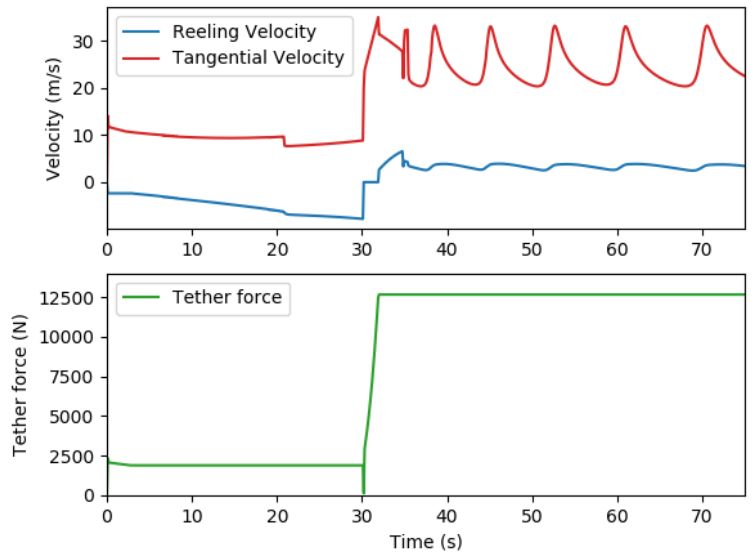


Figure 8.8: Reeling velocity, tangential velocity, and tether force during the nominal flight path with a wind velocity of 9 m/s.

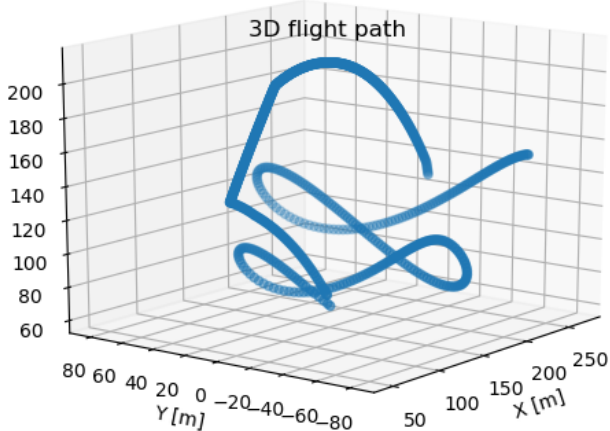


Figure 8.9: Generated nominal flight path with a wind velocity of 11 m/s.

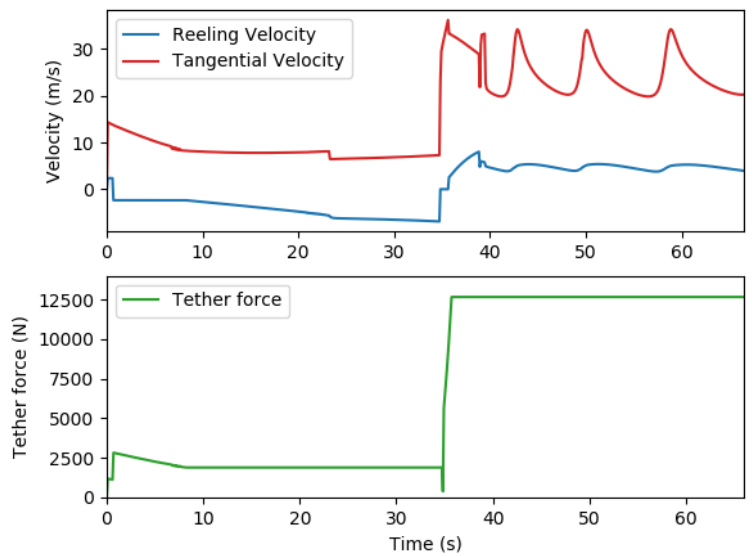


Figure 8.10: Reeling velocity, tangential velocity, and tether force during the nominal flight path with a wind velocity of 11 m/s.

8.3 Non-nominal Descend Model Verification

The non-nominal descend model is verified by generating a random input moment and observing the lift force, drag force, the apparent wind velocity, the velocity of the kite, the angle of attack, and the position of the kite. In this section the behaviour of these parameters are discussed.

The random input values are depicted in Table 8.1. These are randomly generated by choosing a random moment of the tether failure during the reel-out phase with wind coming from the south and with a wind velocity of 7 m/s.

Table 8.1: Input values of the non-nominal descend model.

Variable	Symbol	Value
Time	t	44.84 s
Location	x	180.05 m
	y	-15.60 m
	z	86.54 m
Elevation	β	0.447 rad
Azimuth	ϕ	-0.0864 rad
Course Angle	χ	-1.85 rad
Radial Velocity	$v_t^{k,r}$	4.43 m/s
Tangential Velocity	$v_t^{k,\tau}$	21.67 m/s
Wind Velocity	$v_{wind_ref}^{i,nom}$	7 m/s
Wind Direction	v_w^{hdg}	0°

The flight path during the non-nominal descend is verified by observing the previously mentioned parameters. The flight path of the non-nominal descend after the tether failure is depicted in Figure 8.11. In Figure 8.12 the apparent wind velocity and the velocity of the kite are depicted. Next, in Figure 8.13 the angle of attack is depicted. In Figure 8.14 the lift force and drag force are depicted. In Figure 8.11 it is observed that the kite first flies sideward and a little bit upwards, just after the tether failure. This is the expected behaviour because, just after the tether failure, the tether force that points down and sideward suddenly disappears. Furthermore, the original kite velocity, before tether failure, is sideward. Therefore, a sideward and little bit upwards movement is expected and observed in the simulation. Due to this initial sideward movement the apparent wind velocity is initially in the positive y direction, as depicted in 8.12. Due to the upward movement the apparent wind velocity is in the negative z direction. Due to this upward movement the angle of attack is negative, as depicted in 8.13. As expected, the drag force points in the same direction as the apparent wind due to assumption 7.14 [Ruijgrok, 2009]. The lift force points heavily to the positive z direction due to the high apparent velocity in the negative y direction, just after tether failure. The lift force is upwards and perpendicular to the apparent wind due to assumption 7.11 and 7.12. This lift force is also the cause of the previously mentioned initial upward movement.

In Figure 8.11 it is also observed that after a while the flight path is slowly curved downward and in the direction of the wind. The curvature in the direction of the wind is mainly due to the drag force as observed in Figure 8.14. The high apparent wind velocity in the positive y direction causes a high drag force in the same direction. Therefore, the kite decelerates in the y direction. The drag force in the y direction first decreases due to the decreasing apparent wind velocity. Later it shortly increases again, due to the increasing angle of attack which is caused by the downward movement. The cause of this increase in angle of attack is later explained in this section. However, the drag force in the y direction still moves to zero due to the disappearance of the apparent wind velocity in the y direction.

The curvature downward is mainly due to the decrease in lift force. The lift force drops quickly due to the disappearance of the apparent wind velocity in the y direction. However, due to the increase in angle of attack, mentioned earlier, the lift increases again. This change in lift force is not observed in the velocity of the kite. This due to the fact that the drag in the z direction also increases, which compensates this drop.

In the end, the horizontal apparent wind gradually becomes zero because the drag force is in the same direction as the apparent wind [Ruijgrok, 2009]. Only apparent wind in the z direction is present due to the downward movement. Therefore, the angle of attack gradually increase to around 95 degrees, 90 degrees (the downward direction) plus 5 degrees (the reference pitch angle). The kite acts in this situation as a parachute moving down and moving in the direction of the wind. The downward movement is caused by the gravity force and counteracted by the drag force. The lift force is zero because of the angle of attack of 95 degrees. The lift coefficient is zero with an angle of attack of 95 degrees. This results in a steady downward kite velocity with the equilibrium velocity and sideward by the velocity of the wind until the kite touches the ground. All in all, the model behaves as expected and is therefore verified.

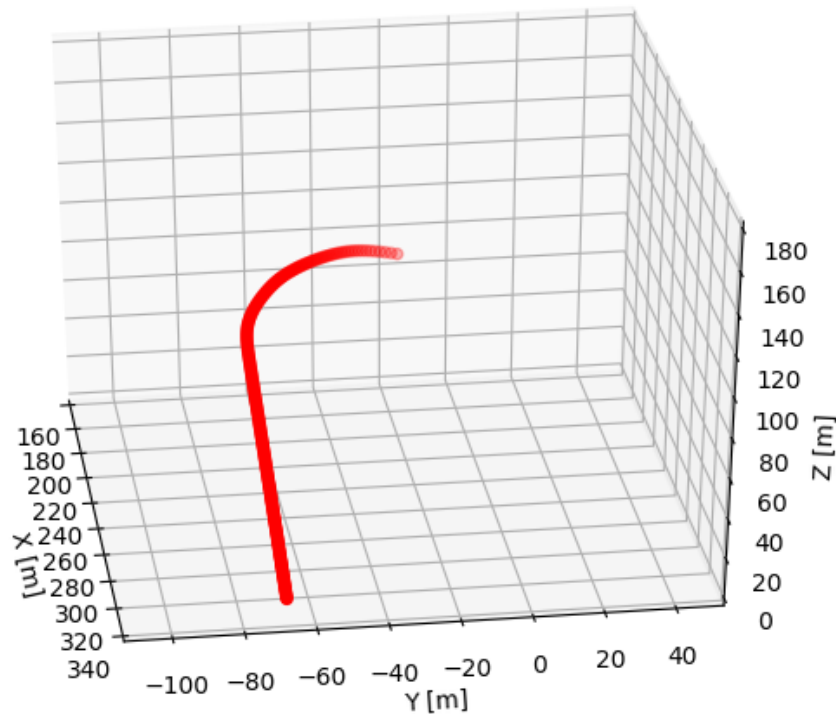


Figure 8.11: The flight path of the non-nominal descend model.

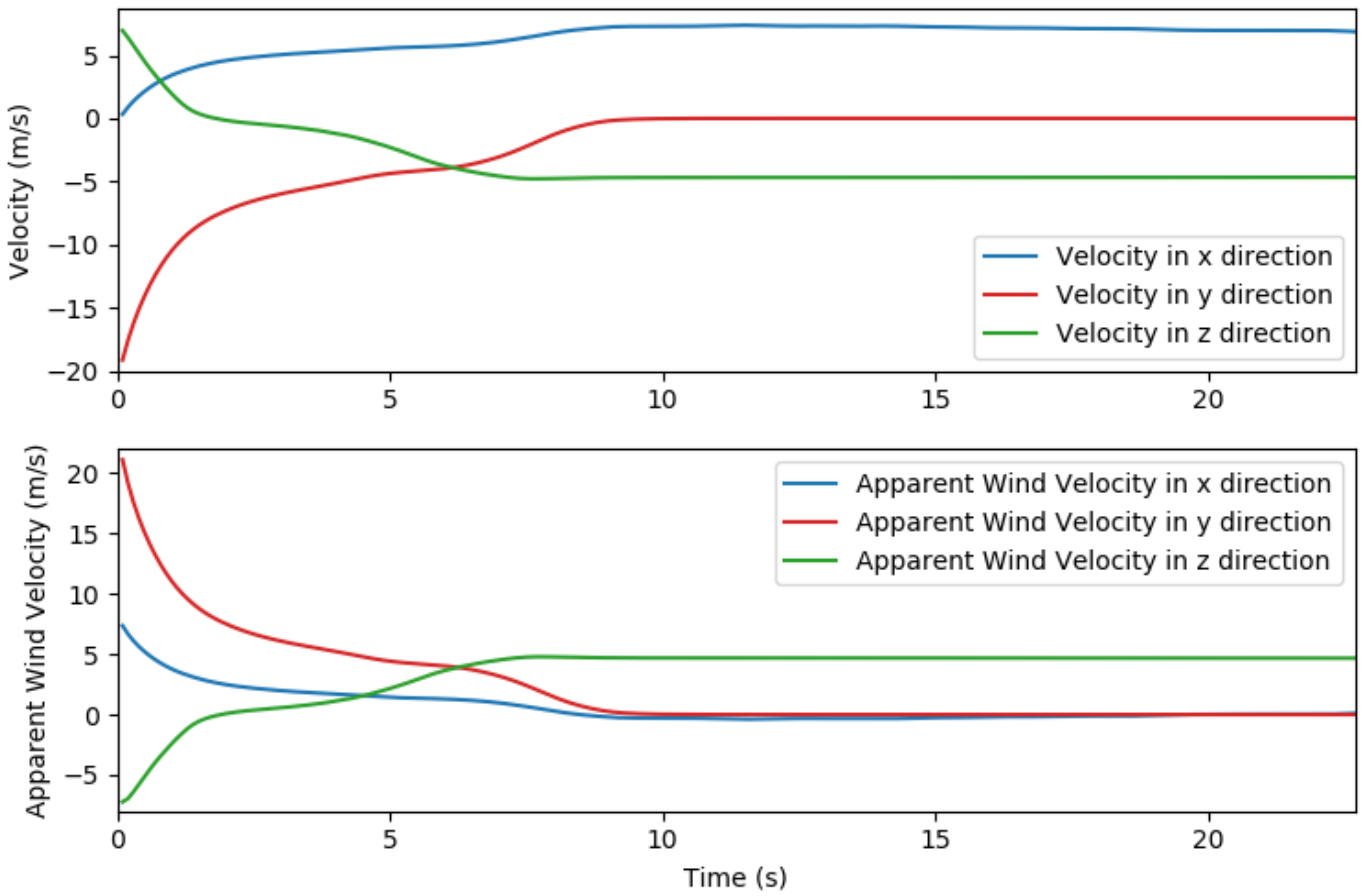


Figure 8.12: Apparent wind velocity and velocity of the kite during a non-nominal descend.

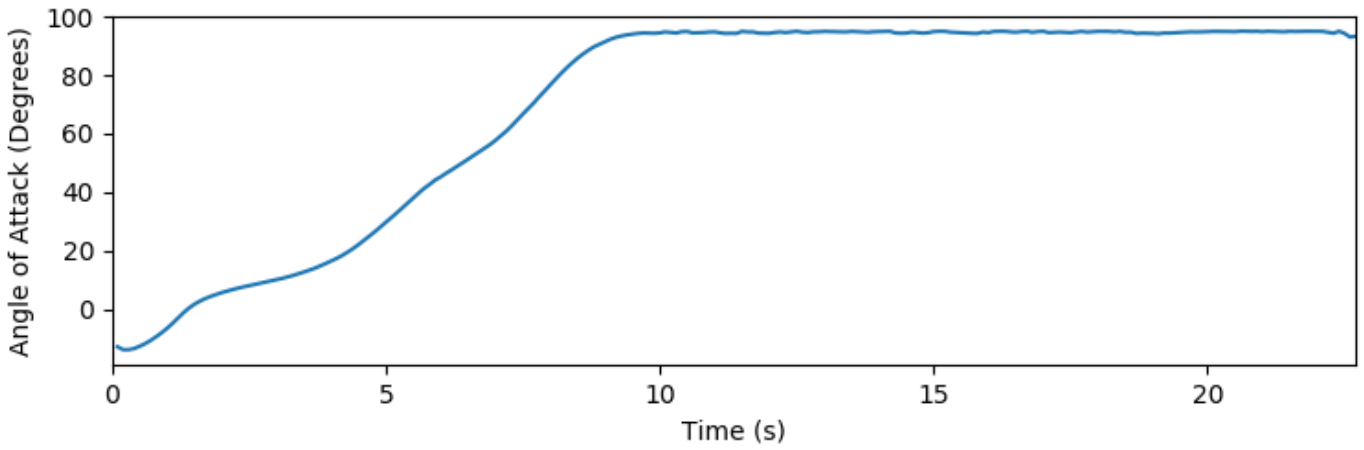


Figure 8.13: Angle of attack of the kite during a non-nominal descend.

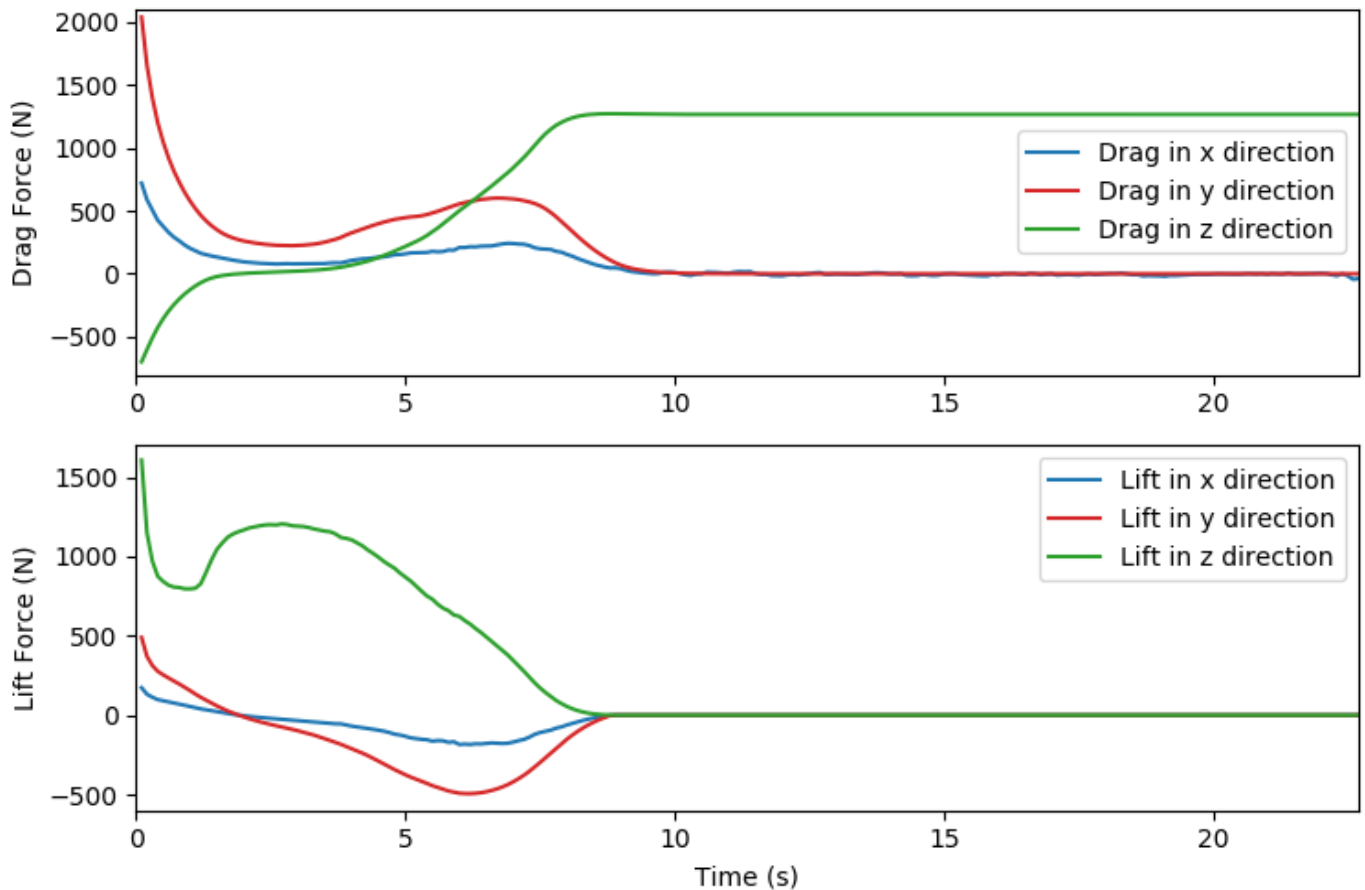


Figure 8.14: Lift force and drag force of the kite during a non-nominal descend.

8.4 Non-nominal Descend Model Validation

In this section the non-nominal descend model is validated as far as possible. It is difficult to validate the non-nominal descend model because the model is a Monte Carlo simulation with random inputs. For example, the wind input is constantly randomly generated during the simulation with the Dryden filter. Furthermore, the design of the system is slightly different since the last tether failure in may 2019. However, it is interesting to compare the output of this tether failure event with the results depicted in section 8.3.

The flight data of the tether failure in may 2019 is depicted in Figure 8.15. In Figure 8.15 the kite velocities, height, and distance from the ground station are depicted. In this design the maximum radial distance was higher than the current considered design. However, it is still interesting to compare the glide ratio because the kite design is still similar. The conditions of the tether failure in may 2019 are similar as in section 8.3. In section 8.3 the wind velocity is 7m/s, during the tether failure in may 2019 the wind velocity was also around 7 m/s.

The glide ratio during the tether failure of may 2019 was 1.1, the kite crashed to the ground 440m horizontally away from the tether failure point. The tether failed at a height of 400m. In the simulation of section 8.3 the horizontal distance between the tether failure point and the crash point is 135m. The tether failure point is at a height of 86.5m in the simulation of section 8.3. This results in a glide ratio of around 1.55. Therefore, it is concluded that the glide ratio in the model is higher than the tether failure in may 2019. However, the numbers are in the same order. Furthermore, the Monte Carlo simulation has random inputs, as earlier mentioned. A higher glide ratio results in higher third-party risk, because more crashes will end up outside the operational

zone, the circle of 400m around the ground station. Therefore, the results of the model are more on the safe side based on this validation point.

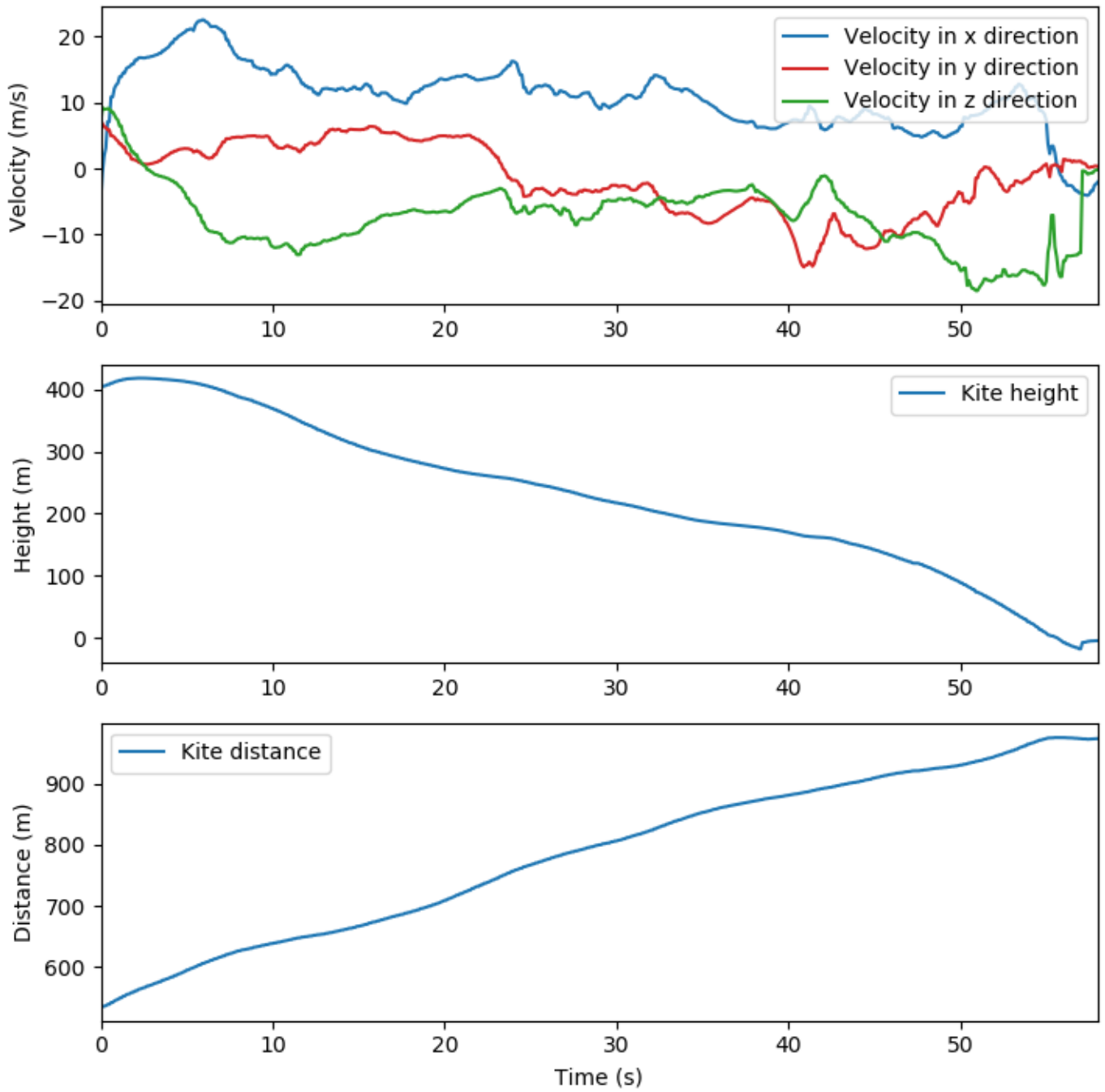


Figure 8.15: Flight data of the tether failure in may 2019.

8.5 Wind Turbulence Model Verification

In this section the wind turbulence model is verified. This is performed by first observing the figures from section 8.3. Next, the wind turbulence model is verified by comparing the white noise with the turbulence magnitude. Lastly, the histogram of the white noise and turbulence magnitude is verified.

Firstly, in Figure 8.11, Figure 8.12, Figure 8.13, and Figure 8.14 fluctuation is observed. For example, in Figure 8.13 a clear fluctuation of the angle of attack is observed. Also in Figure 8.14 a not constant force is observed after an equilibrium is found. It is clearly observed that the drag force in the x direction still fluctuates after 10 seconds, when the previously mentioned steady situation is met. This is due to the wind gust simulation model.

Secondly, in Figure 8.16 and Figure 8.17 the generated discrete random white noise signal is plotted together with the turbulence magnitude obtained by Equation 7.47. The input values for Equation 7.47 are depicted in Table 8.2. In Figure 8.15 and Figure 8.16 it is clearly observed that the Dryden filter follows the white noise signal. Furthermore, it is observed that the turbulence magnitude gradually fluctuates both in the x and y direction. Too many sudden wind velocity changes would be unrealistic. However, this does not happen.

Lastly, in Figure 8.18 a histogram of the turbulence magnitude is depicted with 1 million samples. In Figure 8.19 a histogram of the white noise signal is depicted with 1 million samples. The variance of the white noise signal is measured to be 1.0. The variance of the turbulence magnitude is measured to be 10.0. The variance of the white noise signal is logic since this is also the input value. The variance of the turbulence magnitude is also logic by observing Equation 7.47 and the input values in Table 8.2. All in all, it is concluded that the wind turbulence model is verified and performs as expected.

Table 8.2: Input values for the wind turbulence model verification.

Description	Variable	Value
Sample Period	T_S	0.2 s
Time Interval	t_ℓ	[0 s, 200 s]
Wind Velocity in x Direction	v_{wind_ref, t_ℓ}^x	7 m/s
Wind Velocity in y Direction	v_{wind_ref, t_ℓ}^y	7 m/s
Height	z	100 m

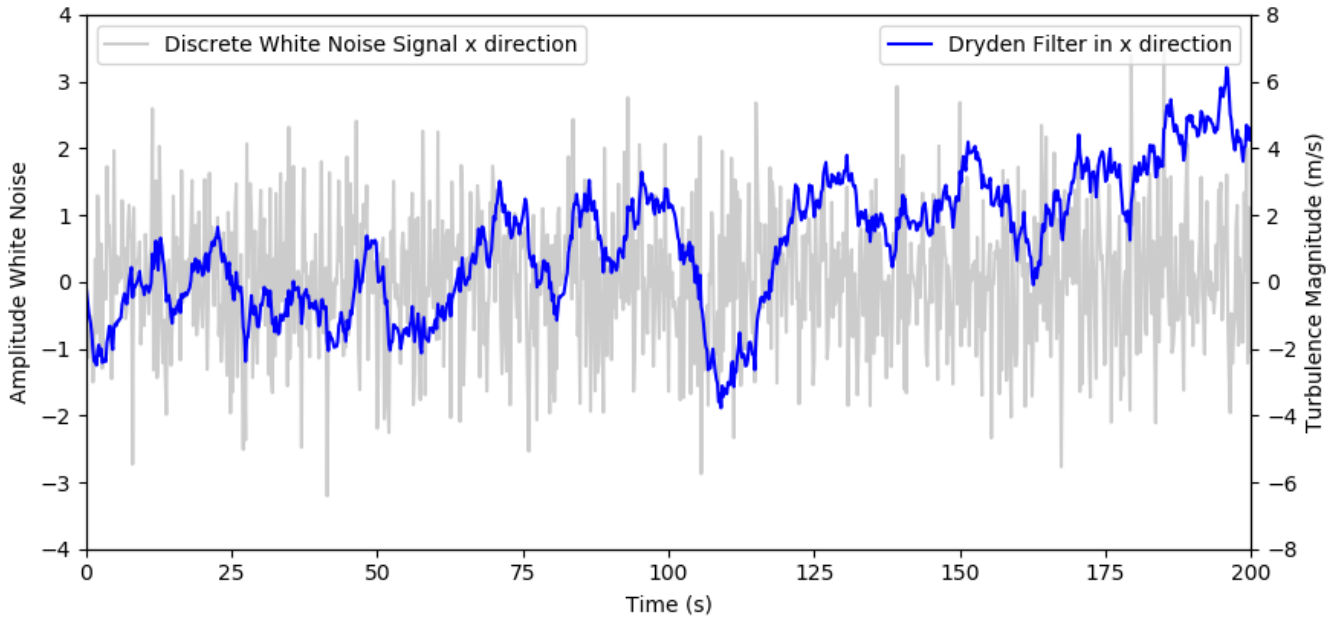


Figure 8.16: Turbulence sample in the x direction and its white noise with input values from Table 8.2.

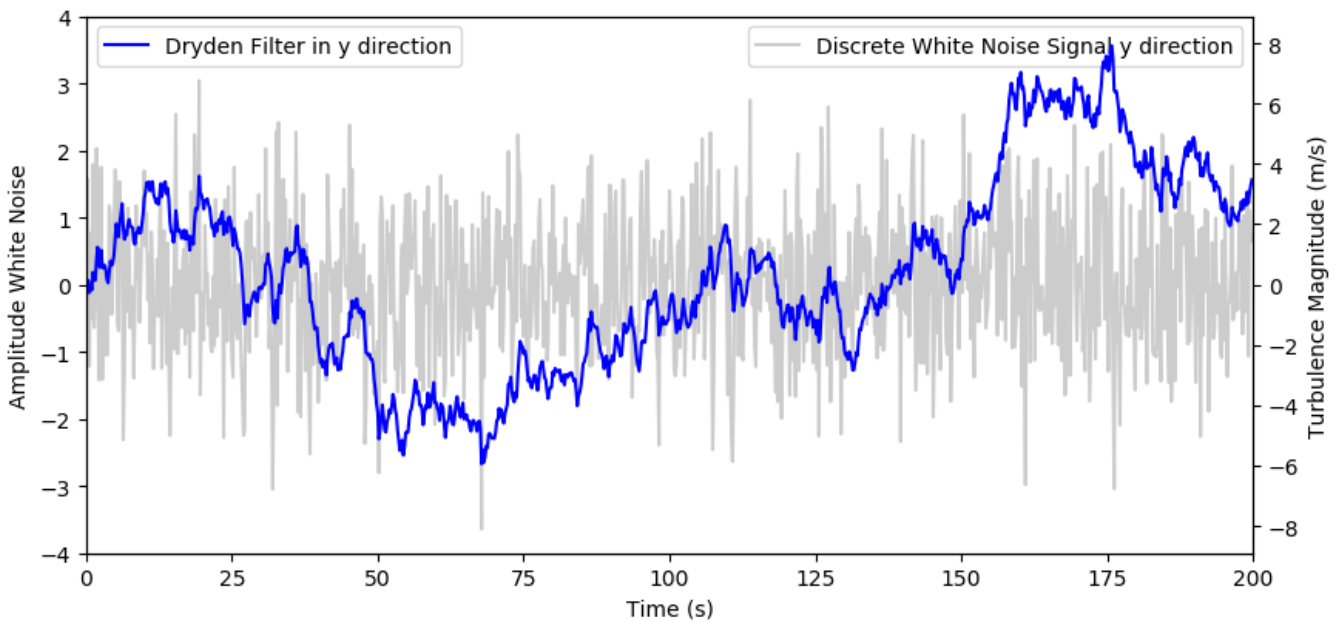


Figure 8.17: Turbulence sample in the y direction and its white noise with input values from Table 8.2.

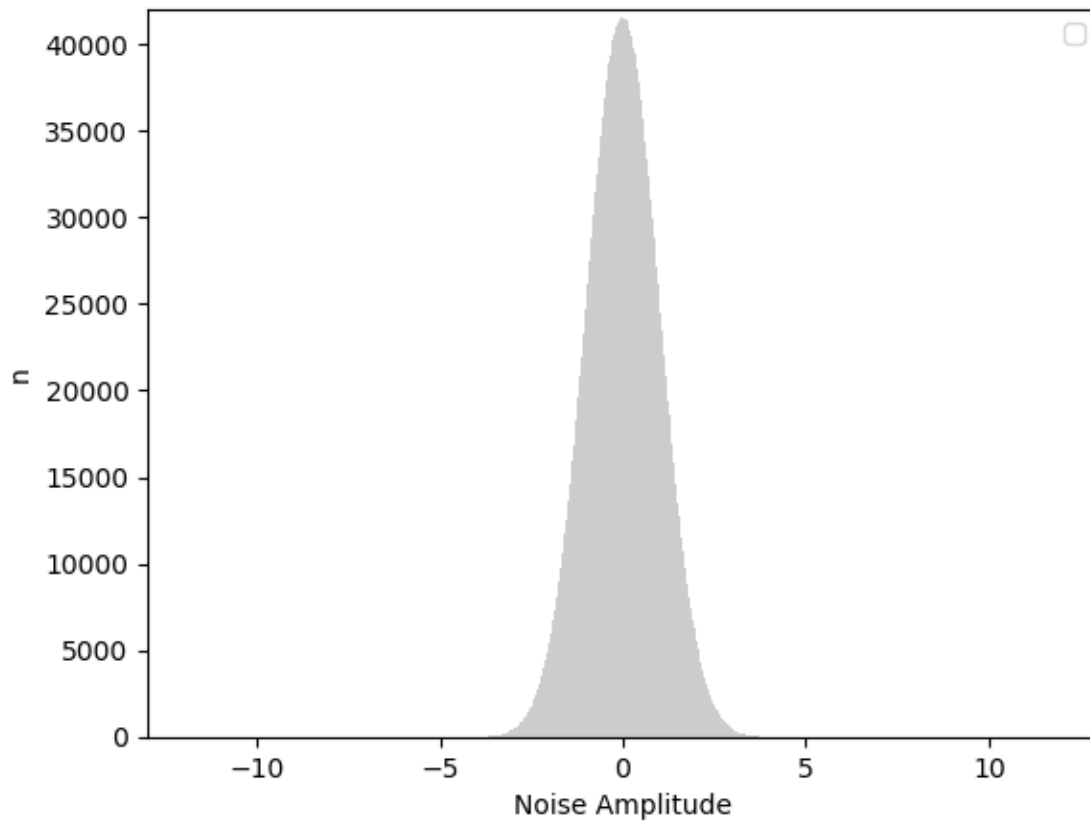


Figure 8.18: Histogram of discrete white noise with a total of 1 million samples.

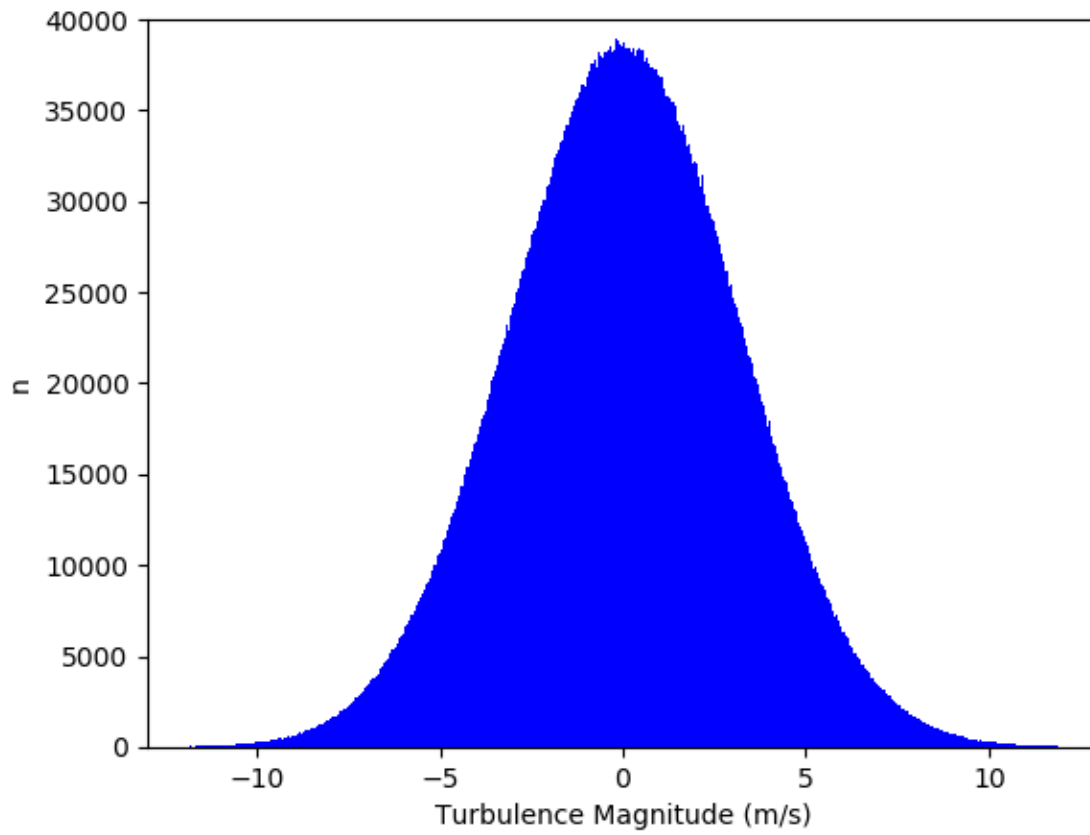


Figure 8.19: Histogram of turbulence magnitude with a total of 1 million samples.

9 Simulation Results and Sensitivity

Analysis

In chapter 8 the model is verified and validated. It is concluded that the model behaves as expected. Therefore, in this chapter, values are identified for every parameter of the model. Furthermore, the results, sensitivity analysis, and uncertainty analysis are discussed in this chapter. Therefore, this chapter consists of seven parts. Firstly, in section 9.1 values are introduced for the model parameters of chapter 7. Furthermore, for every parameter it is assessed if a sensitivity analysis is needed. Secondly, in section 9.2 the individual risk results are depicted. Next, in section 9.3 the collective ground risk per flight hour results are depicted. Subsequently, in section 9.4 the collective ground risk per year results are depicted. In section 9.5 the sensitivity analysis is performed. In section 9.6 the uncertain parameters are evaluated. Lastly, in section 9.7 all the results are discussed.

9.1 Parameter Values and Sensitivity Judgement

In this section the values of the model parameters of chapter 7 are introduced. Therefore, the assessment steps of the model are discussed. Steps that do not contain new parameters are not discussed. All the computational parameters are introduced in Table 9.1. All the physical parameters are depicted in Table 9.2.

Table 9.1: Computational parameters used in the simulation.

Parameter	Description	Value
N	Nominal Flight Paths	1800
$ \Delta v_w $	Wind Velocity Grid Step	2 m/s
Δv_w^{hdg}	Wind Heading Grid Step	1°
Δt	Time Step	0.1 s
K_i	Number of Runs of Non-nominal Descend Model	$ T_i^{nom} $
G_j	Grid Cell Dimensions	10 m x 10 m

Step 1

In step 1 the following physical parameters are introduced, depicted in Table 9.2: the drag coefficient C_D , lift coefficient C_L , scale height for air density H_P , maximum radial distance r_{max} , minimum radial distance r_{min} , projected surface area S , total flight hours T_{Total} , minimum wind velocity v_w^{min} , maximum wind velocity v_w^{max} , roughness z_0 , elevation β , and the air density at the ground ρ_0 . In step 1 the number of nominal flight paths N , the wind velocity grid step $|\Delta v_w|$, and the wind heading grid step Δv_w^{hdg} are the introduced computational parameters. Therefore, the wind sampling error ε_{grid}^v of step 3 is also introduced.

Firstly, the lift and drag coefficient values for different angles of attack are depicted in Table 9.3 and Figure 9.3. These values are obtained by Oehler and Schmehl (2019). However, it is observed that the coefficients vary a lot and are unpredictable. A sensitivity analysis is performed on both coefficients because the relation between third-party risk and the coefficients is non-linear. This sensitivity analysis is performed in section 9.5.

Secondly, the scale height for air density is identified in Table 9.2 by Johnson (2019). This is a commonly used constant. The uncertainty of the scale height for air density is negligible. Therefore, no sensitivity analysis is needed on this parameter. Next, the projected surface area, minimum radial distance, and maximum radial distance is obtained from the Kitepower expert. These are fixed parameters during the operations. This results in a negligible uncertainty. Therefore, a sensitivity analysis is not needed on these parameters.

Subsequently, according to the Kitepower expert, the operational hours are around 90% of the hours that wind conditions allow the kite to fly. The uncertainty of this value is significant because this is a rough estimation. However, no sensitivity analysis is performed on the operational hours because of its linear nature, instead the uncertainty is evaluated in section 9.6. The wind velocity in which the kite is currently safe to fly is between the 2 m/s and 12 m/s, according to the Kitepower expert. These limits are currently used in the operation. Therefore, the uncertainty of these limits is negligible and no sensitivity analysis is needed. By using the data from KNMI (2021) it was obtained that during 82.48% of the time the wind velocity is within the operational limits in Marknesse. The wind rose of Marknesse is depicted in Figure 9.1. Marknesse is the reference wind station for Rutten. The 82.48% availability of safe wind conditions result in 6502.7 operational hours per year if the kite operates 90% of the time.

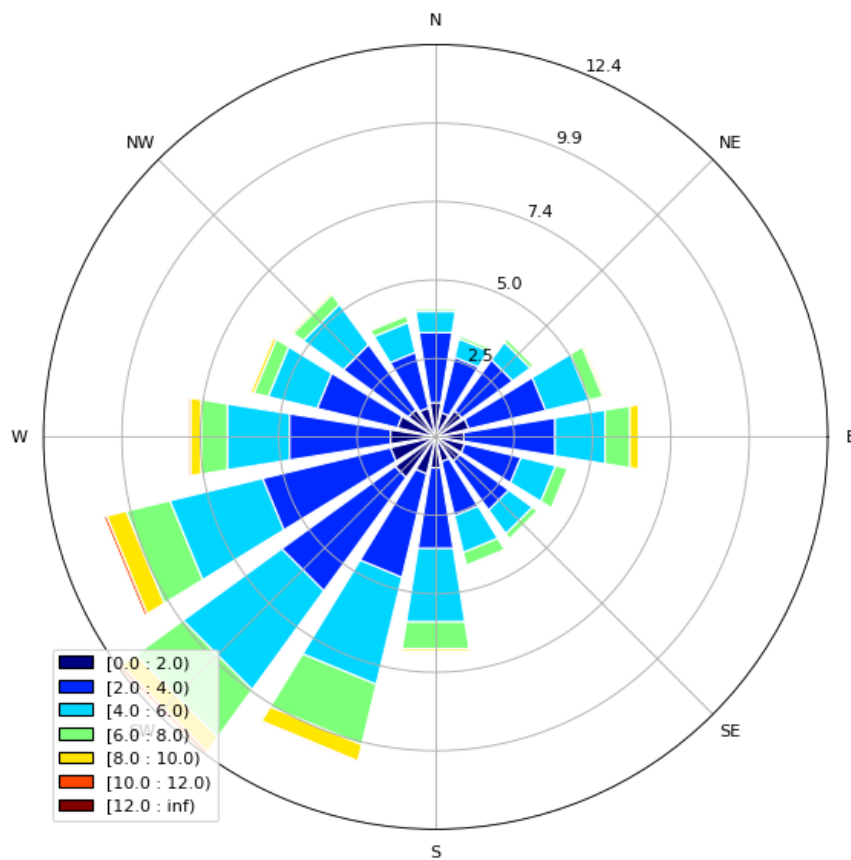


Figure 9.1: Wind rose of the KNMI station Marknesse.

Next, the number of nominal flight paths, the wind velocity grid step, the wind heading grid step, and the wind sampling error are identified to be able to model the flightpaths. The wind velocity grid step is set at 2 m/s and the wind heading grid step at 1°. This is identified by observing the accuracy of the results. It is observed that the results do not significantly change with a smaller wind heading grid step. There are 1800 nominal flight paths due to this grid size. A smaller wind velocity grid step results in a higher number of nominal flight paths. This results in a too long computational time. The wind velocity grid step results in a wind sampling error with a nearly uniform distribution of $U\left(-1\frac{m}{s}, 1\frac{m}{s}\right)$. However, in this thesis the wind sampling error is set at 0.0m/s due to the computational time. This means that all the wind conditions in a grid cell are modelled as the average wind velocity of that grid cell in section 9.2 until section 9.4. In section 9.5 a sensitivity analysis is performed on the wind sampling error to quantify the mismatch in third-party risk caused by the assumption that the wind sampling error is 0.0m/s.

The roughness is set at 0.005 taking into account Table 7.1, the landscape of Rutten, and Faggiani (2014) his analysis. The uncertainty of the roughness is negligible as both Johnson (2019) and Faggiani (2014) already verified and validated their models. Next, the elevation is obtained by operational data from the Kitepower expert. Again, the uncertainty is negligible due to the available data. Therefore, also no sensitivity analysis is needed on this parameter. The air density at the ground is a constant widely used. Johnson (2019) also used this as the air density at the ground. However, the air density at the ground is varying a lot due to local weather conditions. The uncertainty is still relatively small. Therefore, no sensitivity analysis is needed on the air density at the ground.

Step 2

The only parameter in step 2 is the tether failure rate $\lambda_{i,tether}$. This parameter is a worst case assumption from the Kitepower expert. The worst case assumption is that the kite crashes maximum ones a year. Therefore, to obtain the tether failure rate, one is divided by the total operational hours per year. The uncertainty of this value is significant because it is an assumption. No sensitivity analysis is performed because of its linear nature, instead the uncertainty is evaluated in section 9.6.

Step 3

Step 3 is the non-nominal descend model. Seven new physical parameters are needed for this step next to the already identified parameters in step 1 and step 2. Namely, the KCU mass m_{KCU} , the kite mass m_{Kite} , tether density ρ_{tether} , reference pitch angle θ_{Kite,t_e} , standard deviation flight path in the x direction σ_S^x , standard deviation flight path in the y direction σ_S^y , and the standard deviation flight path in the z direction σ_S^z . Furthermore, in terms of computational parameters the number of runs of the non-nominal descend model K_i and the time step of the simulation Δt are identified in Table 9.1.

The time step is of importance for step 1 and step 3 since in both models the time step is used to update the state variables of the kite. The time step is established by trial and error until the result did not deviate anymore. Furthermore, the computational time is taken into account. The time step is depicted in Table 9.1. The number of runs is typically the duration of the nominal path according to Blom et al (2020). This value is also verified by checking if the results did not deviate anymore.

The mass of the components is an important factor in the non-nominal descend model. The mass of the KCU and kite are obtained from the Kitepower expert. These values are fixed and the uncertainty is negligible. Therefore, no sensitivity analysis is needed on these masses. Next, the tether density is a parameter in the non-nominal descend model. This value is obtained from

Johnson (2019) and from the product characteristics. Therefore, also the uncertainty of the tether density is negligible and no sensitivity analysis is needed.

Subsequently, the reference pitch angle is set at 5° by the Kitepower expert. Therefore, the uncertainty is negligible and no sensitivity is needed.

Lastly, the standard deviation of the nominal flight path in the x , y , and z direction are set. These values are obtained from the validation data from Johnson (2019). Therefore, the uncertainty is small and no sensitivity is needed.

Step 4

In step 4 the grid size G_j is set. The grid is set at a size of 10 by 10 meters. The grid size is set at the same value as Vettorato (2021). Furthermore, by trial and error the grid size was changed. However, grid cells of 10 by 10 meters are the optimal size due to the computational time.

Step 5

In step 5 the mid-point value a and standard deviation b are the only parameters that are not identified yet. The mid-point value a is set at $101.6J$ and the standard deviation b at 0.538 . These values were assessed by Feinstein et al. (1968). Therefore, these values have a negligible uncertainty. No sensitivity analysis is needed on the mid-point value and the standard deviation.

Step 6

For step 6 only the crash impact area for the kite $|A(i, e)_{Kite}|$ and KCU $|A(i, e)_{KCU}|$ are not identified yet. The crash impact area for the KCU and kite are obtained by the method of Ale and Piers (2000). This method is a crash impact area estimation method from the aviation industry. In this method a crash impact area of 0.25m^2 per kilogram is set. In step 5 the probability of fatality is obtained. It is observed that the probability of fatality for the kite is too high because only a part of the kite will hit the human. The mass of the kite is distributed over a large area which results in a lower kinetic impact energy. This results in a lower probability of fatality. Therefore, to compensate, the crash impact area of the kite is divided by a factor 10. The uncertainty of the crash impact area is significant due to this assumption. However, due to the linear nature with risk there is no sensitivity analysis performed, instead the uncertainty is evaluated in section 9.6.

Step 9

The population density map is needed in step 9 of the third-party risk model framework from Blom et al. (2020). The population density $\rho(y_j)$ is obtained by data from the CBS (2020), as mentioned before. The used data consists of polygons with data attached to every polygon, the population density is one of the data parameters. In this data it is found that there are three areas close to the ground station in Rutten, as depicted in Figure 9.2. The black point in Figure 9.2 is the location of the ground station. Firstly, the largest area is the lightest area with the lowest number per km^2 , namely 18 per km^2 , this is a rural area. Secondly, the industrial area is the smallest area with a population density of 225 per km^2 . Lastly, the centre of Rutten is the darkest area with a population density of 1902 km^2 .

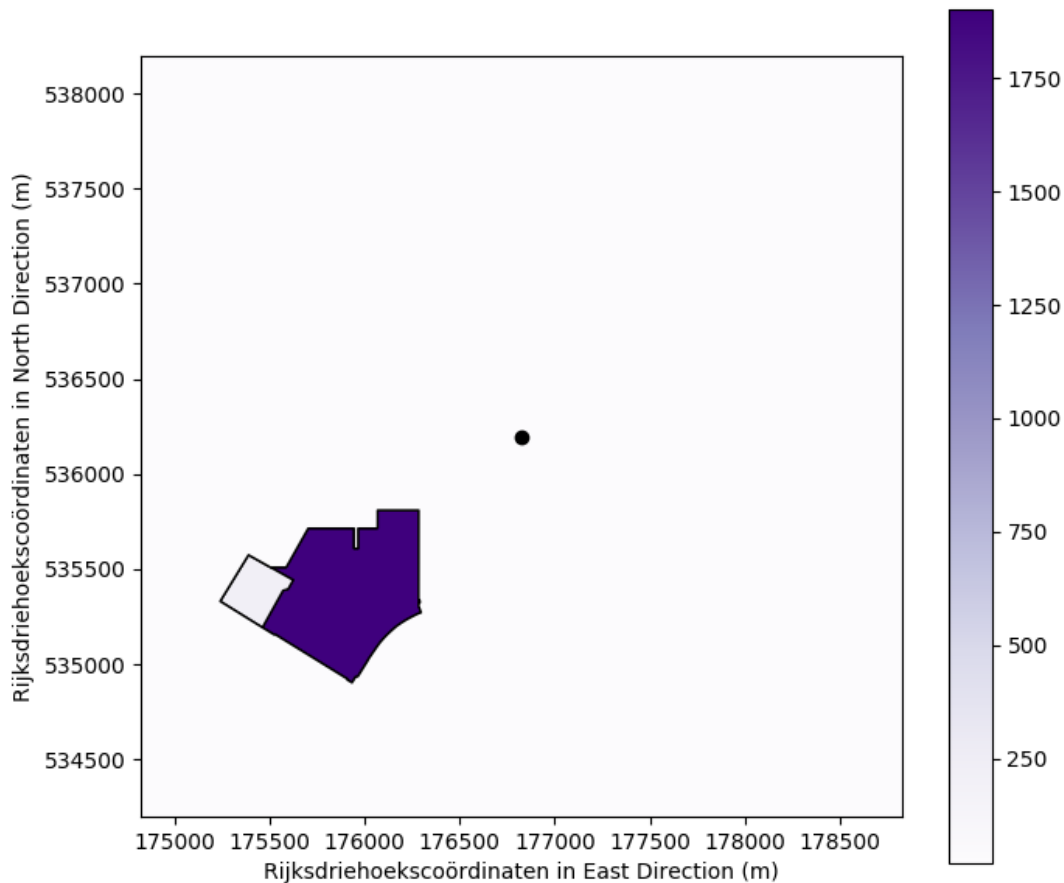


Figure 9.2: Population density map of the area around the ground station in Rutten, the Netherlands [CBS,2020].

Step 10

In step 10 the probability of shelter $\hat{P}(S_i, H)$ is identified. Melnyk et al. (2014) have identified that in the USA 7.6% of the time is spent outdoors, 5.5% in a vehicle, and 5.4% time spent in an office/factory. The area of Rutten is a rural area. Therefore, it is identified that relatively less time is spent in an office, but more outside. Furthermore, in the Netherlands the time spent in a vehicle is also more often on a cycle or a motorbike. Therefore, the time spent outdoors is identified to be 10%. This results in a shelter probability of 0.9 for every grid cell. However, the uncertainty of this value is significant. A sensitivity analysis is not performed due to its linear nature, instead the uncertainty is evaluated in section 9.6.

Table 9.2: Used parameter values with source and judgement of sensitivity.

Parameter	Description	Value	Source	Sensitivity	Uncertainty	Sensitivity Analysis Needed?
Step 1						
C_D	Drag Coefficient	In Table 9.3	[Oehler and Schmehl, 2019]	Non-Linear	Significant	Yes
C_L	Lift Coefficient	In Table 9.3	[Oehler and Schmehl, 2019]	Non-Linear	Significant	Yes
H_P	Scale Height for Air Density	8550 m	[Johnson, 2019]	Non-Linear	Negligible	No
r_{max}	Maximum Radial Distance	300 m	Kitepower Expert	Non-Linear	Negligible	No
r_{min}	Minimum Radial Distance	180 m	Kitepower Expert	Non-Linear	Negligible	No
S	Projected Surface Area	47 m ²	Kitepower Expert	Non-Linear	Negligible	No
T_{Total}	Total Flight Hours	6502.7 h	Kitepower Expert	Linear	Significant	No
v_w^{min}	Minimum Wind Velocity	2 m/s	Kitepower Expert	Non-Linear	Negligible	No
v_w^{max}	Maximum Wind Velocity	12 m/s	Kitepower Expert	Non-Linear	Negligible	No
z_0	Roughness	0.005	[Faggiani, 2014]	Non-Linear	Negligible	No
β	Elevation	25°	Kitepower Expert	Non-Linear	Negligible	No
ρ_0	Air Density at the Ground	1.225 kg/m ³	[Johnson, 2019]	Non-Linear	Small	No
Step 2						
$\lambda_{i,tether}$	Tether Failure Rate	$\frac{1}{T_{Total}}$ per hour	Kitepower Expert	Linear	Significant	No
Step 3						
m_{KCU}	KCU Mass	30 kg	Kitepower Expert	Non-Linear	Negligible	No
m_{Kite}	Kite Mass	80 kg	Kitepower Expert	Non-Linear	Negligible	No
$\varepsilon_{grid}^{v_{wind}}$	Wind Sampling Error	0.0 m/s	To Avoid Too High Computation Time	Non-Linear	$U\left(-1\frac{m}{s}, 1\frac{m}{s}\right)$	Yes
θ_{Kite, t_e}	Reference Pitch Angle	5°	Kitepower Expert	Non-Linear	Negligible	No
ρ_{tether}	Tether Density	0.000618 kg/m ³	[Johnson, 2019]	Non-Linear	Negligible	No

σ_S^x	Standard Deviation Flight Path in x Direction	10 m	[Johnson, 2019]	Non-Linear	Small	No
σ_S^y	Standard Deviation Flight Path in y Direction	10 m	[Johnson, 2019]	Non-Linear	Small	No
σ_S^z	Standard Deviation Flight Path in z Direction	10 m	[Johnson, 2019]	Non-Linear	Small	No
Step 5						
a	Mid-point Value	101.6 J	[Feinstein et al., 1968]	Non-Linear	Negligible	No
b	Standard deviation	0.538	[Feinstein et al., 1968]	Non-Linear	Negligible	No
Step 6						
$ A(i, e)_{Kite} $	Crash Impact Area Kite	2 m ²	[Ale and Piers, 2000]	Linear	Significant	No
$ A(i, e)_{KCU} $	Crash Impact Area KCU	7.5 m ²	[Ale and Piers, 2000]	Linear	Significant	No
Step 9						
$\rho(y_j)$	Population Density	18, 225, or 1902 1/km ²	[CBS, 2020]	Linear	Negligible	No
Step 10						
$\widehat{P}(S i, H)$	Probability of Shelter Protection	0.9	[Melnik et al., 2014], [Blom et al., 2020]	Linear	Significant	No

Table 9.3: The lift and drag coefficients for different angles of attack.

AoA(α)	-90°	-20°	-10°	0°	5°	10°	20°	45°	90°
C_L	0.0	0.0	0.15	0.35	0.6	1.0	1.3	0.9	0.0
C_D	2.0	0.13	0.15	0.15	0.15	0.2	0.5	0.85	2.0

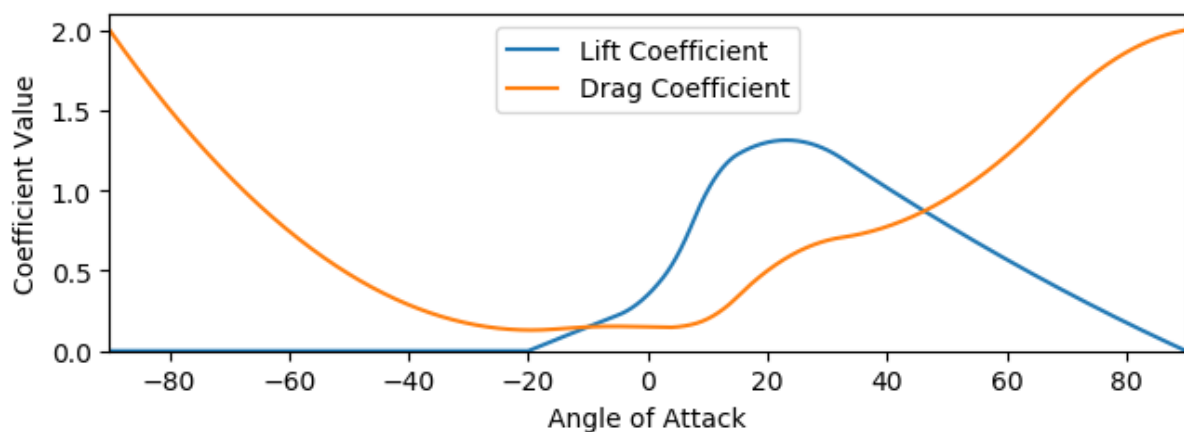


Figure 9.3: The lift and drag coefficients for different angles of attack plotted in one graph.

9.2 Simulation Results Individual Risk

In this section the simulation results with respect to the individual risk are depicted and discussed. The individual risk is identified by the model in step 7, of section 7.1, with the parameters identified in section 9.1. The individual risk per year is depicted in Figure 9.4 for the area around the Rutten installation. The ground station is located at the origin of the graph, the north is upwards, and the east is right. The black circle shows the border of the operational zone, the radius of 400m. Within this radius also other events than a tether failure can occur. Therefore, only the individual risk outside this circle is the total individual risk. A discrete individual risk map is depicted in Figure 9.5 to see the exact borders between the different regulation limits. In Figure 9.5 the green pixels depict an individual risk per year lower than 10^{-6} , the orange pixels depict an individual risk per year between 10^{-6} and 10^{-5} , and the red pixels depict an individual risk higher than 10^{-5} . The maximum individual risk is identified to be 1.551×10^{-5} .

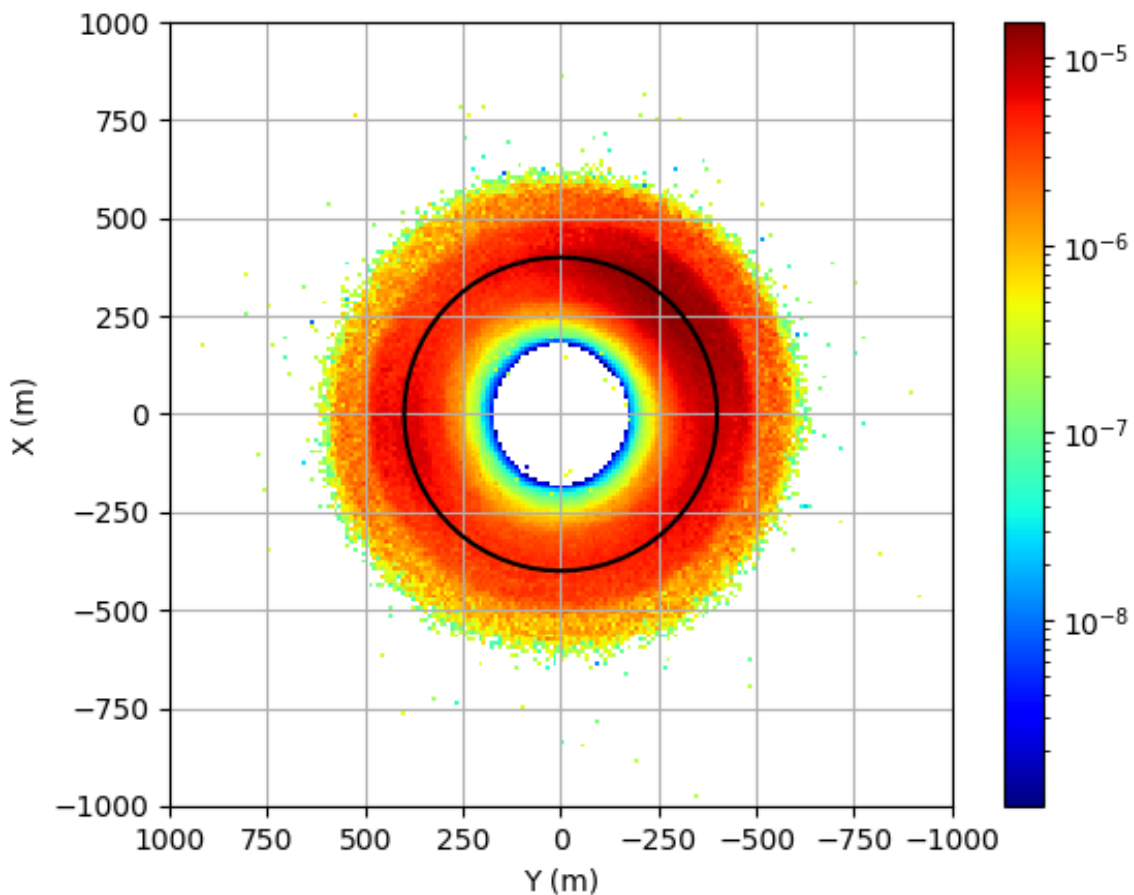


Figure 9.4: Individual risk per year for the area around Rutten.

The results, that are depicted in Figure 9.4 and Figure 9.5, show that the individual risk is above most of the individual risk regulations. In chapter 4 it is found that in most countries the individual risk per year is allowed to be maximal 10^{-6} per year for new objects. For already existing objects the limitation for individual risk is 10^{-5} per year. It is observed in Figure 9.5 that there is a large zone that exceeds the limitation for new objects, with an individual risk per year higher than 10^{-6} . Therefore, within a radius of 600m around the ground station no new housing development is allowed.

The limit for existing objects, a maximal individual risk of 10^{-5} per year, is also not completely met because the maximum individual risk is 1.551×10^{-5} . In Figure 9.5 the red contour depicts the area that does not comply with the maximum individual risk of 10^{-5} per year. Therefore, the operational zone should be enlarged to a radius of 500m in the dominant wind direction. All the housing within

the 10^{-5} contour should be demolished. In Figure 9.6 a satellite photo is depicted of the area around the test location of Rutten. The yellow pin is the location of the ground station, the yellow circle shows the radial distance of 700m. In Figure 9.6 it is observed that within this circle no housing is present. Therefore, no houses need to be demolished.

Next to the regulations, it is observed that the wind conditions have a strong correlation with the individual risk in Figure 9.4 and Figure 9.5. This is logic because the kite flies with the wind in the simulation. The wind direction is the main factor that influences the crash direction of the kite. The wind velocity influences the crash distance of the kite from the ground station. The higher the wind velocity the further the kite flies. Due to the commonly south west winds it is observed that the highest individual risk is north east of the ground station. Furthermore, due to the strong easterly winds there is also a higher individual risk observed west of the ground station, as depicted in Figure 9.4. Therefore, the individual risk heavily depends on the location of the ground station because the wind conditions differ per location.

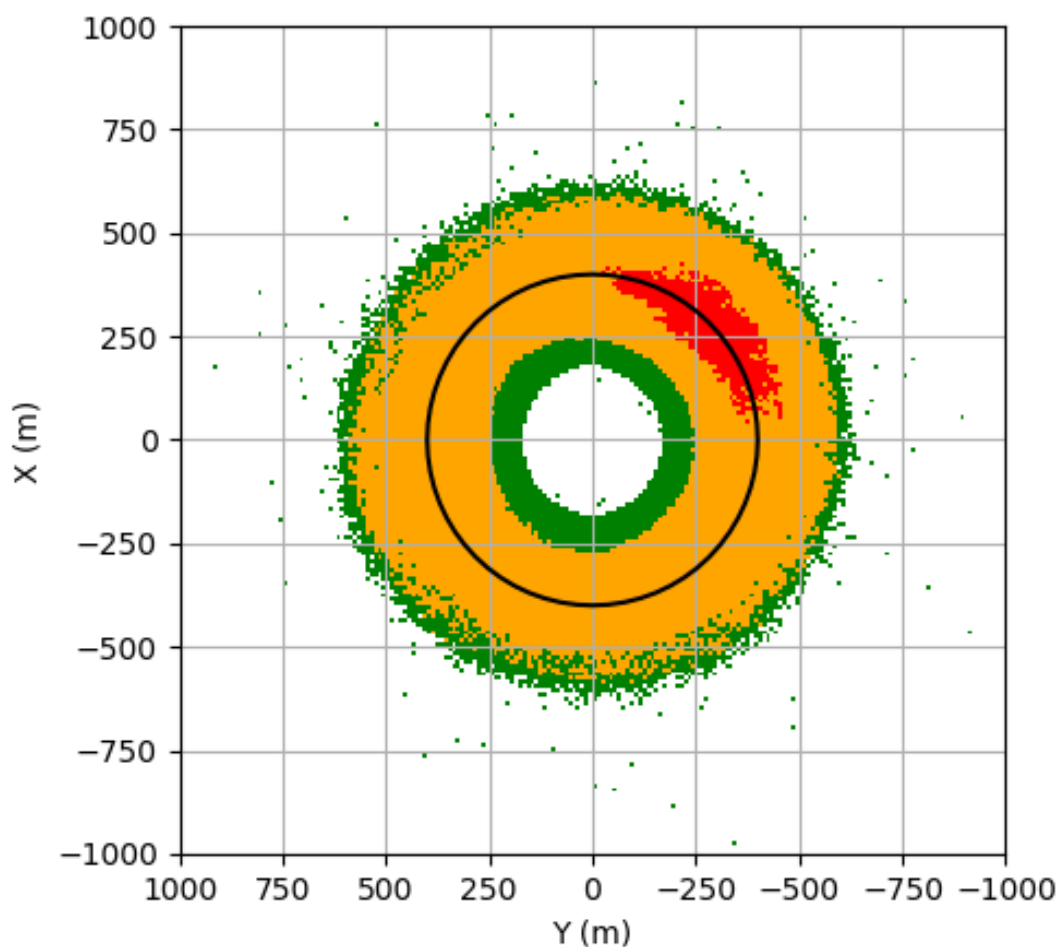


Figure 9.5: Individual risk per year at test location Rutten, green is $R_f < 10^{-6}$, orange is $10^{-6} < R_f < 10^{-5}$, and red is $R_f > 10^{-5}$.



Figure 9.6: The yellow pin is the location of the ground station at test location Rutten, the circle has a radius of 700m.

9.3 Simulation Results Collective Ground Risk per Flight Hour

In this section the simulation results with respect to the collective ground risk per flight hour are depicted and discussed. The collective ground risk per flight hour is identified by the model in step 12, previously described with the parameters identified in section 9.1. In Figure 9.7 a histogram of the collective ground risk per flight hour is depicted.

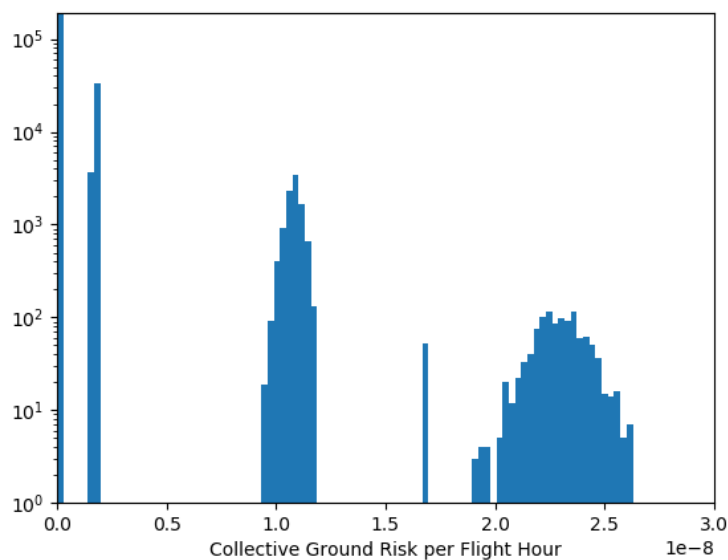


Figure 9.7: Histogram of the collective ground risk per flight hour.

Firstly, in Figure 9.7 it is observed that the maximum collective ground risk per flight hour is 2.8×10^{-8} fatalities. In chapter 7 it is found that currently a threshold of 10^{-6} fatal injuries is the regulation limit for UAS. Therefore, the maximum collective ground risk per flight hour of the system is lower than the regulations.

Secondly, in Figure 9.7 it is observed that there are five clusters with around the same collective ground risk per flight hour. These clusters exist due to the wind velocity grid steps in the model of chapter 7. The model consists of the wind velocity grid steps 3 m/s, 5 m/s, 7 m/s, 9 m/s, and 11 m/s. The collective ground risk per flight hour with a wind velocity of 3 m/s is negligible. Therefore, no graph is depicted with a wind velocity of 3 m/s. Next, in Figure 9.8 the collective ground risk per flight hour is depicted with a wind velocity of 5 m/s. On the x -axis the wind direction is depicted, on the y -axis the collective ground risk per flight hour. In Figure 9.9 the collective ground risk per flight hour is depicted with a wind velocity of 7 m/s. In Figure 9.10 the collective ground risk per flight hour is depicted with a wind velocity of 9 m/s. In Figure 9.11 the collective ground risk per flight hour is depicted with a wind velocity of 11 m/s. Lastly, in Figure 9.12 the collective ground risk per flight hour for every wind velocity grid step are plotted in one graph. The magnitude of the collective ground risk per flight hour for every wind velocity grid step is easily compared with Figure 9.12.

The first identified cluster in Figure 9.7 is a combination of the wind velocity grid steps 3 m/s and 5 m/s. The collective ground risk per flight hour with a wind velocity of 3 m/s is zero and with a wind velocity of 5 m/s is around 0.7×10^{-10} , as depicted in Figure 9.8. Therefore, both wind velocities fall in the first bin of the histogram depicted in Figure 9.7. The next cluster in Figure 9.7 has a collective ground risk per flight hour of around 1.8×10^{-9} . This cluster is the wind velocity of 7 m/s, as depicted in Figure 9.9. The next cluster in Figure 9.7 has a collective ground risk per flight hour of around 1.1×10^{-8} . This cluster is the wind velocity of 9 m/s, as depicted in Figure 9.10. The next cluster in Figure 9.7 has a collective ground risk per flight hour of around 1.7×10^{-8} . This cluster is the result of the spikes and gaps of the Monte Carlo simulation of the wind velocity of 9 m/s and 11 m/s, as observed in Figure 9.10, Figure 9.11, Figure 9.12. The last cluster in Figure 9.7 is the wind velocity of 11 m/s, as observed in Figure 9.11.

From the results in Figure 9.7 until Figure 9.12 it is observed that the collective ground risk per flight hour is independent of the wind direction. For all wind directions the collective ground risk per flight hour is the same if the wind velocity is constant. The reason for this is the constant population density around the installation. The town of Rutten, with a higher population density, is not reached by any of the simulations. Therefore, the wind direction has no contribution to the collective ground risk per flight hour. This should be analyzed again if the accuracy of the population density map in Rutten is improved. Furthermore, if the system is operated on other locations, with different population densities, the collective ground risk per flight hour can still be influenced.

Lastly, from the results in Figure 9.7 until Figure 9.12 it is also observed that the collective ground risk per flight hour highly depends on the wind velocity. The higher the wind velocity the higher the collective ground risk per flight hour because more crashes are outside the operational zone of 400m. The rise of the collective ground risk per flight hour decreases if higher velocities are present because most crashes are already outside the operational zone. The collective ground risk per flight hour only depends on the crash location in terms of population density because the probability of shelter is assumed constant at all locations. However, only the operational zone has an influence on the population density because the population density is constant outside the operational zone and zero within the operational zone.

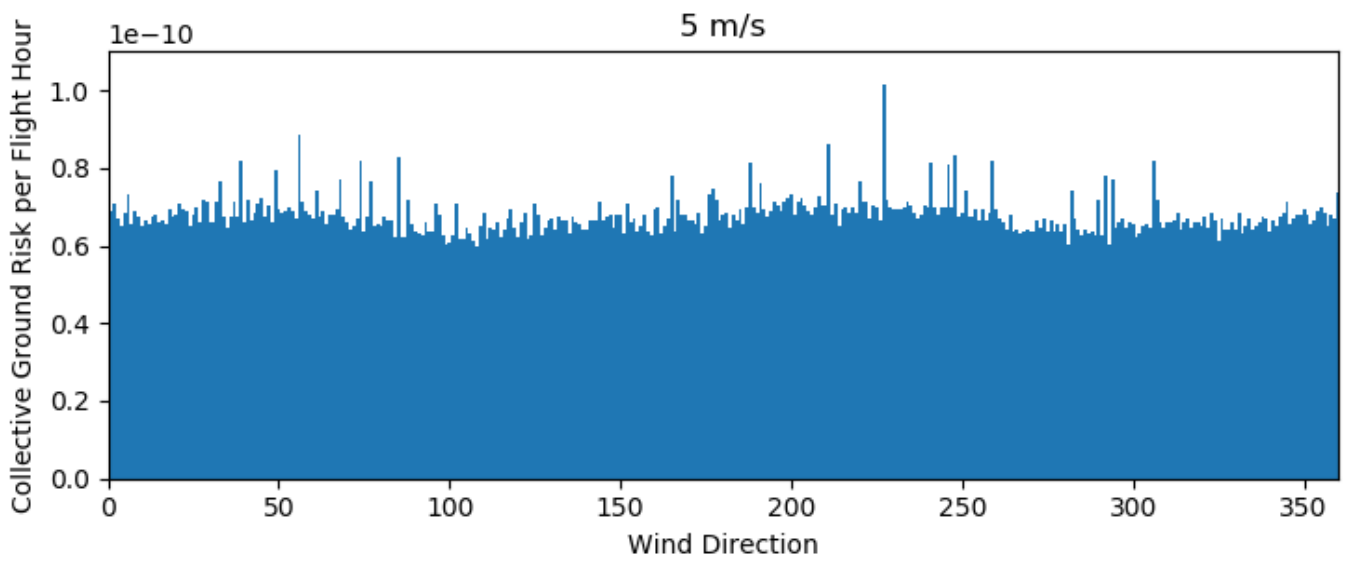


Figure 9.8: Collective ground risk per flight hour with a wind velocity of 5 m/s.

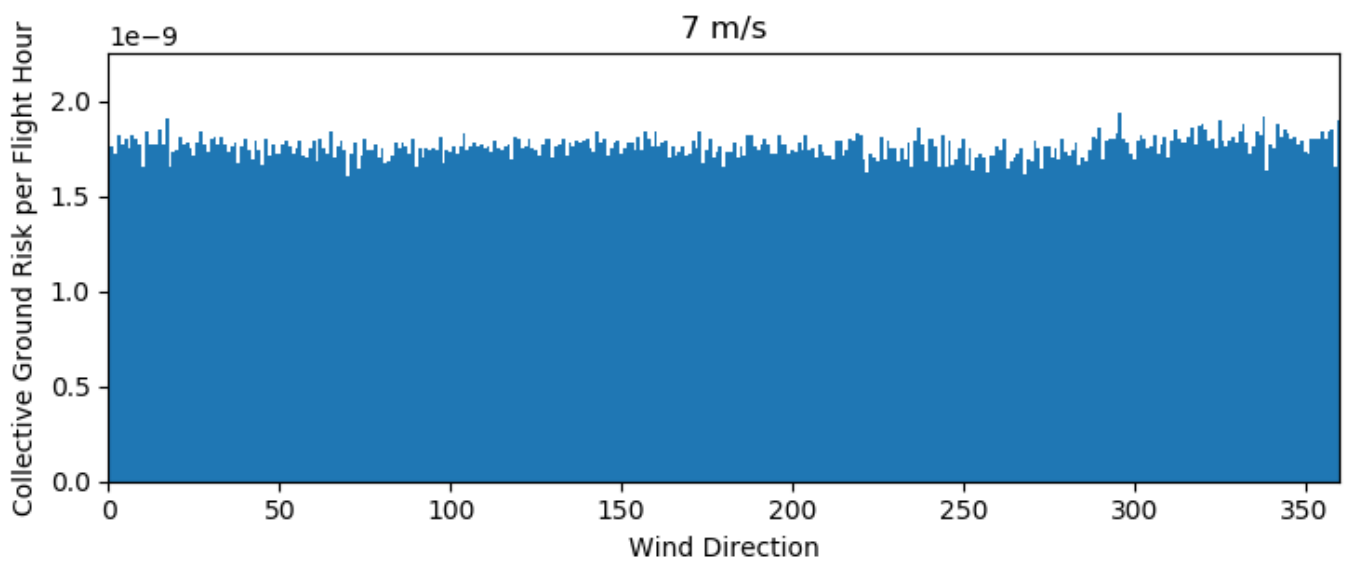


Figure 9.9: Collective ground risk per flight hour with a wind velocity of 7 m/s.

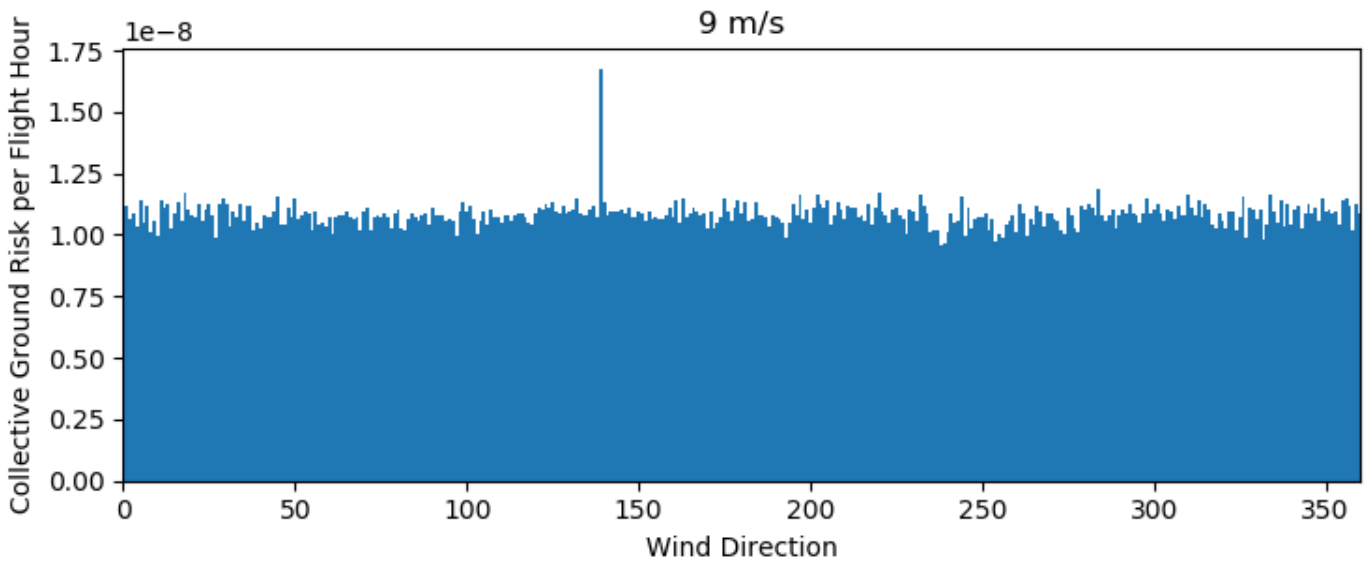


Figure 9.10: Collective ground risk per flight hour with a wind velocity of 9 m/s.

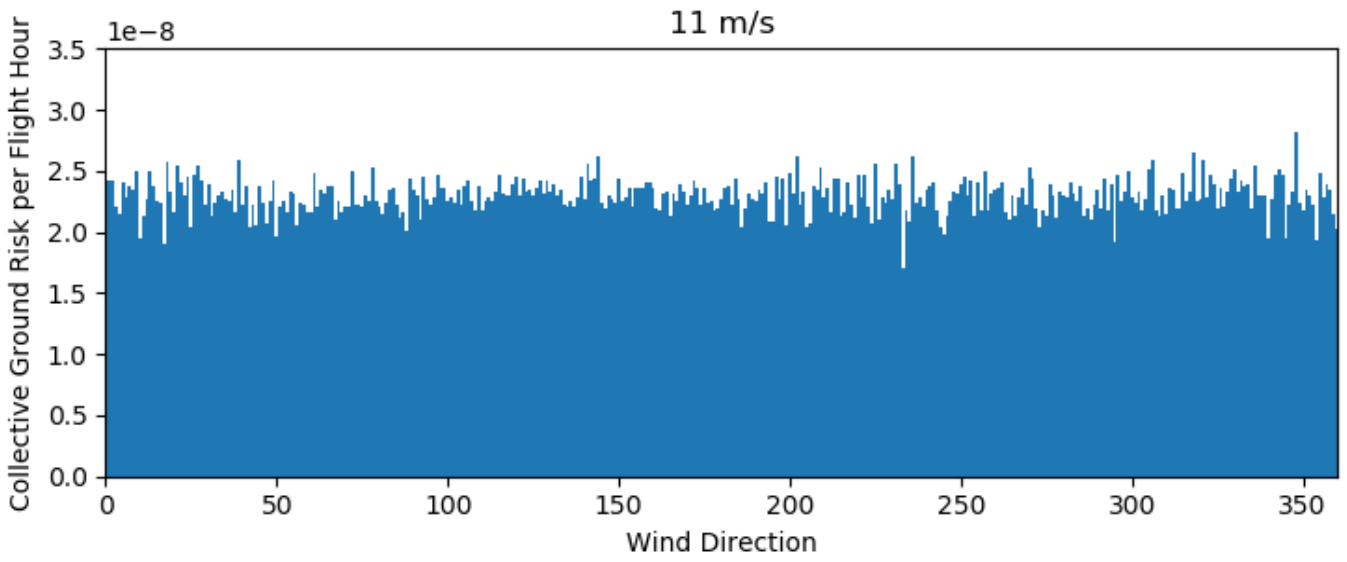


Figure 9.11: Collective ground risk per flight hour with a wind velocity of 11 m/s.

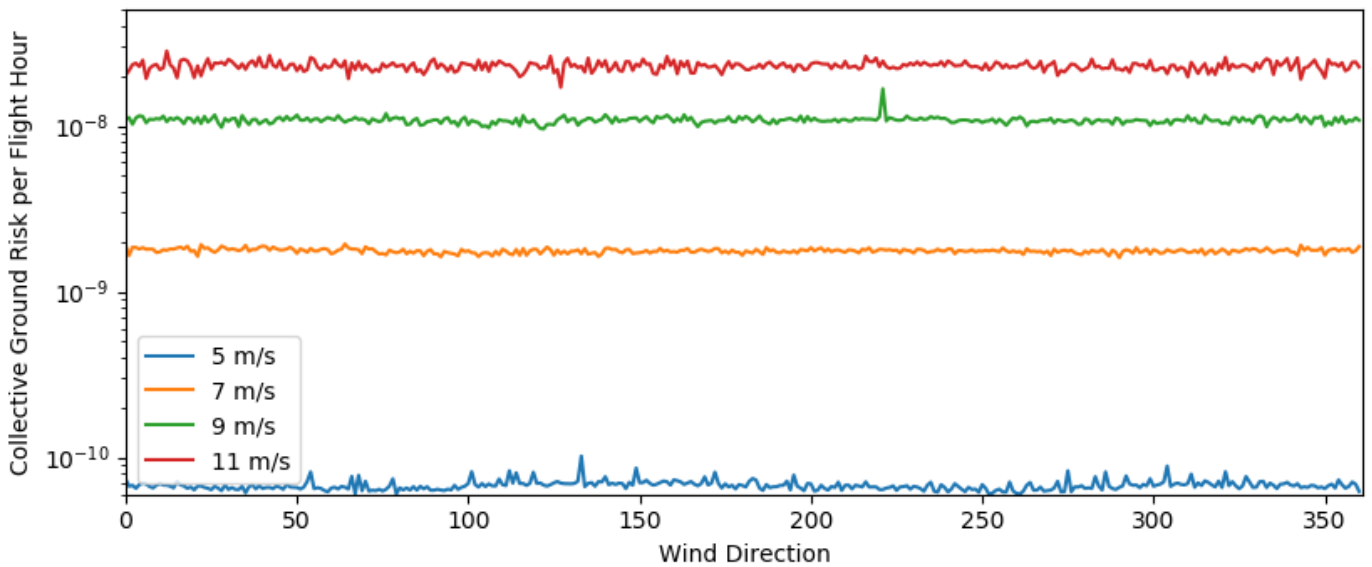


Figure 9.12: Overview of the collective ground risk per flight hour for the different wind velocities.

9.4 Simulation Results Collective Ground Risk per Year

In this section the simulation results for the collective ground risk per year are depicted and discussed. The collective ground risk per year is identified by the model in step 14, of section 7.1, with the parameters identified in section 9.1. The collective ground risk for the area around the test location in Rutten is $3.972732177 \times 10^{-6}$ per year, as depicted in Figure 9.13.

Equation 7.16 sets the regulations for collective ground risk by adapting the FN-curve regulations found in chapter 4 if a crash only leads to one fatality. In this thesis $\alpha=2$ and $C=10^{-3}$ are the assumed regulation constants. This results in a maximum collective ground risk of 1.6449×10^{-3} per year, according to the regulations. It is observed that the collective ground risk of the system is far below this value, as depicted in Figure 9.13. Therefore, the system is considered safe in terms of collective ground risk per year with the condition that a crash leads to maximum one fatality. During the results it is observed that the probability of fatality is very low for the kite. This due to the fact that the impact energy is spread over a large area. The probability of fatality of the KCU is higher and therefore the main driving factor. Based on these results it is observed that a crash only leads to maximum one fatality. Therefore, Equation 7.16 is assumed correct and the system is within the regulation limits in terms of collective ground risk per year.

The collective ground risk per year is highly influenced by the population density, the same as for the collective ground risk per flight hour. It is observed that the area around the test location in Rutten has a relatively low population density of only 18 per km^2 . This is one of the reasons that the collective ground risk per year is low. However, the system is still within the regulation limits if the population density around the system is a factor 100 higher, like the centre of the town Rutten. Therefore, the undetailed population density is not an important factor in terms of collective ground risk per year for the location in Rutten. However, the population density still has a large influence on the collective ground risk per year and should be investigated if the system is operated at other locations.

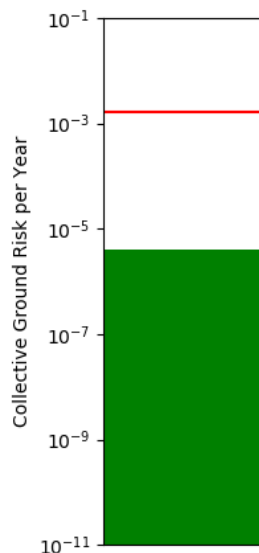


Figure 9.13: The collective ground risk per year of the system in green and the regulation limit in red.

9.5 Sensitivity Analysis

In this section the sensitivity analysis is performed. In section 9.1 it is identified that the sensitivity is unknown for the wind sampling error, lift coefficient, and the drag coefficient. Therefore, first a sensitivity analysis is performed on the wind sampling error. Secondly, a sensitivity analysis is performed on the lift coefficient and on the drag coefficient.

Wind Sampling Error

The sensitivity analysis on the wind sampling error is performed because in section 9.2 until section 9.4 the wind sampling error is set at 0.0m/s to limit the computational time. The actual wind sampling error has a uniform distribution of $U\left(-1\frac{m}{s}, 1\frac{m}{s}\right)$. Therefore, the maximum deviation is 1.0m/s or -1.0m/s. The higher the wind velocity the higher the third-party risk. Therefore, only the upper limit is assessed in this sensitivity analysis, a wind sampling error of 1.0m/s.

The individual risk with a wind sampling error of 0.0m/s is depicted in Figure 9.14 and Figure 9.15. The individual risk with a wind sampling error of 1.0m/s is depicted in Figure 9.16 and Figure 9.17. The red zone increases and the zone where individual risk is present increases if the wind sampling error changes from 0.0m/s to 1.0m/s, as depicted in Figure 9.15 and Figure 9.17. Therefore, the individual risk increases significantly if the wind sampling error changes from 0.0m/s to 1.0m/s. The operational zone should still be enlarged to a radius of 500m in the dominant wind direction. The size of this zone increase is increased with respect to the original findings.

The collective ground risk with a wind sampling error of 0.0m/s is depicted in Figure 9.18. The collective ground risk with a wind sampling error of 1.0m/s is depicted in Figure 9.19. The collective ground risk is increased significantly if the wind sampling error changes from 0.0 to 1.0, as depicted in Figure 9.18 and Figure 9.19. However, the collective ground risk is still below the threshold set by the regulators.

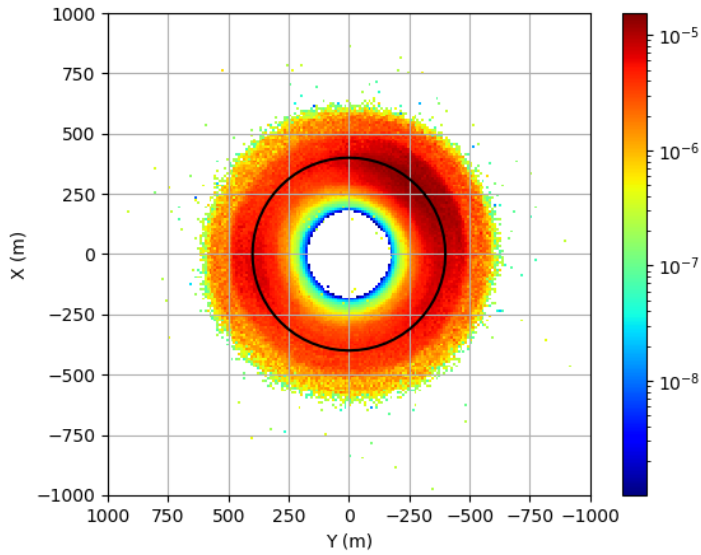


Figure 9.14: Individual risk per year for the area around Rutten with a wind sampling error of 0.0m/s.

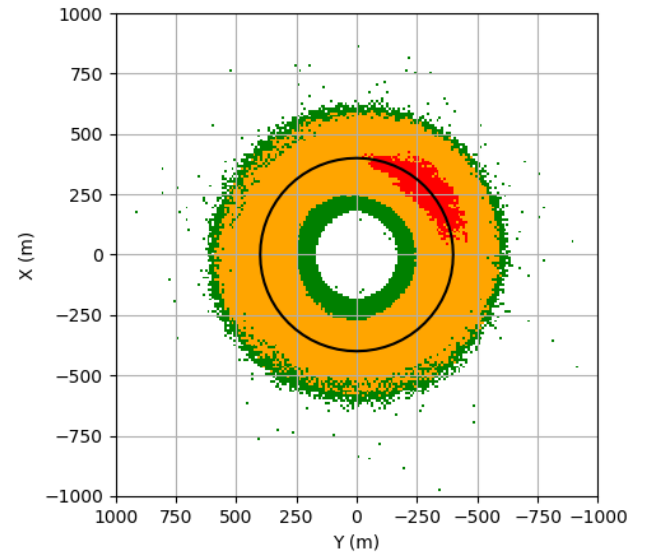


Figure 9.15: Discrete individual risk per year for the area around Rutten with a wind sampling error of 0.0m/s, green is $R_I < 10^{-6}$, orange is $10^{-6} < R_I < 10^{-5}$, and red is $R_I > 10^{-5}$.

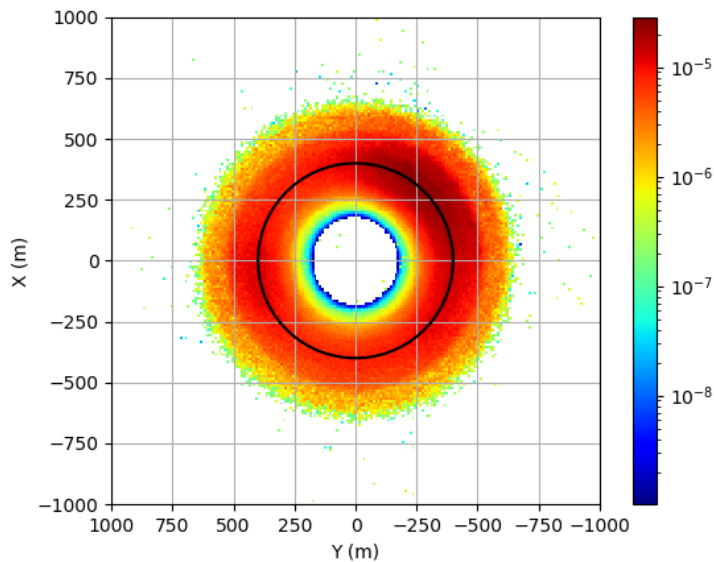


Figure 9.16: Individual risk per year for the area around Rutten with a wind sampling error of 1.0m/s.

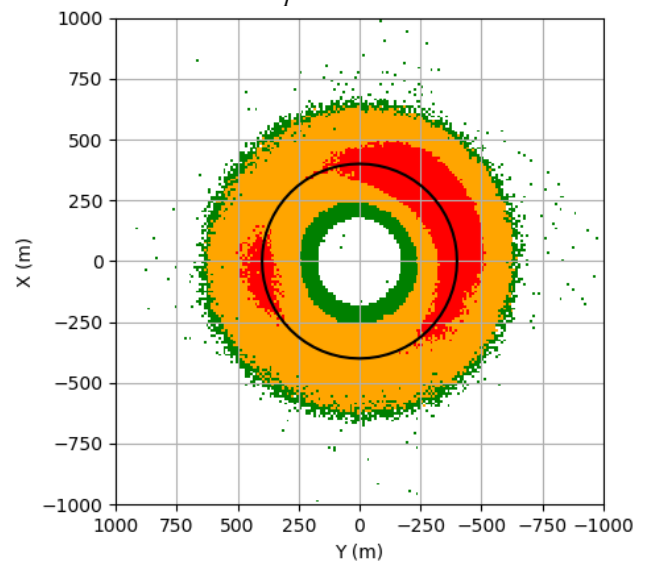


Figure 9.17: Discrete individual risk per year for the area around Rutten with a wind sampling error of 1.0m/s, green is $R_I < 10^{-6}$, orange is $10^{-6} < R_I < 10^{-5}$, and red is $R_I > 10^{-5}$.

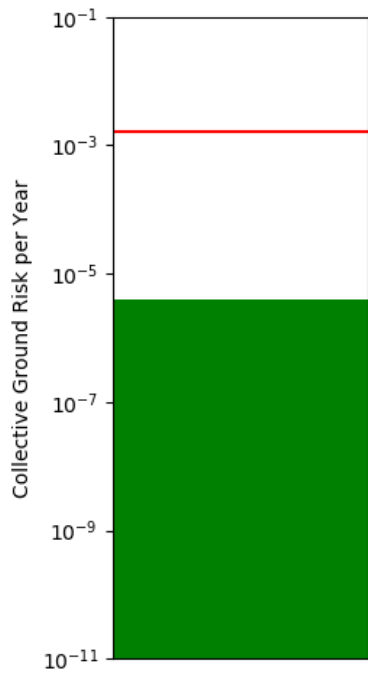


Figure 9.18: Collective ground risk per year for the area around Rutten with a wind sampling error of 0.0m/s.

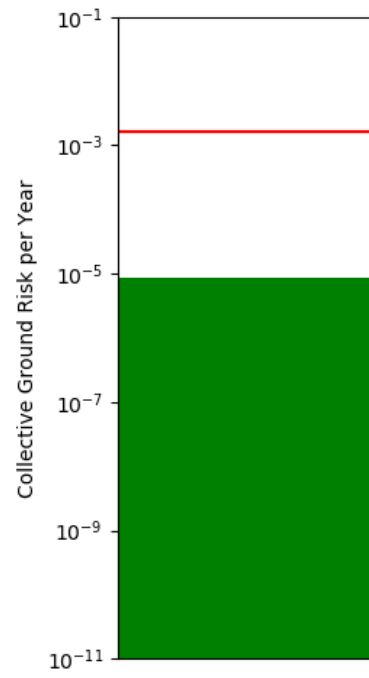


Figure 9.19: Collective ground risk per year for the area around Rutten with a wind sampling error of 1.0m/s.

Lift Coefficient

The sensitivity analysis on the lift coefficient consists of multiplying all the lift coefficients from Table 9.3 with a factor. This is performed for the factors 0.8, 0.9, 1.0, 1.1, and 1.2. These relatively small factors are chosen because the lift coefficient is from its origin a sensitive parameter. Furthermore, otherwise physical impossible situations are simulated, the lift force unrealistically high compared to the drag force.

In Figure 9.20 until Figure 9.29 the influence of the lift coefficient on the individual risk is depicted. It is observed that the individual risk does only slightly change by a decreasing lift coefficient. The individual risk concentrates a bit more on one place. The red zone increases while the green zone decreases, as depicted in Figure 9.21. The clarification of this observation is that in this situation the kite flies less far due to a smaller lift influence which results in a lower lift over drag ratio. This results in a higher maximum individual risk and less spread out individual risk.

If the lift coefficient is multiplied by a factor 1.1 the individual risk is spread slightly more. The red zone decreases but the green zone clearly grows a bit. However, it is observed that if the lift coefficient is multiplied by a factor 1.2 the individual risk drastically change. The red zone has disappeared. The orange and green zone increase drastically. A larger area is posed by individual risk with a higher lift coefficient. The largest increase is clearly between the factor 1.1 and 1.2. The clarification of this observation is that in this situation the kite flies further due to a larger lift influence. This results in a larger lift over drag ratio. This results in a lower maximum individual risk due to the lower concentration of crashes. However, there is at more locations individual risk present due to the longer distance flown.

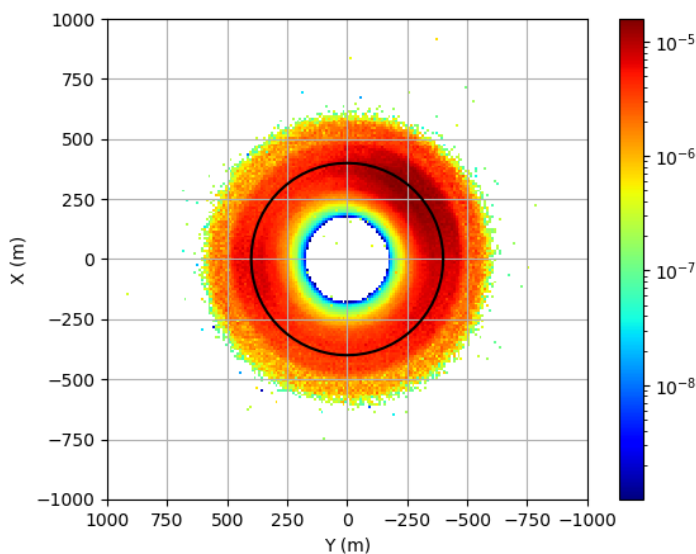


Figure 9.20: Individual risk per year for the area around Rutten with the lift coefficient multiplied by a factor 0.8.

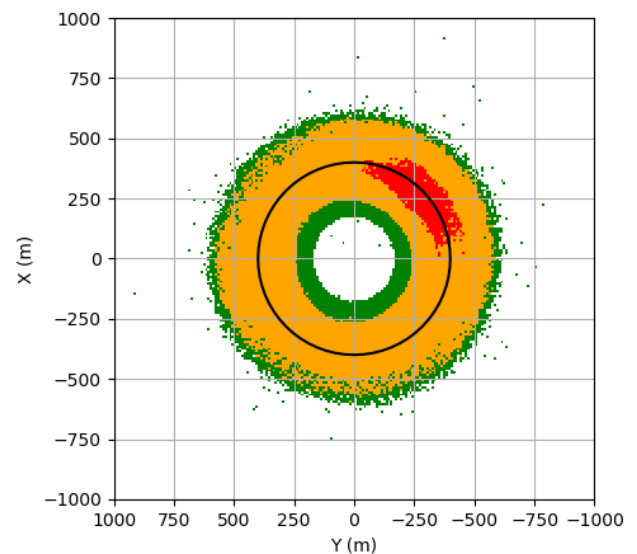


Figure 9.21: Discrete individual risk per year for the area around Rutten with the lift coefficient multiplied by a factor 0.8, green is $R_I < 10^{-6}$, orange is $10^{-6} < R_I < 10^{-5}$, and red is $R_I > 10^{-5}$.

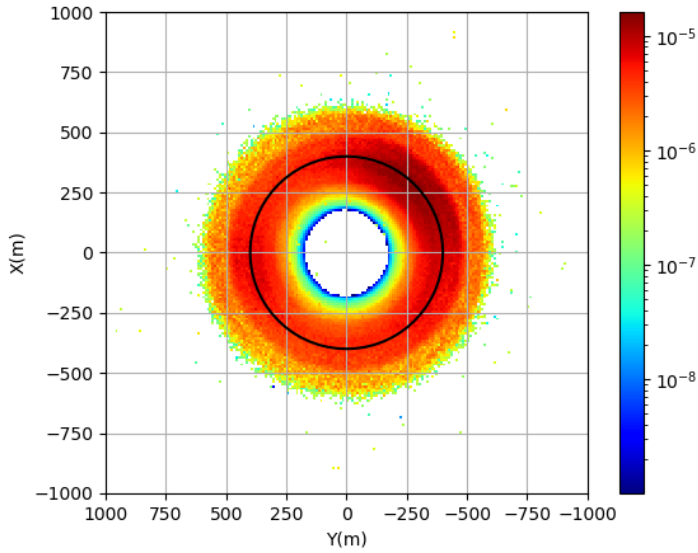


Figure 9.22: Individual risk per year for the area around Rutten with the lift coefficient multiplied by a factor 0.9.

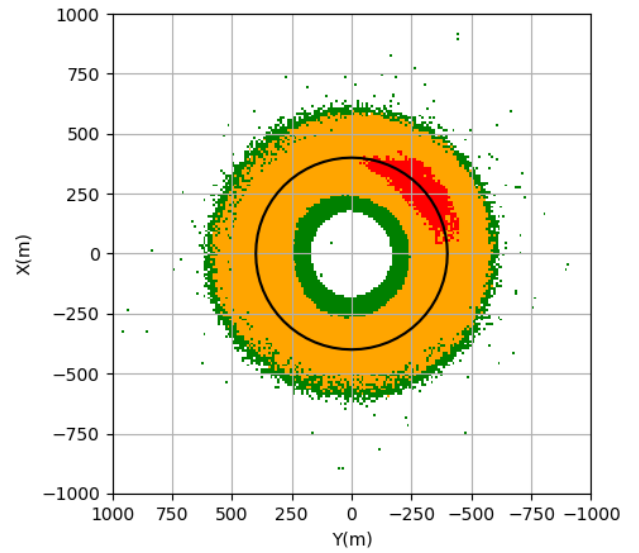


Figure 9.23: Discrete individual risk per year for the area around Rutten with the lift coefficient multiplied by a factor 0.9, green is $R_I < 10^{-6}$, orange is $10^{-6} < R_I < 10^{-5}$, and red is $R_I > 10^{-5}$.

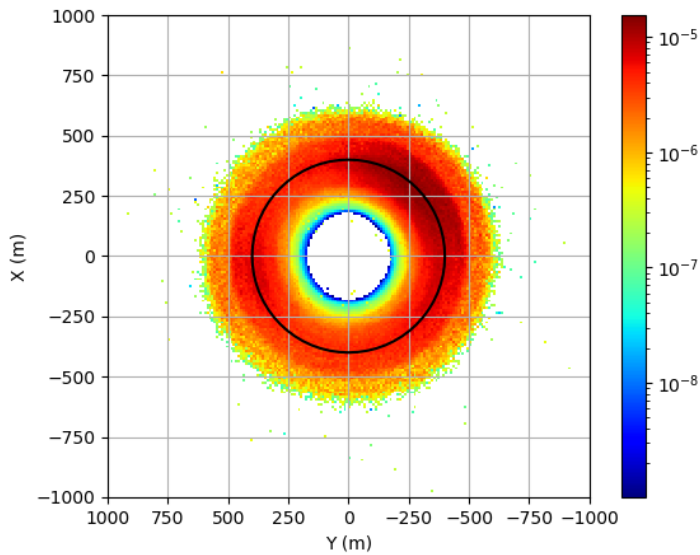


Figure 9.24: Individual risk per year for the area around Rutten with the lift coefficient multiplied by a factor 1.0.

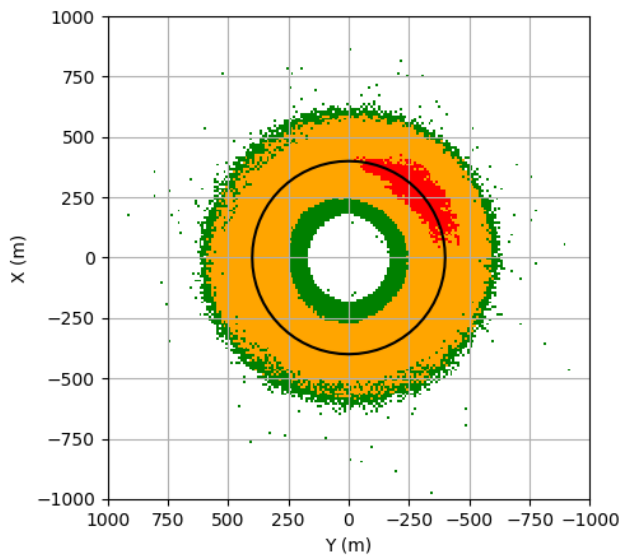


Figure 9.25: Discrete individual risk per year for the area around Rutten with the lift coefficient multiplied by a factor 1.0, green is $R_I < 10^{-6}$, orange is $10^{-6} < R_I < 10^{-5}$, and red is $R_I > 10^{-5}$.

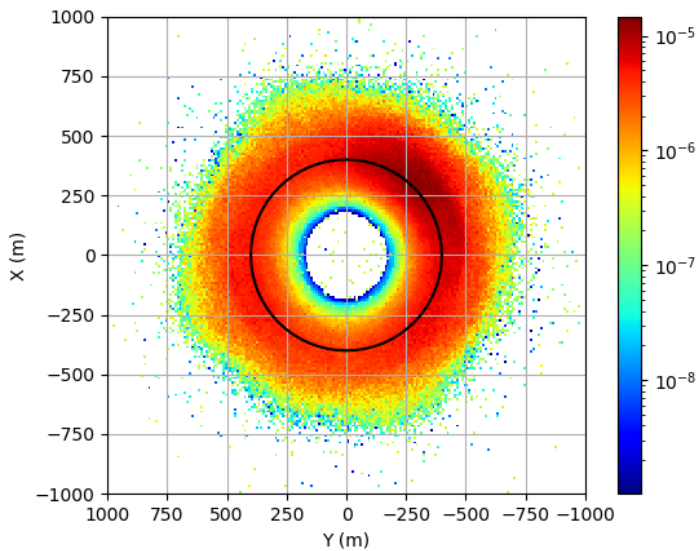


Figure 9.26: Individual risk per year for the area around Rutten with the lift coefficient multiplied by a factor 1.1.

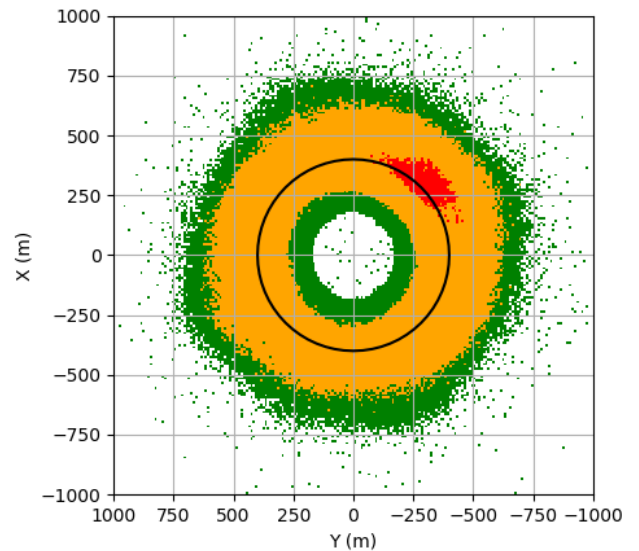


Figure 9.27: Discrete individual risk per year for the area around Rutten with the lift coefficient multiplied by a factor 1.1, green is $R_I < 10^{-6}$, orange is $10^{-6} < R_I < 10^{-5}$, and red is $R_I > 10^{-5}$.

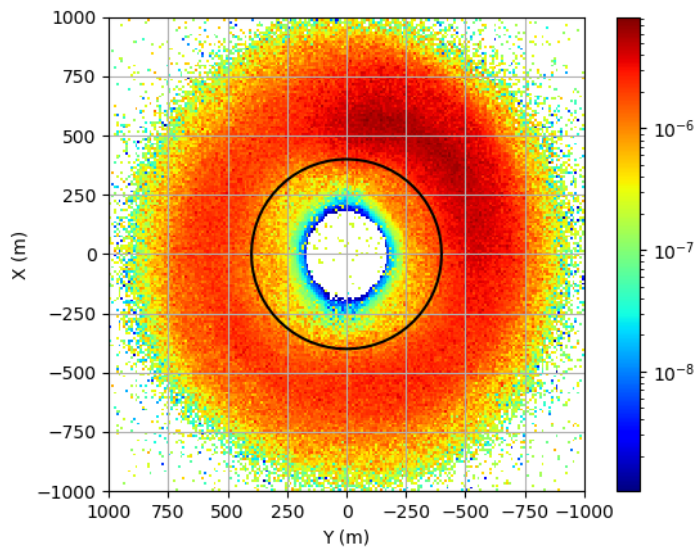


Figure 9.28: Individual risk per year for the area around Rutten with the lift coefficient multiplied by a factor 1.2.

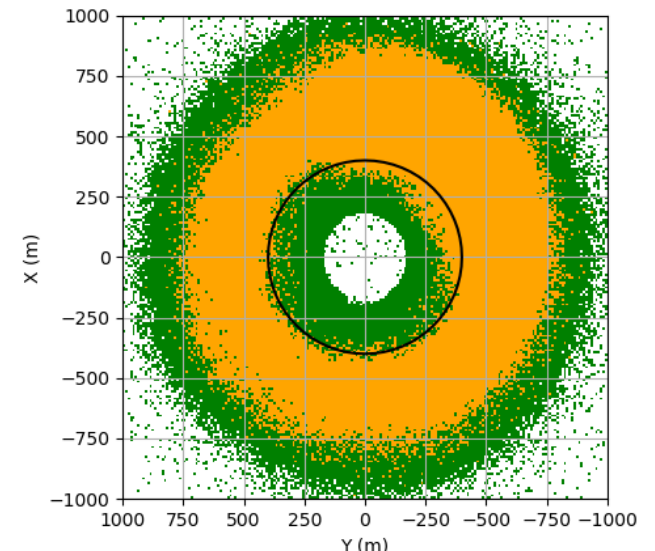


Figure 9.29: Discrete individual risk per year for the area around Rutten with the lift coefficient multiplied by a factor 1.2, green is $R_I < 10^{-6}$, orange is $10^{-6} < R_I < 10^{-5}$, and red is $R_I > 10^{-5}$.

Only the influence on the collective ground risk per year is depicted because the same sensitivity is expected on the collective ground risk per flight hour. In Figure 9.30 the relation between the collective ground risk per year and the lift coefficient multiplication factor is depicted. It is observed that the same behaviour of the collective ground risk is found as in the individual risk figures. The collective ground risk slightly increases between a lift coefficient multiplication factor between 0.8 and 1.1. However, the collective ground risk increases drastically with a lift coefficient multiplication factor of 1.2. In the individual risk plots it is observed that the kite is able to fly further due to the higher lift forces. This results in crash locations that are further away. Therefore, the kite also crashes in regions with a higher population density, the town of Rutten. Furthermore, nearly all crashes are outside the operational zone with a multiplication factor of 1.2. This also results in a higher collective ground risk. This combination results in the drastically higher collective ground risk if the lift coefficient is multiplied by a factor 1.2.

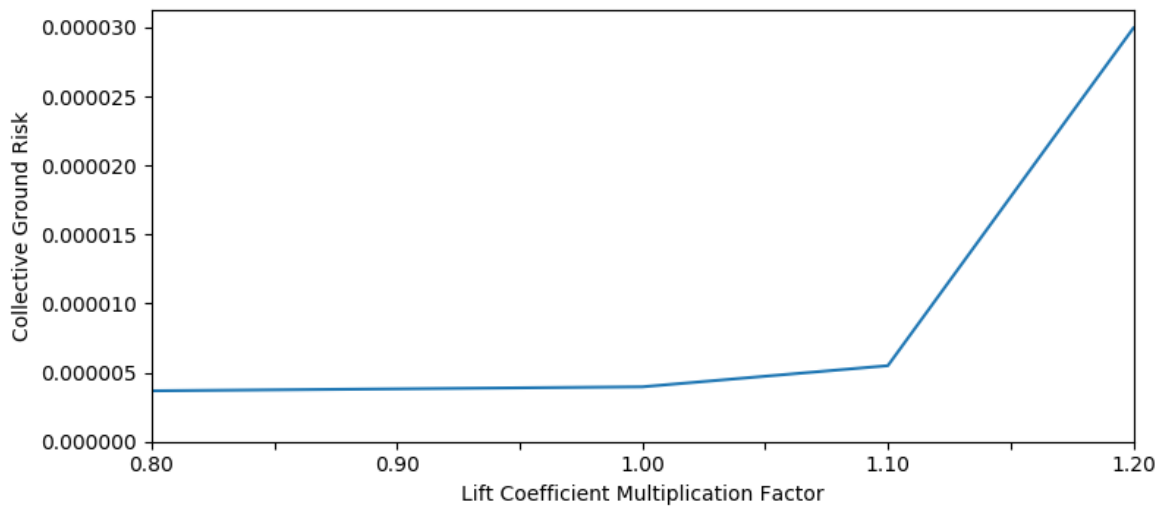


Figure 9.30: Relation between the lift coefficient multiplication factor and the collective ground risk.

Drag Coefficient

The sensitivity analysis of the drag coefficient consists of multiplying all the drag coefficients from Table 9.3 with a factor. This is also performed for the factors 0.8, 0.9, 1.0, 1.1, and 1.2. This relatively small factor is chosen because the drag coefficient is from its origin a sensitive parameter. Furthermore, otherwise physical impossible situations are simulated, the drag force unrealistically low compared to the lift force.

In Figure 9.31 until Figure 9.40 the influence of the drag coefficient on the individual risk is depicted. It is observed that the individual risk does only slightly change by an increasing drag coefficient. The red zone slightly decreases and the area where individual risk is present has moved slightly closer to the ground station, as depicted in Figure 9.39 and Figure 9.40. The clarification for this observation is that in this situation the kite flies less far due to a larger drag influence. Therefore, the individual risk moves closer to the ground station. The red zone decreases and the orange zone decreases at the outer boundary. The red zone decreases due to the lower impact velocity caused by the larger drag coefficient.

The individual risk is spread slightly more if the drag coefficient is multiplied by a factor 0.9. The red zone moves further away from the ground station. The orange and green zone increase in size. However, it is observed that if the drag coefficient is multiplied by a factor 0.8 the individual risk drastically change. The red zone has disappeared. The orange and green zone increase drastically. A larger area is posed by individual risk with a lower drag coefficient. The largest increase is clearly between the factor 0.8 and 0.9. The clarification of this observation is that in this situation the kite flies further due to a lower drag influence which results in a larger lift over drag ratio. This results in a lower maximum individual risk due to the lower concentration of crashes. However, there is at more locations individual risk present due to the longer distance flown.

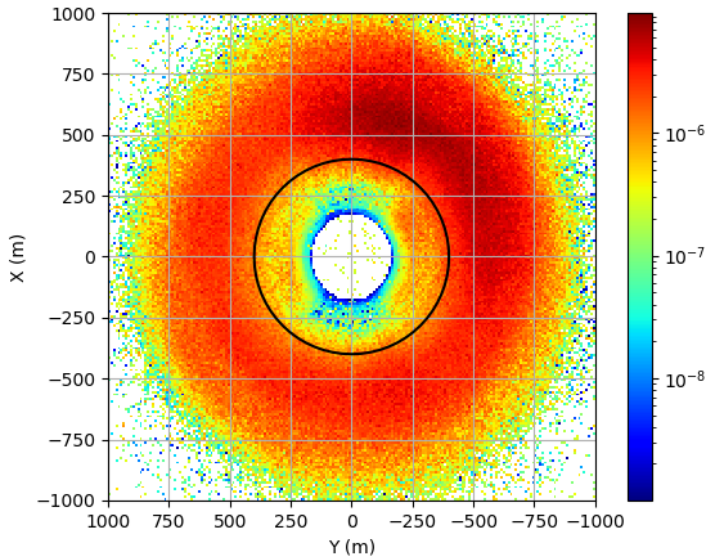


Figure 9.31: Individual risk per year for the area around Rutten with the drag coefficient multiplied by a factor 0.8.

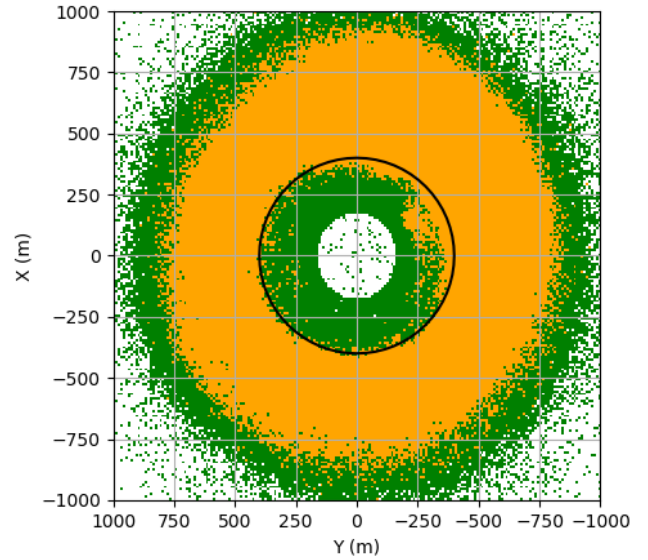


Figure 9.32: Discrete individual risk per year for the area around Rutten with the drag coefficient multiplied by a factor 0.8, green is $R_I < 10^{-6}$, orange is $10^{-6} < R_I < 10^{-5}$, and red is $R_I > 10^{-5}$.

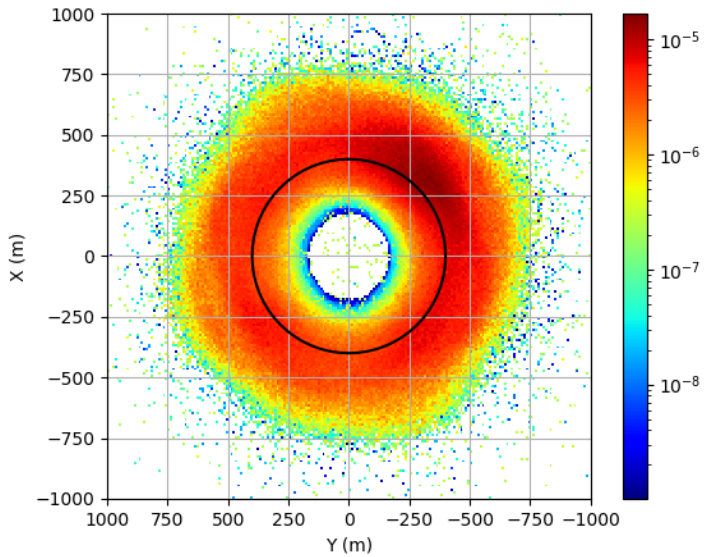


Figure 9.33: Individual Risk per year for the area around Rutten with the lift coefficient multiplied by a factor 0.9.

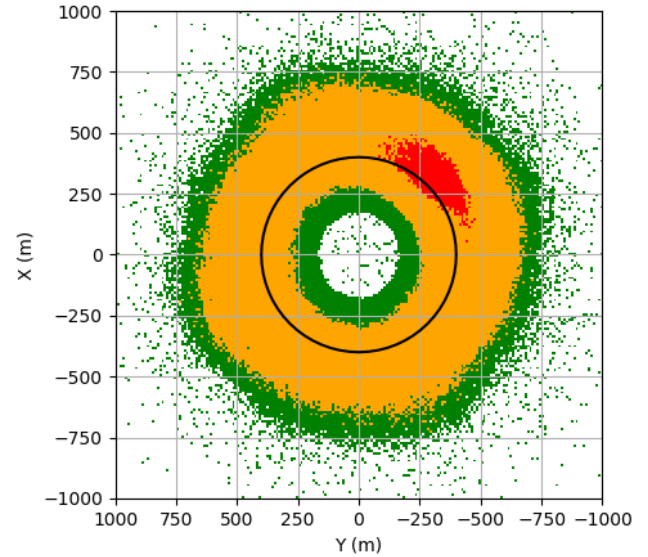


Figure 9.34: Discrete individual risk per year for the area around Rutten with the lift coefficient multiplied by a factor 0.9, green is $R_I < 10^{-6}$, orange is $10^{-6} < R_I < 10^{-5}$, and red is $R_I > 10^{-5}$.

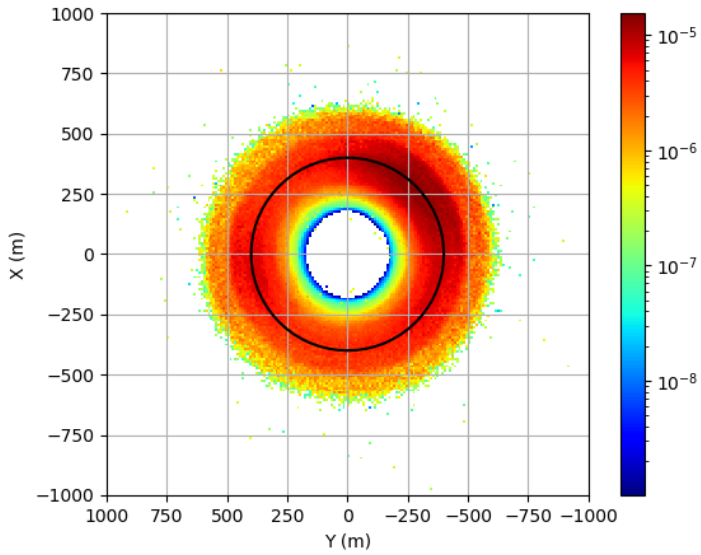


Figure 9.35: Individual risk per year for the area around Rutten with the drag coefficient multiplied by a factor 1.0.

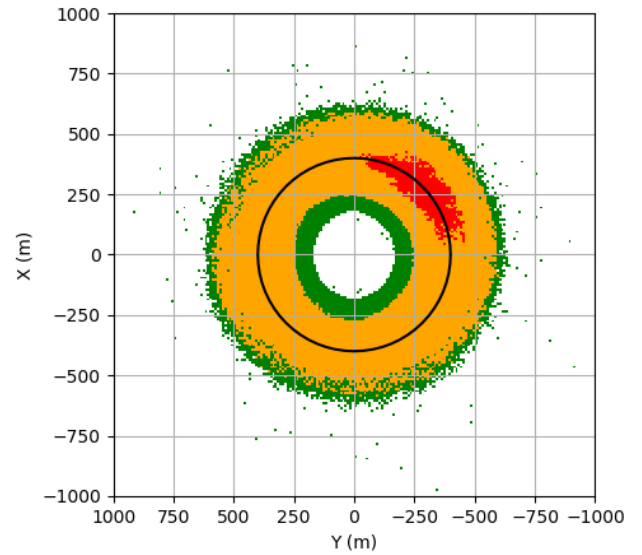


Figure 9.36: Discrete individual risk per year for the area around Rutten with the drag coefficient multiplied by a factor 1.0, green is $R_I < 10^{-6}$, orange is $10^{-6} < R_I < 10^{-5}$, and red is $R_I > 10^{-5}$.

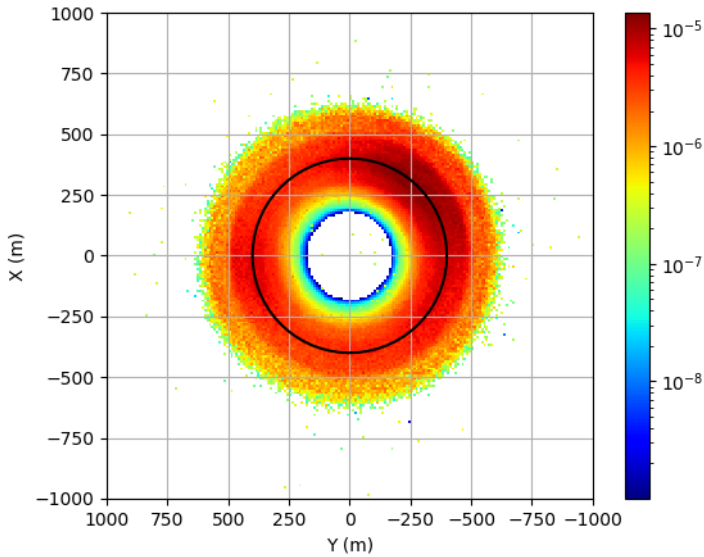


Figure 9.37: Individual risk per year for the area around Rutten with the drag coefficient multiplied by a factor 1.1.

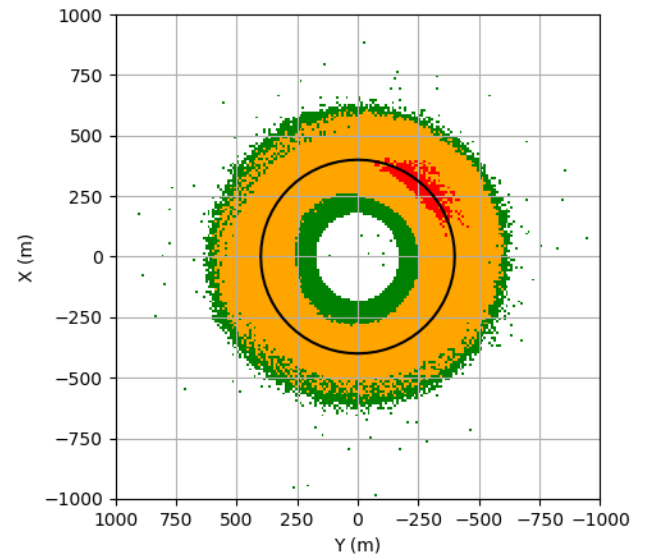


Figure 9.38: Discrete individual risk per year for the area around Rutten with the drag coefficient multiplied by a factor 1.1, green is $R_I < 10^{-6}$, orange is $10^{-6} < R_I < 10^{-5}$, and red is $R_I > 10^{-5}$.

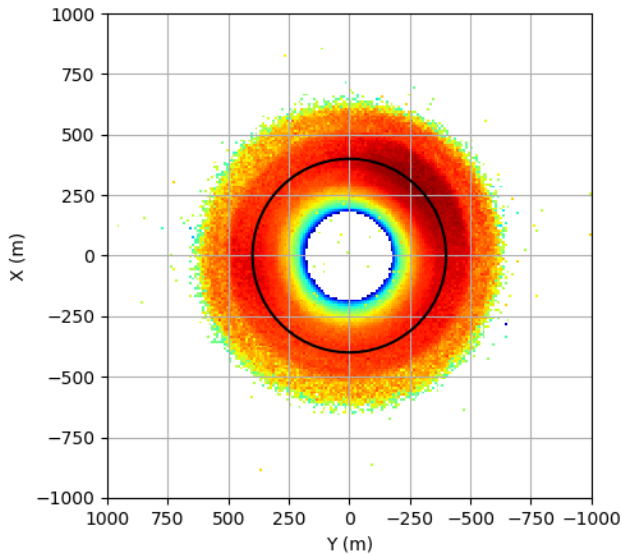


Figure 9.39: Individual risk per year for the area around Rutten with the drag coefficient multiplied by a factor 1.2.

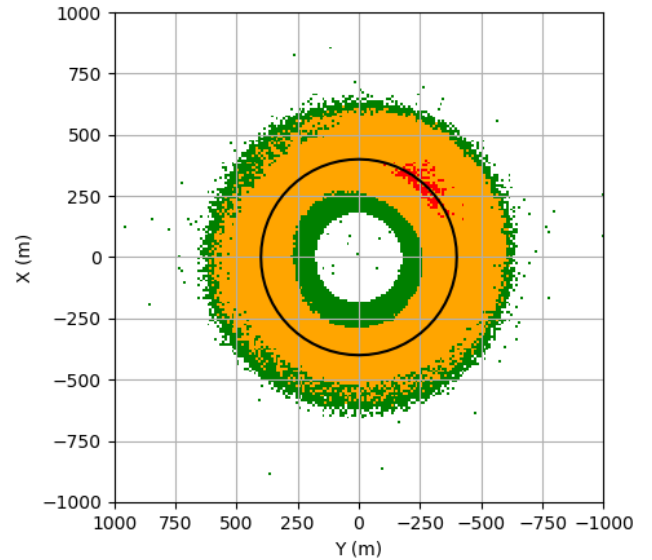


Figure 9.40: Discrete individual risk per year for the area around Rutten with the drag coefficient multiplied by a factor 1.2, green is $R_I < 10^{-6}$, orange is $10^{-6} < R_I < 10^{-5}$, and red is $R_I > 10^{-5}$.

Only the influence on the collective ground risk per year is depicted because the same sensitivity is expected on the collective ground risk per flight hour. In Figure 9.41 the relation between the collective ground risk per year and the drag coefficient multiplication factor is depicted. It is observed that the same behaviour of the collective ground risk is found as in the sensitivity analysis of the lift coefficient. The collective ground risk slightly decreases between a drag coefficient multiplication factor of 0.9 and 1.2. However, the collective ground risk increases drastically with a lift coefficient multiplication factor lower than 0.9. In the individual risk plots it is observed that the kite is able to fly further due to the lower drag forces. This results in crash locations that are further away. Therefore, the kite also crashes in regions with a higher population density, the town of Rutten. Furthermore, nearly all crashes are outside the operational zone with a multiplication factor of 0.8. This also results in a higher collective ground risk. This combination results in the drastically higher collective ground risk if the drag coefficient is multiplied by a factor 0.8.

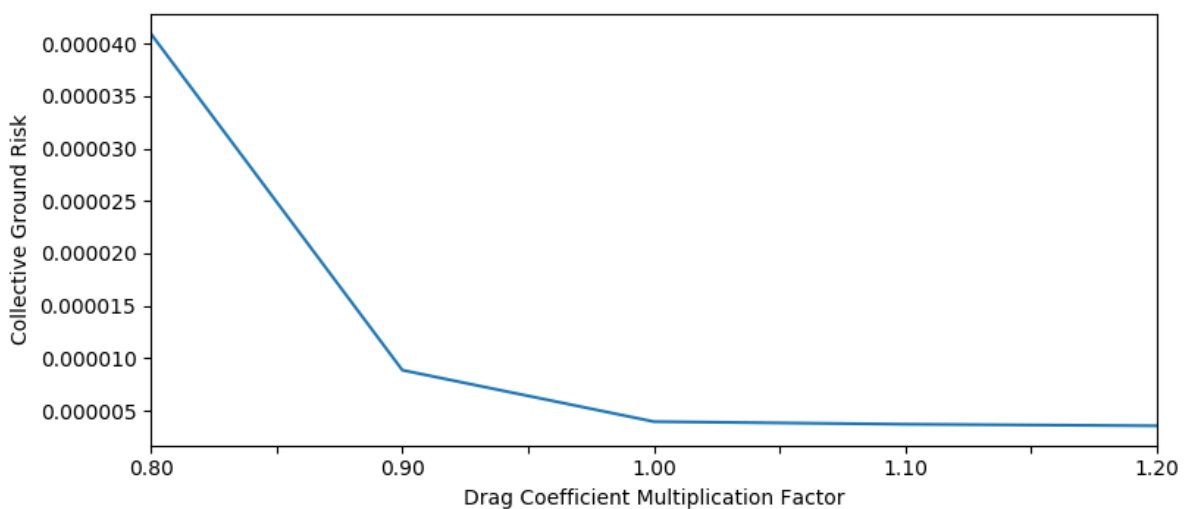


Figure 9.41: Relation between the drag coefficient multiplication factor and the collective ground risk.

9.6 Uncertainty Evaluation

In this section the uncertainty evaluation of the parameters identified in section 9.1 is performed. In section 9.1 four parameters were identified to be uncertain but linear. Namely, the total flight hours T_{total} , tether failure rate $\lambda_{i,tether}$, crash impact area $|A(i,e)|$, and the probability of shelter protection $\widehat{P}(S|i,H)$. The uncertainty of these parameters are evaluated in this section.

Firstly, the total flight hours uncertainty is evaluated. In section 9.1 it was assumed that the system operates 90% of the time if wind conditions allow to operate. This value can be maximally increased by 10% to keep it realistic, also because more than 100% is physically not possible. An increase of 10% in total flight hours results in a collective ground risk of 4.37×10^{-6} per year, as depicted in Table 9.4. This value is still way lower than the regulation limit of 1.6449×10^{-3} per year. Therefore, the total flight hours uncertainty does not have an impact on exceeding the collective ground risk limits.

Secondly, the tether failure rate uncertainty is evaluated. In section 9.1 it was assumed that the tether only fails ones per year. This was based on the worst case assumption of the Kitepower expert. The tether failure rate can be raised to two times a year, but higher factors would be unrealistic. The collective ground risk is 7.95×10^{-6} per year if the tether failure rate is raised by a factor 2, as depicted in Table 9.4. This value is still lower than the regulation limit of 1.6449×10^{-3} per year. Therefore, the tether failure rate uncertainty does not have an impact on exceeding the collective ground risk limit if even the worst case assumption is double exceeded. However, it is still important to investigate the exact parameter based on operational data.

Thirdly, the crash impact area uncertainty is evaluated. The crash impact area is divided in the area of the KCU and kite. However, the ratio between these two areas depend on the impact velocity as described in section 7.5. Therefore, the total crash impact area is analyzed with the maximum factor of the kite its crash impact area because the kite impact area potentially increases the most. In section 9.1 it is assumed that the crash impact area of the kite is only 10% of the crash impact area modelled by the model of Ale and Piers (2000). This assumption is made because the kinetic energy is divided over a large area. This assumption is uncertain. The crash impact area increases with a factor 10 if this assumption is not valid. This results in a collective ground risk of 3.97×10^{-5} per year, as depicted in Table 9.4. This value is still lower than the regulation limit of 1.6449×10^{-3} per year. Therefore, the crash impact area uncertainty does not have an impact on exceeding the collective ground risk limits.

Next, the probability of shelter protection uncertainty is evaluated. The probability of shelter protection is based on the statistics of Melnyck et al. (2014), in section 9.1. This value is identified at 90%. However, this value can be reduced with a factor 0.9 if the time spent in a vehicle is all outdoors and the time spent at work is also all outdoors. A reason for this could be the rural nature of the area. This results in a factor 1.9 higher collective ground risk due to Equation 7.13. The collective ground risk is 7.55×10^{-6} per year with the lower probability of shelter protection, as depicted in Table 9.4. This value is still lower than the regulation limit of 1.6449×10^{-3} per year. Therefore, the probability of shelter protection uncertainty does not have an impact on exceeding the collective ground risk limits.

Lastly, the collective ground risk is 1.66×10^{-4} per year if all the previously mentioned parameters are at its maximum factor, as depicted in Table 9.4. This is still a factor 10 lower than the regulation limit which is 1.6449×10^{-3} per year. All in all, the only uncertainty is the tether failure rate because this value is based on assumptions from the Kitepower expert.

Table 9.4: Uncertainty parameters with its maximum collective ground risk.

Parameter	Description	Maximum Factor	Collective Ground Risk with Maximum Factor	Collective Ground Risk Including All Maximum Factors
T_{Total}	Total Flight Hours	1.1	4.37×10^{-6}	1.66×10^{-4}
$\lambda_{i,tether}$	Tether Failure Rate	2	7.95×10^{-6}	
$ A(i,e) $	Crash Impact Area	10	3.97×10^{-5}	
$\hat{P}(S i,H)$	Probability of Shelter Protection	0.9	7.55×10^{-6}	

9.7 Discussion of Results

In this section the results of the simulation, sensitivity analysis, and uncertainty evaluation are discussed. In the simulation results it is identified that the system complies with the regulations on collective ground risk. However, the system does not completely comply with the individual risk limits. There is an area outside the operational zone with too high individual risk. Therefore, the operational zone should be enlarged to a radius of 500m in the dominant wind direction. Furthermore, in the simulation results it is identified that the wind conditions have a large influence on the individual risk and collective ground risk. In the simulation results it is also identified that the population density has a large influence on the collective ground risk per flight hour and collective ground risk per year. Therefore, the model should be adapted for every new test location.

In the sensitivity analysis on the lift and drag coefficient it is found that an increase in lift coefficient of factor 1.2 has a large impact on the collective ground risk. The same holds for a decrease in drag coefficient of the factor 0.8. In these situations the kite is able to fly further. Therefore, a more certain identification of the lift and drag coefficient is needed.

In the uncertainty evaluation it is found that all uncertain parameters cannot increase the collective ground risk over the regulation limit. However, the tether failure should be investigated in more detail because at the moment this value is based on assumptions from the Kitepower expert and not based on operational data.

Lastly, new designs of the system have a large influence on the model. Therefore, the model should also be adapted if the design changes. In the past years the kite size is changed. The kite size has a large influence on the individual and collective ground risk. The same holds for the maximum radial distance and the mass of the system. The maximum radial distance is changed in past designs. Therefore, the influence of the maximum radial distance on the third-party risk should be analysed if the maximum radial distance changes again. Also the mass of the system has changed over time. Therefore, the influence of the mass of the system on the third-party risk should also be analysed if the mass changes again.

10 Conclusion and Follow-up

Research

In this chapter the thesis is concluded and directions for further research are given. Firstly, in section 10.1 this thesis is concluded. Secondly, in section 10.2 follow-up research is proposed.

10.1 Conclusion

In chapter 1 the following research question has been identified:

Which third-party risks are posed by Kitepower operations and how high are these?

To address this research question, firstly, in chapter 2 the operation of the system is described in a structured way. The human intervention and division of roles during the operation is clarified. In chapter 3 it is found that there are three main third-party risk indicators in a quantitative third-party safety risk assessment, namely individual risk, collective ground risk per flight hour, and collective ground risk per year. Next, in chapter 4 it is found that 63% of the researched countries regulate on individual risk and 83% regulate on the FN-curve. The regulations on the FN-curve can be used as regulations for the collective ground risk per year. Subsequently, in chapter 5 the operations of the system are modelled as an agent-based system as a first step in the safety risk assessment. The responsibility and interaction of every agent is clarified in this chapter.

In chapter 6 a pure hazard brainstorm is performed. Four potential safety-relevant scenarios are constructed from the hazards that are identified during the hazard brainstorm session and from earlier performed reliability studies. These four scenarios give a new view on the safety of the system. In the already performed reliability studies no potential safety-relevant scenarios were constructed. In chapter 7 the scenario in which the tether, KCU, and kite fly away after a tether failure (scenario I) is modelled. Scenario I is the most likely scenario of chapter 6. In chapter 8 this model is implemented in Python. Furthermore, in chapter 8 the model is verified and validated. It is concluded that the model behaves as expected.

In chapter 9 the results are depicted and the sensitivity analysis is performed. The collective ground risk per year is identified at $3.972732177 \times 10^{-6}$ per year with the regulation limit at 1.6449×10^{-3} per year. The maximum collective ground risk per flight hour is identified at 2.8×10^{-8} fatalities per flight hour with the regulation limit at 10^{-6} fatalities per UA flight hour. Furthermore, it is found that in the dominant wind direction the individual risk is above the limit of 10^{-5} fatalities per year. This problem is solved by enlarging the operational zone to a radius of 500m in the dominant wind direction. Therefore, the main conclusion of chapter 9 is that the system complies with all the regulations on third-party risk if the operational zone is enlarged to 500m in the dominant wind direction.

Furthermore, in chapter 9 it is identified that the wind conditions and population density have a large impact on the individual and collective ground risk. Therefore, for every new location the model should be adapted to the local weather conditions and population density to be able to identify the individual and collective ground risk for the specific location.

In the sensitivity analysis of chapter 9 it is found that the individual and collective ground risk are sensitive to the lift and drag coefficient. However, no regulation limits were exceeded during the sensitivity analysis. In conclusion, the safety findings are still valid but in further research the lift and drag coefficients should be modelled more precisely.

Lastly, in the uncertainty analysis of chapter 9 it is found that all the uncertain parameters do not have a critical impact on the collective ground risk. However, the tether failure rate should be researched in detail to obtain an operational data based tether failure rate.

10.2 Follow-up Research

In this section follow-up research is proposed. These follow-up research consist of three parts. Firstly, recommendations are given to extend the current third-party risk model. Secondly, recommendations are given to research some limitations and undiscovered influences of parameters on the third-party risk model. Lastly, recommendations are given on the adaptation of the model in the situation the operation of the system changes.

Extension Third-Party Risk Model

In this thesis only scenario I is modelled without considering the tether snag situation. Therefore, the third-party risk model can be extended by also modelling all the other identified safety-relevant scenarios in chapter 6. Therefore, the following research should be performed to extend the current third-party risk model:

- **Scenario I extension:** Scenario I, the kite, KCU, and tether fly away, is modelled in this thesis. However, in scenario I the tether can snag behind an object. This part of the scenario is not modelled yet. There should be looked into this part of the scenario.
- **Scenario II:** Scenario II, the kite and KCU fly away from the system, is not modelled because of its low probability. However, scenario II should still be analysed in more detail. This scenario is easily adaptable from the developed model in chapter 7. In order to simulate scenario II only the tether weight should be removed from the developed model.
- **Scenario III:** Scenario III, the kite flies away from the system, is not modelled because of its low probability. However, scenario III should still be analysed in more detail.
- **Scenario IV:** Scenario IV, the scenario in which the complete system slides over the ground, is not modelled also because of its low probability. However, scenario IV should still be analysed in more detail.

Third-party Risk Model Parameters

During the development of the model some limitations and undiscovered influences of parameters were identified. Not all limitations and influences on this model were researched during this thesis. Therefore, the following research should be performed as a follow-up:

- **Influence kite size:** In this thesis the 60m² kite is analysed. However, Kitepower is also developing larger kites, for example 100m² kites. The influence of this size increase should be analysed in detail.
- **Influence maximum radial distance:** In this thesis a maximum radial distance is assumed of 300m. However, in different designs different tether lengths are considered. Therefore, the influence of the maximum radial distance on the third-party risk should be analysed if the maximum tether length changes again.
- **Mass influence:** In this thesis a mass of 30kg for the KCU and 80kg for the kite is assumed. However, this will probably still change in the further development of the system. Therefore, the influence of the masses of the kite and KCU on the third-party risk should be analysed if the masses change.
- **Event rate identification:** The event rate of the tether failure is based on assumptions of the Kitepower expert. Therefore, this value is not that accurate yet. The exact event rate of the tether failure should be analysed if more operational hours are performed.
- **Operational hour identification:** The exact operational plan is not clear at this design stage. Therefore, the assumption that at 90% of the time the system is harvesting energy should be validated in a further design stage.
- **Model adaptation for new locations:** In this thesis it is found that the wind direction and population density have a large impact on the individual risk and the collective ground risk. Therefore, the model should be adapted to the local weather conditions and population density if the system operates at a new location.
- **Detailed population density map:** In this thesis a non-detailed population density map is used because a more detailed population density map is not available. However, in next third-party risk identification processes there should be looked into a more detailed population density map.
- **Lift coefficient:** In the sensitivity analysis it is found that the individual risk and collective ground risk are sensitive to the lift coefficient. Therefore, the lift coefficient should be identified more precisely.
- **Drag coefficient:** In the sensitivity analysis it is found that the individual risk and collective ground risk are sensitive to the drag coefficient. Therefore, the drag coefficient should be identified more precisely.

Change of Kitepower Operations

In the developed model the current system design is considered. The third-party risk model should be adapted if the system design changes significantly. These design changes can be numerous things. An example is the reduction of the operational zone. In the current design the operational zone has a radius of 400m. However, eventually Kitepower would like to reduce the radius of the operational zone. This operational zone reduction has a large influence on the considered hazards and considered safety-relevant scenarios.

References

- E. Ancel, F.M. Capristan, J.V. Foster, and R.C. Condotta. Real-time risk assessment framework for unmanned aircraft system (uas) traffic management (utm). Conference: 17th AIAA Aviation Technology, Integration, and Operations Conference, 2017. Doi: 10.2514/6.2017-3273.
- U. Ahrens, M. Diehl, and R. Schmehl. Airborne Wind Energy. Green Energy and Technology. Springer, Berlin, Heidelberg, 978-3-642-39964-0, 2013. Doi: 10.1007/978-3-642-39965-7.
- B.J.M. Ale and M. Piers. The assessment and management of third party risk around a major airport. *Journal of Hazardous Materials*, 71(1-3):16, 2000. Doi: 10.1016/S0304-3894(99)00069-2.
- S. Bertrand, N. Raballand, F. Viguier, and F. Muller. Ground risk assessment for long-range inspection missions of railways by uavs. Conference: 2017 International Conference on Unmanned Aircraft Systems, 2017. Doi: 10.1109/ICUAS.2017.7991331.
- H.A.P. Blom. Agent based safety risk analysis. Lecture Slides AE4448, January 2018-2019.
- H.A.P. Blom, S.H. Stroeve, and H.H. de Jong. Safety risk assessment by monte carlo simulation of complex safety critical operations. Conference: 14th Safety-critical Systems Symposium, 2006. Doi: 10.1007/1-84628-447-3_3.
- H.A.P. Blom, C. Jiang, W.B.A. Grimme, M. Mitici, and Y.S. Cheung. Third party risk modelling of Unmanned Aircraft System operations , with application to parcel delivery service. 2020.
- P.H. Bottelberghs. Risk analysis and safety policy developments in the Netherlands. *Journal of Hazardous Materials*, 71(1-3):59–84, 2000. Doi: 10.1016/S0304-3894(99)00072-2.
- C. Brezoescu. Small lightweight aircraft navigation in the presence of wind. Université de Technologie de Compiègne. 2013.
- D.A. Carter, J.J. Mewis, H.J. Pasma, and E.E. De Rademaeker. The scaled risk integral - a simple numerical representation of case societal risk for land use planning in the vicinity of major accident hazards. *Loss prevention and safety promotion in the process industries*, 2:219–224, 2002. Accessed by: <https://www.tib.eu/en/search/id/BLCP%3ACN010103903/The-scaled-risk-integral-a-simple-numerical-representation/>. Retrieved on: 23-04-2021.
- C. de Castro, M. Mediavilla, L.J. Miguel, and F. Frechoso. Global wind power potential: Physical and technological limits. *Energy Policy*, 39(10):6677–6682, 2011. Doi: 10.1016/j.enpol.2011.06.027
- CBS. Wijk- en buurtkaart. Centraal Bureau voor de Statistiek. 2020. Accessed by: <https://www.cbs.nl/nl-nl/longread/aanvullende-statistische-diensten/2020/toelichting-wijk-en-buurtkaart-2018-2019-en-2020>. Retrieved on: 03-08-2021
- J. Clegg. Battlefield airborne communications node (bacn). Northrop Grumman, 2021. Accessed by: <https://www.northropgrumman.com/what-we-do/air/battlefield-airborne-communications-node-bacn/>. Retrieved on: 29-04-2021.
- A. La Cour-Harbo. Quantifying risk of ground impact fatalities for small unmanned aircraft. *Journal of Intelligent & Robotic Systems*, 93(4):367–384, 2019. Doi: 10.1007/s10846-018-0853-1.
- G. de Croon, M.A. Groen, C. De Wagter, B. Remes, R. Ruijsink, and B.W. van Oudheusden. Design, aerodynamics and autonomy of the delfly. *Bioinspiration & Biomimetics*, 7(2), 2012. Doi: 10.1088/1748-3182/7/2/025003.

EASA. *Official Journal of the European Union. European Aviation Safety Agency (EASA)*, 2008.

EASA. *Concept of operations for drones a risk based approach to regulation of unmanned aircraft. European Aviation Safety Agency (EASA)*, 2015.

A.W. Evans, P.B. Foot, S.M. Mason, I.G. Parker, and K. Slater. *Third party risk near airports and public safety zone policy. Technical report, National Air Traffic Services Limited*, 1997.

FAA. *Notification for airborne wind energy systems (awes). Federal Register*, 76(235), 2011.

FAA. *National policy: Unmanned aircraft systems (uas) operational approval. Federal Aviation Administration (FAA)*, 2013.

P. Faggiani, *Pumping kites wind farm, TU Delft. 2014. MSc thesis.*

U. Fechner. *A Methodology for the Design of Kite-Power Control Systems. TU Delft. 2016. PhD thesis.*

D.I. Feinstein, W.F. Haugel, M.L. Kardatzke, A. Weinstock. *Personnel casualty study. Illinois Institute of Technology. 1968. Technical Report Project No. J 6067*

L. Gooijer, N. Cornil, and C.L. Lenoble. *An international comparison of four quantitative risk assessment approaches. National Institute of Public Health and the Environment (RIVM)*, 2011. Accessed by: <https://www.rivm.nl/bibliotheek/rapporten/620552001.pdf>. Retrieved on: 18-04-2021.

I.L. Hirst and D.A. Carter. *A “worst case” methodology for obtaining a rough but rapid indication of the societal risk from a major accident hazard installation. Journal of Hazardous Materials*, 92(3):223–237, 2002. Doi: 10.1016/S0304-3894(02)00016-X.

R. Hillestad, K.A. Solomon, B.G. Chow, J.P. Kahan, B. Hoffman, S.D. Brady, J.A. Stoop, J.S. Hodges, H. Kloosterhuis, and G. Stiles. *Airport growth and safety a study of the external risks of Schiphol airport and possible safety enhancement measures. RAND*, 1993. Accessed by: https://www.rand.org/pubs/monograph_reports/MR288.html. Retrieved on: 19-04-2021.

ICAO. *Aeronautical charts - annex 4 to the convention on international civil aviation*, 2009. Accessed by: https://www.icao.int/safety/airnavigation/nationalitymarks/annexes_booklet_en.pdf. Retrieved on: 29-04-2021.

ICAO. *Aerodromes - annex 14 to the convention on international civil aviation*, 2013. Accessed by: <https://www.warningspheres.com/pdf/icao-annex-14-2013.pdf>. Retrieved on: 29-04-2021.

C. Jiang, H.A.P. Blom, and A. Sharpanskykh. *Third party risk indicators and their use in safety regulations for uas operations. Conference: AIAA AVIATION 2020 FORUM*, 2020. Doi: 10.2514/6.2020-2901.

H. Johnson. *Kite Farm Simulation. TU Delft. 2019. MSc thesis.*

D. Jones. *Nomenclature for hazard and risk assessment in the process industries. Institute of Chemical Engineering*, 1985.

S.N. Jonkman, P.H.A.J.M. van Gelder, and J.K. Vrijling. *An overview of quantitative risk measures for loss of life and economic damage. Journal of Hazardous Materials*, 99(1): 30, 2003. Doi: 10.1016/S0304-3894(02)00283-2.

R.E. Jorissen and P.J.M. Stallen. *Quantified Societal Risk and Policy Making, volume 12 of Technology Risk and Society. Kluwer Academic Publishers, isbn: 978-0-7923-4955-6 edition*, 1998. Doi: 10.1007/978-1-4757-2801-9.

Kitepower. *Internal source. 2021*

- KNMI. *Dag gegevens van het weer in Nederland*. Royal Netherlands Meteorological Institute. 2021. Accessed by: <https://www.knmi.nl/nederland-nu/klimatologie/daggegevens>. Retrieved on: 24/08/2021.
- G.M.H. Laheij, J.G. Post, and B.J.M. Ale. *Standard methods for land-use planning to determine the effects on societal risk*. *Journal of Hazardous Materials*, 71(1-3):269–282, 2000. Doi: 10.1016/s0304-3894(99)00083-7.
- R. Melnyk, D. Schrage, V. Volovoi, and H. Jimenez. *A third-party casualty risk model for unmanned aircraft system operations*. *Reliability Engineering and System Safety*, 124:105–116, 2014. ISSN 09518320. Doi: 10.1016/j.ress.2013.11.016.
- J. Oehler and R. Schmehl. *Aerodynamic characterization of a soft kite by in situ flow measurement*. *Wind Energy Science*, 4, 1-21, 2019. Doi: 10.5194/wes-4-1-2019
- Overheid. *Regeling kabelvliegers en kleine ballons*. wetten.overheid.nl, 2014. Accessed by: <https://wetten.overheid.nl/BWBR0007094/2014-12-12>. Retrieved on: 5-05-2021.
- M. Piers. *Quantified Societal Risk and Policy Making*, chapter *Methods and Models for the Assessment of Third Party Risk due to Aircraft Accidents in the Vicinity of Airports and Their Implications for Societal Risk*, pages 166–204. Volume 17 of *Jorissen and Stallen (1998)*, 1998. Doi: 10.1007/978-1-4757-2801-9.
- R.M. Pitblado, M. Bardy, P. Nalpanis, P. Crossthwaite, K. Molazemi, M. Bekaert, and V. Raghunathan. *International comparison on the application of societal risk criteria*. *Process Safety Progress*, 31(4), 2012. Doi: 10.1002/prs.11525.
- S. Primatesta, A. Rizzo, and A. La Cour-Harbo. *Ground risk map for unmanned aircraft in urban environments*. *Journal of Intelligent & Robotic Systems*, 97:489–509, 2019. Doi: 10.1007/s10846-019-01015-z.
- Range Commanders Council. *Range safety criteria for unmanned air vehicles - rationale and methodology supplement*. Range commanders council white sands missile range nm. 2001.
- RIVM. *Reference manual bevi risk assessments*. RIVM(National Institute of Public Health and the Environment), 2009. Accessed by: <https://www.rivm.nl/documenten/reference-manual-bevi-risk-assessments-version-32>. Retrieved on: 23-04-2021.
- G.J.J. Ruijgrok. *Elements of airplane performance*. Delft University of Technology. Delft Academic Press, Delft, isbn: 978-90-6562-204-4, 2009.
- V. Salma, R. Ruitkamp, M. Kruijff, M.M.R van Paassen, and R. Schmehl. *Airborne wind energy - Advances in Technology Development and Research*, chapter *Current and Expected Airspace Regulations for Airborne Wind Energy Systems*. Volume 29 of *Schmehl (2018)*, 2018. Doi: 10.1007/978-981-10-1947-0_29.
- V. Salma, F. Friedl, and R. Schmehl. *Improving reliability and safety of airborne wind energy systems*. *Airborne Wind Energy Research Group*, 23(5), 2019. Doi: 10.1002/we.2433.
- R. Schmehl. *Airborne wind energy - Advances in Technology Development and Research*. *Green Energy and Technology*. Springer, Singapore, isbn: 978-981-10-1946-3 edition, 2018. Doi: 10.1007/978-981-10-1947-0.
- R. Schmehl. *Airborne wind energy – An introduction to an emerging technology*. AWESCO, 2019. Accessed by: <http://awesco.eu/awe-explained/>. Retrieved on: 4-11-2021.
- K.A. Solomon. *Airplane crash risk to ground population*. University of California, UCLA-ENG-7424, 1974.
- R.B. Stull. *Meteorology for Scientists and Engineers*. 2000.

V.M. Trbojevic. *Risk criteria in eu*. Risk Support Limited, London, U.K., 2005. Accessed by: https://cdn.regulation.gov.ua/3c/be/02/1f/regulation.gov.ua_File_224.pdf. Retrieved on: 27-05-2021.

C. Vermillion, M. Cobb, L. Fagiano, R. Leuthold, M. Diehl, R.S. Smith, T.A. Wood, S. Rapp, R. Schmehl, D. Olinger, and M. Demetriou. *Electricity in the air: Insights from two decades of advanced control research and experimental flight testing of airborne wind energy systems*. *Annual Reviews in Control*, 2021. Doi: 10.1016/j.arcontrol.2021.03.002.

J.E. Vettorato. *Modelling and Simulation of Third Party risk of an Unmanned Aircraft Systems-based Surveillance Operation in the Port of Rotterdam*. TU Delft. 2021. MSc thesis.

R. van der Vlucht, J. Peschel, R. Schmehl. *Design and Experimental Characterization of a Pumping Kite Power System*. In: U. Ahrens, M. Diehl, R. Schmehl. *Airborne Wind Energy. Green Energy and Technology*. Springer, Berlin, Heidelberg, 978-3-642-39964-0, 2013. Doi: 10.1007/978-3-642-39965-7.

R. Wiser and M. Bolinger. *Wind Technologies Market Report*. U.S. Department of Energy, 2018. Accessed by: <https://www.energy.gov/sites/default/files/2019/08/f65/2018%20Wind%20Technologies%20Market%20Report%20FINAL.pdf>. Retrieved on: 22-4-2021.

P.A. Zielinski and P. Eng. *Setting individual and societal risk criteria for safety of dams*. Conference: 2014 Annual Canadian Dam Association Conference, 2014. Accessed by: https://www.researchgate.net/publication/335453062_SETTING_INDIVIDUAL_AND_SOCIAL_RISK_CRITERIA_FOR_SAFETY_OF_DAMS. Retrieved on 23-04-2021.